Multicomponent diffusion systems

by

Sun Ung Kim

A dissertation submitted in partial fulfillment
of the requirements for the degree of
Doctor of Philosophy
(Mechanical Engineering)
in the University of Michigan
2013

Doctoral Committee:

Assistant Professor Charles W. Monroe, Co-Chair
Professor Anna G. Stefanopoulou, Co-Chair
Assistant Professor Donald J. Siegel
Professor Robert M. Ziff

Acknowledgement

I would like to acknowledge the support of Monroe research group, Stefanopoulou research group at the University of Michigan, and the research group of Dr. Jake Christensen at the Robert-Bosch Research and Technology Center. I would like to thank the University of Michigan-Fraunhofer Alternative Energy Technologies for Transportation program, the Automotive Research Center (ARC), and the Advanced Research Projects Agency-Energy (ARPA-E) for funding my research. The Robert-Bosch Research and Technology Center gave me an internship opportunity, directly related to my researches at the University of Michigan. The University of Michigan Rackham Graduate School supported my conference travels.

Table of Contents

List of Figures

List of Tables

List of Symbols

A	area, m^2
A	amplitude
a_i	activity coefficient of species i
a_V	surface-to-volume ratio, 1/m
Bi	Biot number Bi
c_i	molar concentration of species i, mol/m^3
c_p	specific heat capacity, J/kg-K
C_p	volumetric heat capacity, J/m^3-K
c_T	total concentration, mol/m^3
c_0	solvent concentration, mol/m^3
c_i^∞	concentration of species i in the reservoir, mol/m^3
D	Fickian diffusivity, m^2/s
D	tube diameter, m
$\mathscr{D}_{ij}$	Stefan-Maxwell coefficient for interaction of species i and j, m^2/s
F	Faraday's constant 96,487 C/equiv
f_i	molar activity coefficient on a molar concentration basis
h	convective heat transfer coefficient, W/m^2-K
$\overline{H}_i$	partial molar enthalpy of species i, J/mol
$\vec{i}$	electric current density, A/m^2
$\vec{i}_i$	electric current density in phase i, A/m^2
I	electric current, A
I	dimensionless current density
i_0	exchange-current density, A/m^2
I_L	dimensionless limiting current
i_n	charge exchange, A/m^2
$\boldsymbol{J}$	Jacobian matrix
$\vec{J}_i$	molar flux density of species i relative to the mass-average velocity, mol/cm^2-s
k	thermal conductivity, W/m-K
K_{ij}	drag coefficient for interaction of species i and j, $J-s/m^5$
L	length, m
M_i	chemical formula of species i
n	number of electrons involved in electrochemical reaction
N	number of species
$\overrightarrow{N_i}$	total molar flux of species i, mol/m^2-s
$\vec{N}_j^{\text{rxn}}$	molar flux that arises from heterogeneous reactions, mol/m^2-s
$\vec{N}_j^{\text{forced}}$	molar flux that arises from forced convection, mol/m^2-s

p	pressure, N/m^2
p	period, s
P	power, W
P_c	power associated with concentration overpotential, W
Pe	modified Péclet number
Q	volumetric flowrate, m^3/s
$\vec{q}^{(x)}$	Dufour energy flux density, W/m^2
R	universal gas constant, 8.3143 J/mol-K
R	load or resistance, Ω
R_i	homogeneous generation rate of species i
s	dimensionless ratio between the electric solid- and liquid-phase resistivities
s_i	stoichiometric coefficient in the reaction of species i
$\Delta\overline{S}_{rxn}$	reaction entropy, J/mol-K
t	time, s
T	absolute temperature, K
U	open-circuit potential, V
V	potential, V
$\vec{v}^{\,forced}$	convective velocity, m/s
$\vec{v}^{\blacksquare}$	volume-average velocity, m/s
$\overline{V}_i$	partial molar volume of species i, m^3/mol
t_i^0	cation transference number of species i
$\vec{v}_i$	velocity of species i, m/s
X	dimensionless reaction distribution
y_i	mole fraction of species i
z_i	equivalent charge carried by species i, C
α^2	a ratio of electric bulk resistance to kinetic resistance
β	symmetry factor
δ	thickness, m
ϵ	porosity
Φ	electrostatic potential, V
Φ_c	concentration overpotential, V
ϕ_c	dimensionless concentration overpotential
η_s	surface overpotential, V
κ	conductivity, S/m
μ	dynamic viscosity
μ_i	chemical or electrochemical potential of species i, J/mol
ν_j	stoichiometric coefficient of species i
θ	dimensionless ion concentration
θ	dimensionless temperature
ρ	density, kg/m^3
ρ	resistivity, Ω-m
ρ_i	bulk resistivity of phase i, Ω-m
ρ_k	kinetic resistivity, Ω-m

σ	dimensionless reaction heat
τ	dimensionless time
ξ	dimensionless position in the separator region

Superscript

expl	experimental
rxn	reaction
forced	forced convection
θ	standard state
0	value at the liquid surface
0	value or result of initial guess
1	value or result of first iteration

Subscript

a	acetone
avg	average
b	methanol
c	air
c	concentration-related
e^-	electron
eff	effective
ext	exterior
f	friction-related
fluc	fluctuation
int	interior
max	maximum
min	minimum
ref	reference
s	surface
SEI	SEI layer
surf	value at the separator boundary
0	solvent
0	value or result of initial guess
1	value or result of first iteration
1	solid
2	liquid, electrolyte
+	cation
–	anion

Abstract

This dissertation focuses on coupled multicomponent mass, heat, and charge transfer analyses of chemical and electrochemical systems. First, the Stefan-Maxwell multicomponent diffusion theory is introduced, along with constitutive laws for chemical and electrochemical potential. This set of model equations is then applied to various systems: gas diffusion in a tube, simultaneous mass and charge transfer in a convection battery, coupled heat and charge transfer in a prismatic lithium-ion battery, and coupled heat, mass, and charge transfer in a very-high-capacity lithium-ion cell.

Carty and Schrodt's measurements of steady-state species concentrations during ternary gas diffusion in a tube are analyzed in Chapter 2. The driving forces for gas diffusion are concentration gradients in the tube, which induce chemical potential gradients that drive relative species fluxes. I find that relaxing Carty and Schrodt's assumptions when analyzing their data results in better fits of theory to measurements.

In chapter 3, the research focus shifts to electrochemical systems. In addition to concentration, which drives diffusion, electric potential is introduced within the Stefan-Maxwell theory as a driving force for migration. Electric effects are included through thermodynamic constitutive laws based on electrochemical potentials. The resulting concentrated-solution theory allows the description of simultaneous mass and charge transport in isothermal, isobaric binary electrolytes. I apply the concentrated-solution theory to illustrate the effect of electrolyte flow through the separator in a traditional

battery, showing how convection alters limiting currents and can improve overall power efficiency during high-current operation.

Two different approaches to thermoelectrochemical transport in porous electrodes are taken in Chapters 4 and 5. Both approaches extend fundamental electrochemical models based on the concentrated-solution theory by adding a general local thermal-energy balance. The details of the electrochemical models applied in the two cases differ, however. First, a transport model based on the Newman-Tobias porous-electrode theory is used to simulate the transient thermal response of a commercial A123 lithium-ion battery. Although this model does not include the effects of mass-transfer limitations within the battery cell, it still is found to predict the cell's thermal response within the bounds of experimental error. Second, the standard Dualfoil model of electrochemical, porous intercalation-electrode transport is implemented to include mass-transfer effects. In this case, the coupled thermal-energy balance is used to evaluate safety and performance of a high-capacity GS Yuasa lithium-ion battery.

Chapter 1 Introduction

A system can depart from equilibrium for a number of reasons: heat transfer occurs as a result of temperature gradients; fluid flow results from mechanical driving forces; charge flow arises in response to electric fields; and mass diffusion results from inhomogeneities in composition. This thesis focuses on multicomponent momentum, heat, mass, and charge transfer in various systems. I examined multicomponent mass transfer in a modified Stefan tube (chapter 2), convective mass and charge transfer in a convection battery (chapter 3), simultaneous heat and charge transfer in a 15-Ah A123 Inc. prismatic lithium-ion battery (chapter 4), and simultaneous heat, mass, and charge transfer in a 50-Ah GS-Yuasa Inc. automotive lithium-ion cell (chapter 5).

In this chapter, I introduce the Stefan-Maxwell multicomponent diffusion equation, and provide constitutive laws for chemical and electrochemical potential that form the basis for all subsequent discussions of simultaneous mass and charge transfer. In chapter 2, I discuss the simplest case of multicomponent diffusion: ternary gas diffusion in a tube. Chapter 3 shifts the focus to electrochemical transport systems. I investigate the effect of forced electrolyte flow in a traditional battery system, showing how convection alters limiting currents and can be used to improve the power delivered by the system. Chapters 4 and 5 present two different attacks on coupled thermoelectrochemical transport in porous electrodes. Chapter 4 demonstrates that adding a heat balance to a simple electrochemical model (the Newman-Tobias porous-electrode theory) can predict

the transient thermal response of lithium-ion battery accurately. Although the Newman-Tobias model does not include the effects of mass-transfer limitations within the battery cell, it still estimates the thermal response within experimental error. In Chapter 5, I show how the standard Dualfoil model can be used to include mass-transfer effects in the electrochemical modeling, using a coupled thermal-energy balance to evaluate the safety and performance of a high-capacity GS-Yuasa Li-ion battery. In the Appendix, I provide algorithms based on the Chapman-Enskog kinetic theory to estimate transport properties of gases in terms of their molecular potentials, an analysis that is a necessary first step toward closing some further questions that arise in chapter 2.

1.1 Stefan-Maxwell equation for multicomponent mass diffusion systems

Gradients of chemical (or electrochemical) potential drive mass diffusion and charge transport. In multicomponent systems, the Stefan-Maxwell equation can be used to relate mass fluxes to composition gradients [1,2]. The extended Stefan-Maxwell equation relates the gradient of chemical (or electrochemical) potential of each species, $\nabla\mu_i$, to the relative velocity of species i relative to every other species j, $\vec{v}_j - \vec{v}_i$, through a set of drag coefficients K_{ij}.

$$c_i \nabla \mu_i = \sum_{j \neq i}^{N} K_{ij} \left(\vec{v}_j - \vec{v}_i \right) = RT \sum_{j \neq i}^{N} \frac{c_i c_j}{c_{\mathrm{T}} \mathcal{D}_{ij}} \left(\vec{v}_j - \vec{v}_i \right). \tag{1.1}$$

Here c_i is the concentration of species i, N is the number of species, R is the universal gas constant, T is the absolute temperature, c_{T} is the total concentration, and $\mathcal{D}_{ij}$ is the Stefan-Maxwell coefficient parameterizing the diffusivity of species i through j. The drag

coefficient K_{ij} is inversely proportional to the binary diffusion coefficient. This equation received its name because Maxwell suggested it to describe the diffusion in a binary gas; Stefan generalized Maxwell's diffusion law to mixtures containing an arbitrary number of species [3]. Onsager justified the use of the extended Stefan-Maxwell equation using both non-equilbrium statistical mechanics and irreversible thermodynamics [4].

1.2 Chemical potential

In Stefan-Maxwell equations (1.1), $c_i \nabla \mu_i$ can be regarded as a driving force per unit volume acting on species i (it has units of force per volume). The chemical potential μ_i of an electrically neutral species relates to its activity a_i through

$$\mu_i = \mu_i^\theta + RT \ln a_i, \tag{1.2}$$

where μ_i^θ represents the chemical potential of species i in a standard state at fixed temperature, pressure, and composition. Since it depends to first order on the molar concentration c_i, the activity coefficient for species i is typically written as

$$a_i = f_i c_i = f_i c_\mathrm{T} y_i, \tag{1.3}$$

where f_i is the molar activity coefficient on a molar concentration basis, and y_i the mole fraction, of species i. Here c_T represents the total molar concentration, *i.e.*, the sum of the species concentrations. Sometimes composition is placed on a molal, mole-fraction, or mass basis, calling for different definitions of the activity coefficient, but use of equation (1.3) is standard in modern electrochemistry [5]. Equation (1.3) suffices to describe neutral constituents of solid, liquid, or gas phases. In gases, the activity coefficient from

equation (1.3) can be related to a fugacity coefficient, since c_T is proportional to pressure [6]. A component of an isobaric, isothermal ideal-gas mixture, or a solute in an ideal solution can be modeled by taking $f_i \approx 1$. That is,

$$\mu_i = \mu_i^\theta + RT \ln c_i \tag{1.4}$$

for a neutral constituent of an ideal-gas mixture or ideal solution.

Chapter 2 addresses multicomponent diffusion in an isothermal, isobaric gas, for which the Stefan-Maxwell equation can be expressed as

$$\nabla y_i = \sum_{j \neq i} \frac{y_i \overrightarrow{N_j} - y_j \overrightarrow{N_i}}{c_T \mathcal{D}_{ij}}. \tag{1.5}$$

Here $\overrightarrow{N_i}$ represents the total molar flux of species *i* relative to a stationary inertial frame,

$$\overrightarrow{N_i} = c_i \overrightarrow{v_i}. \tag{1.6}$$

The molar flux is directly measurable (as in the experiments of Carty and Schrodt [7]), and is therefore sometimes preferred to the species velocity as a basis for describing material flow.

1.3 Electrochemical potential

In Chapters 3, 4, and 5, transport models based on the Stefan-Maxwell equation are applied to electrochemical systems, requiring consideration of the electric field as a driving force for charge flow. This effect is taken into account by introducing the

electrochemical potential, which serves as a driving force for both mass and charge transfer. When species in a transport system are charged, the chemical potential is modified to account for an electrostatic potential Φ, through

$$\mu_i = \mu_i^\theta + RT \ln a_i + z_i F \Phi, \tag{1.7}$$

in which z_i is the equivalent charge carried by species i, and F is Faraday's constant. The electrochemical potential at standard state has different meaning from the standard chemical potential in equation (1.2) as well. In addition to fixed temperature and pressure, the potential must be measured relative to a standard reference electrode of a given kind at fixed composition. Guggenheim calls this a "secondary reference state" [8].

The electric current in an electrolytic solution arises from the motion of charged particles according to Faraday's law,

$$\vec{i} = F \sum_i z_i \overrightarrow{N_i}. \tag{1.8}$$

Here, $\vec{i}$ is the electric current density, expressed in units of charge per time per area. Using Faraday's law, the condition of local electroneutrality (a charge balance)

$$\sum_j z_j c_j = 0, \tag{1.9}$$

and the set of species mass balances

$$\frac{\partial c_j}{\partial t} = -\nabla \cdot \vec{N}, \tag{1.10}$$

the modified Stefan-Maxwell equations applicable to an electrochemical system comprising a binary electrolytic solution (comprising one neutral solvent and one electrolyte) of a binary electrolyte (comprising one anion and one cation) can be rearranged into flux-explicit transport laws comprising terms associated with diffusion (driven by electrolyte concentration gradients), migration (driven by the current), and convection (driven by the solvent velocity) [5],

$$\vec{N}_+ = -D\left(1 - \frac{d\ln c_0}{d\ln c}\right)\vec{\nabla}c_+ + \frac{t_+^0}{z_+F}\vec{i} + c_+\vec{v}_0, \tag{1.11}$$

$$\vec{N}_- = -D\left(1 - \frac{d\ln c_0}{d\ln c}\right)\vec{\nabla}c_- + \frac{\left(1-t_+^0\right)}{z_-F}\vec{i} + c_-\vec{v}_0, \tag{1.12}$$

where c_0 is the solvent concentration. The Fickian diffusivity D is defined in terms of Stefan-Maxwell coefficients and the activity coefficient $\ln f_{+-} = \nu_+ \ln f_+ + \nu_- \ln f_-$ as

$$D = c_T\bar{V}_0\left(1 + \frac{d\ln f_{+-}}{d\ln c}\right)_{T,p} \cdot \frac{\left(z_+ - z_-\right)\mathcal{D}_{0+}\mathcal{D}_{0-}}{z_+\mathcal{D}_{0+} - z_-\mathcal{D}_{0-}}, \tag{1.13}$$

where $\bar{V}_0$ is the partial molar volume of solvent; the cation transference number t_+^0 is defined as

$$t_+^0 = \frac{z_+\mathcal{D}_{0+}}{z_+\mathcal{D}_{0+} - z_-\mathcal{D}_{0-}}. \tag{1.14}$$

Insertion of flux laws (1.11) and (1.12) into either of the material balances (1.10) on the charged species yields a general form of Fick's second law,

$$\frac{\partial c}{\partial t} + \nabla \cdot \left(c\vec{v}_0 \right) = \nabla \cdot \left(D \nabla c \right) - \frac{\vec{i} \cdot \nabla t_+^0}{z_+ \nu_+ F} \tag{1.15}$$

Insertion of the electrochemical potential (1.7) into the Stefan-Maxwell equation for a charged species, followed by rearrangement with the flux laws (1.11) and (1.12), further yields

$$\nabla \Phi = -\frac{\vec{i}}{\kappa} - \frac{RT}{F} \sum_j \frac{t_j}{z_j} \nabla \ln c_j, \tag{1.16}$$

where κ is the conductivity, defined in terms of Stefan-Maxwell coefficients as

$$\kappa = -\frac{F^2 z_- c_- c_T \mathcal{D}_{+-}}{RT} \cdot \frac{z_+ \mathcal{D}_{0+} - z_- \mathcal{D}_{0-}}{c_0 \mathcal{D}_{+-} + c_+ \mathcal{D}_{0-} + c_- \mathcal{D}_{0+}}. \tag{1.17}$$

Equation (1.16) is a modified form of Ohm's law applicable to systems with concentration gradients, also called the MacInnes equation [9]. It relates the electric potential to the current density and the concentration distribution of ions.

Although the modified Stefan tube, the alkaline convection battery, and lithium-ion batteries are significantly different systems, the transport formulations involved are all based on the same multicomponent mass-diffusion model.

1.4 References

[1] E. N. Lightfoot, E. L. Cussler, and R. L. Rettig, "Applicability of the Stefan-Maxwell equations to multicomponent diffusion in liquids," *AIChE Journal*, vol. 8, no. 5, pp. 708–710, 1962.
[2] J. O. Hirschfelder, C. F. Curtiss, and R. B. Bird, *Molecular theory of gases and liquids*, 1964.

[3] R. B. Bird, W. E. Stewart, and E. N. Lightfoot, *Transport Phenomena, 2nd Edition*, Wiley, 2001.
[4] L. Onsager, "THEORIES AND PROBLEMS OF LIQUID DIFFUSION," *Annals of the New York Academy of Sciences*, vol. 46, no. 5, pp. 241–265, Nov. 1945.
[5] J. Newman and K. E. Thomas-Alyea, Electrochemical Systems, 3rd Edition, Wiley-Interscience, 2004.
[6] G. N. Lewis and M. Randall, *Thermodynamics*. McGraw-Hill Book Company, 1961.
[7] R. Carty and T. Schrodt, *Ind. Eng. Chem. Fundamen*. 14(3) (1975) 276-278.
[8] E. A. Guggenheim, *Thermodynamics: an advanced treatment for chemists and physicists*. North-Holland Pub. Co., 1949.
[9] D. A. MacInnes, *The Principles of Electrochemistry*. Reinhold, 1939.

Chapter 2 Multicomponent mass diffusion in the Stefan tube

As a simple introductory case, this chapter discusses the analysis of multicomponent transport within a gas mixture in a Stefan tube. A Stefan tube is an apparatus similar to an Arnold cell [1,2], in which a liquid film is allowed to evaporate into an ambient gas through a tube of fixed length; at the top of the tube, a transverse ambient gas flow convects away the evaporating solute or solutes. (The Stefan tube differs from an Arnold cell in that a large liquid reservoir is present, keeping the diffusion length constant as the liquid evaporates.) Carty and Schrodt [3] produced a modified Stefan tube in which gas-phase concentrations could be measured directly as functions of height from the liquid film. Carty and Schrodt's experiments provide an excellent direct test and illustration of the general multicomponent Stefan-Maxwell diffusion model on which most of the work in this dissertation is based. The driving forces for mass diffusion in this case are concentration gradients in the tube, which can be related to relative species fluxes by equations (1.5), using the chemical potential constitutive law from equation (1.2), under the assumption that the system is isothermal and isobaric.

Accurate gas transport properties are essential in the design and simulation of processes involving heat and mass transfer. For example, binary diffusion coefficients, viscosities, and thermal conductivities are necessary in the design of chemical reactors, and also play a crucial role in atmospheric chemistry, combustion science, studies of indoor air pollution, and aerothermodynamics [4,5]. Carty and Schrodt's modified Stefan

tube allows Stefan-Maxwell coefficients in multicomponent gases to be measured directly, by fits of model output to measured concentration profiles.

Carty and Schrodt used their model to test Stefan-Maxwell theory, using auxiliary measurements of diffusion coefficients as input parameters. Their analysis relied on some rather extreme simplifying assumptions, causing experimental and theoretical concentration profiles to differ by more than the generally acceptable experimental error. In this chapter, we demonstrate that relaxing some of Carty and Schrodt's assumptions leads to different boundary conditions on the Stefan tube, yielding a transport model that can achieve a better fit of experimental data. The deviation of experimental concentration distributions from simulations reduces dramatically when experimentally measured mass fluxes at the tube exhaust are employed directly as boundary conditions. Although the model fits data well, the question remains whether these phenomenological results agree with expectations based on our knowledge of molecular-level interactions, providing a strong motivation for future research into kinetic theory. Some preliminary analysis involving the kinetic theory of gases is provided in Appendix A of this thesis.

2.1 Carty and Schrodt's experiment

Carty and Schrodt provide concentration profiles for the modified Stefan tube during the steady-state evaporation of a methanol/acetone liquid film into ambient air [3]. The schematic diagram in Figure 2-1 depicts the experimental setup. The liquid reservoir contains a solution of acetone and methanol, which has constant concentration and interfacial position throughout a given measurement. The vertical position from the liquid

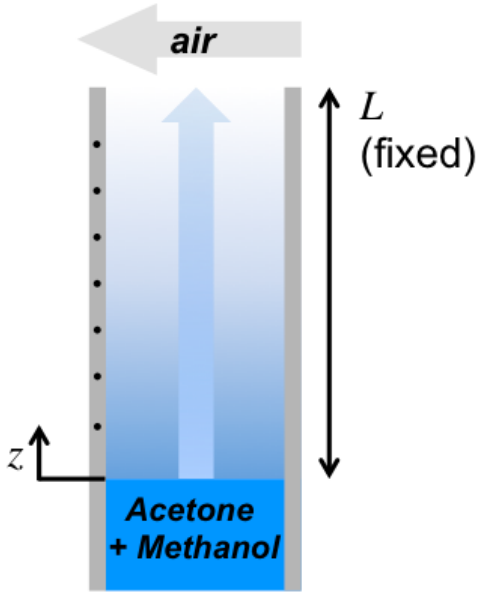

Figure 2-1 A schematic of a modified Stefan tube used in the Carty and Schrodt experiment [3]

surface is designated by z. Dry air flows across the tube's aperture at position $z = L$, fixing the mole fractions y_i of acetone (species a), methanol (species b), and air (species c) at the tube outlet,

$$y_a \approx 0, \quad y_b \approx 0, \quad \text{and} \quad y_c \approx 1 \quad \text{at} \quad z = L. \tag{2.1}$$

A difference in solute mole fraction between the gas at the liquid surface and the ambient flow-by stream at the tube outlet drives acetone and methanol to diffuse in the z-direction. The actual tube length used by Carty and Schrodt was $L = 24.25$ cm. Transport was assumed to be one-dimensional (for reference, the tube diameter was $D = 5.08$ cm). Seven sealable pinholes along the tube, connected by a piping manifold to a gas chromatograph, permitted composition analysis after the concentration profiles in the tube had reached steady state. The points on the graph in Figure 2-2 show Carty and Schrodt's steady-state concentration measurements.

2.2 Governing equations

Carty and Schrodt also developed an analytical solution to the Stefan-Maxwell equations and presented theoretical concentration profiles alongside their experimental composition data. To explore the validity of the boundary conditions they employed, we will lay out the complete system of material balances and flux laws here. An interior point in an isothermal, isobaric, three-component ideal-gas diffusion system at steady state is modeled by the following five equations:

$$\nabla \cdot \overrightarrow{N_a} = 0, \tag{2.2}$$

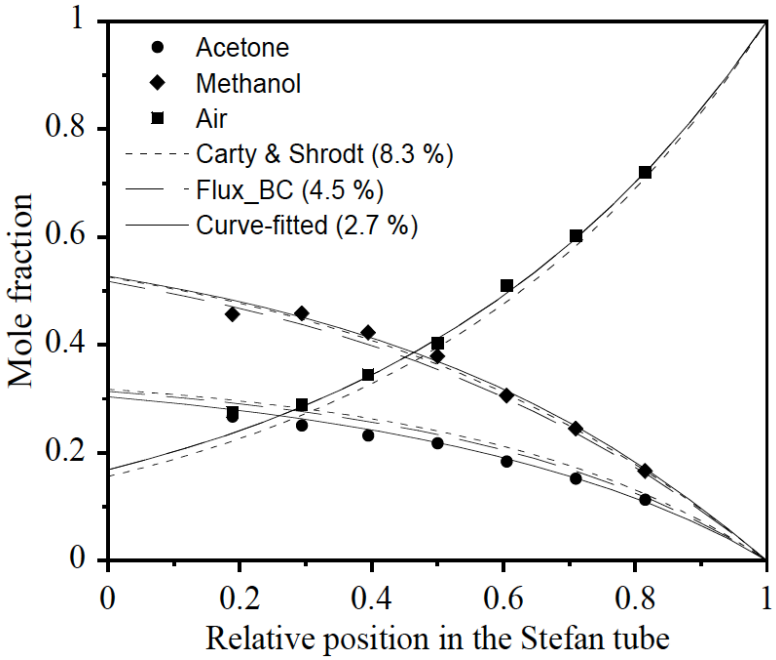

Figure 2-2 Mole fractions of acetone (●), methanol (◆) and air (■) in a modified Stefan tube. Carty and Schrodt's theoretical concentration profiles [3] are represented as dotted lines; our results using Carty and Schrodt's Stefan-Maxwell coefficients with a flux boundary condition are shown as dashed lines; the result of a best fit wherein all the transport properties were allowed to vary is shown by solid lines.

$$\nabla \cdot \overrightarrow{N_{\mathrm{b}}} = 0, \tag{2.3}$$

$$\nabla \cdot \overrightarrow{N_{\mathrm{c}}} = 0, \tag{2.4}$$

$$\nabla y_{\mathrm{a}} = \sum_{j \neq \mathrm{a}} \frac{y_{\mathrm{a}} \overrightarrow{N_j} - y_j \overrightarrow{N_{\mathrm{a}}}}{c_{\mathrm{T}} \mathcal{D}_{\mathrm{a}j}}, \tag{2.5}$$

$$\nabla y_{\mathrm{b}} = \sum_{j \neq \mathrm{b}} \frac{y_{\mathrm{b}} \overrightarrow{N_j} - y_j \overrightarrow{N_{\mathrm{b}}}}{c_{\mathrm{T}} \mathcal{D}_{\mathrm{b}j}}. \tag{2.6}$$

Recall that $\overrightarrow{N_i}$ is the molar flux of species *i* relative to a stationary reference frame; c_{T} represents the total concentration ($c_{\mathrm{T}} = p/RT$ for an ideal gas at constant pressure p and temperature T). Equations (2.2), (2.3), and (2.4) are material balances; in the steady state there is no accumulation; in the absence of homogeneous chemical reactions no generation terms appear. Equations (2.5) and (2.6) are the independent Stefan-Maxwell equations. (The isothermal, isobaric Gibbs-Duhem equation

$$\sum_i c_i \nabla \mu_i = \vec{0} \tag{2.7}$$

shows that only two diffusion driving forces in a ternary system are linearly independent, justifying the use of only two Stefan-Maxwell equations for ternary diffusion.) Composition in an isothermal, isobaric single phase is also constrained by the Gibbs phase rule. With species mole fractions as a basis for composition, the dependence of one species concentration on the others is described by the simple characteristic equation

$$\sum_j y_j = 1, \tag{2.8}$$

which clearly constrains the mole fractions. After calculating y_a and y_b by integrating the governing system, the distribution of air can be found using equation (2.8).

2.2.1 Boundary conditions

For the one-dimensional geometry depicted in Figure 2-1, equations (2.2)–(2.6) are first-order ordinary differential equations (ODEs). Five independent boundary conditions are needed to close the problem. In accord with equation (2.8), equation (2.1) provides two linearly independent boundary conditions. Following from integration of equation (2.4), a third boundary condition is found:

$$\left\|\vec{N}_c\right\| = N_c = 0 \qquad \text{at} \quad z = 0. \tag{2.9}$$

(This equation introduces the simplified notation N_i to represent the flux component of species i in the z direction.) Physically this makes sense, since the liquid surface is not permeable to air. Note that equation (2.9) does not prevent air from maintaining a concentration gradient in the tube.

Carty and Schrodt used two additional boundary conditions to close the set of equations. Direct measurements of the steady-state acetone and methanol fluxes in the z direction (N_a and N_b) were available to them: values of $N_a = 1.779 \times 10^{-7}$ mol·cm^2·s^{-1} and $N_b = 3.121 \times 10^{-7}$ mol·cm^2·s^{-1} were computed based on knowledge of the ambient-air flow rate and composition at the flow-system exhaust.

Rather than using the flux information, however, Carty and Schrodt used the conventional wisdom that the kinetics of evaporation is slow in comparison to diffusion, which suggests that the acetone and methanol mole fractions at the reservoir surface can be determined through vapor-liquid equilibrium (VLE) data. Thus they used boundary conditions

$$y_a(z=0) = y_a^0, \tag{2.10}$$

$$y_b(0) = y_b^0, \tag{2.11}$$

with a superscript 0 indicating the value of a property at the liquid surface. The VLE data of Freshwater and Pike suggest that for the liquid composition used by Carty and Schrodt, $y_a^0 = 0.3173$, $y_b^0 = 0.5601$, and $y_c^0 = 0.1227$ [6]. The surface compositions will be maintained as variables in this analysis, to simplify further discussion in chapter 2.4.1.

2.3 Carty and Schrodt's analytic solution and deviations from experimental data

Carty and Schrodt analyzed the problem as follows. Directly integrate equations (2.2) through (2.4) to show that the molar fluxes of all species are constant with respect to position in the steady state. Then apply equation (2.9); since there is no flux of air through the liquid surface at the bottom of the tube, it follows that the total air flux must vanish throughout the tube. These conditions reduce the governing system to two first-order differential equations:

$$c_{\mathrm{T}}\frac{dy_{\mathrm{a}}}{dz}=y_{\mathrm{a}}\left(\frac{N_{\mathrm{b}}}{\mathscr{D}_{\mathrm{ab}}}+\frac{N_{\mathrm{a}}+N_{\mathrm{c}}}{\mathscr{D}_{\mathrm{ac}}}\right)-y_{\mathrm{b}}\left(\frac{N_{\mathrm{a}}}{\mathscr{D}_{\mathrm{ab}}}-\frac{N_{\mathrm{a}}}{\mathscr{D}_{\mathrm{ac}}}\right)-\frac{N_{\mathrm{a}}}{\mathscr{D}_{\mathrm{ac}}}, \tag{2.12}$$

$$c_{\mathrm{T}}\frac{dy_{\mathrm{b}}}{dz}=-y_{\mathrm{a}}\left(\frac{N_{\mathrm{b}}}{\mathscr{D}_{\mathrm{ab}}}-\frac{N_{\mathrm{b}}}{\mathscr{D}_{\mathrm{bc}}}\right)+y_{\mathrm{b}}\left(\frac{N_{\mathrm{a}}}{\mathscr{D}_{\mathrm{ab}}}+\frac{N_{\mathrm{b}}+N_{\mathrm{c}}}{\mathscr{D}_{\mathrm{bc}}}\right)-\frac{N_{\mathrm{b}}}{\mathscr{D}_{\mathrm{bc}}}. \tag{2.13}$$

(The Onsager reciprocal relation $\mathscr{D}_{ij}=\mathscr{D}_{ji}$ [7] has been applied to simplify these expressions.) This system can be integrated directly from 0 (where equations (2.12) and (2.13) hold) to z, yielding closed-form distributions of methanol and acetone:

$$y_{\mathrm{a}}=\frac{\left(\mathscr{D}_{\mathrm{ab}}\lambda_{-}-\mathscr{D}_{\mathrm{bc}}\lambda_{+}\right)\left\{\mathscr{D}_{\mathrm{ab}}\left(-e^{\lambda_{-}(1-z/L)}+e^{\lambda_{+}(1-z/L)}\right)\lambda_{-}+\mathscr{D}_{\mathrm{ac}}\left[\lambda_{-}-e^{\lambda_{+}(1-z/L)}\lambda_{-}+\left(-1+e^{\lambda_{-}(1-z/L)}\right)\lambda_{+}\right]\right\}}{\mathscr{D}_{\mathrm{ab}}\left(\mathscr{D}_{\mathrm{ac}}-\mathscr{D}_{\mathrm{bc}}\right)\lambda_{-}\left(\lambda_{-}-\lambda_{+}\right)}, \tag{2.14}$$

$$y_{\mathrm{b}}=\frac{\left(\mathscr{D}_{\mathrm{ab}}\lambda_{-}-\mathscr{D}_{\mathrm{ac}}\lambda_{+}\right)\left\{\mathscr{D}_{\mathrm{ab}}\left(-e^{\lambda_{-}(1-z/L)}+e^{\lambda_{+}(1-z/L)}\right)\lambda_{-}+\mathscr{D}_{\mathrm{bc}}\left[\lambda_{-}-e^{\lambda_{+}(1-z/L)}\lambda_{-}+\left(-1+e^{\lambda_{-}(1-z/L)}\right)\lambda_{+}\right]\right\}}{\mathscr{D}_{\mathrm{ab}}\left(-\mathscr{D}_{\mathrm{ac}}+\mathscr{D}_{\mathrm{bc}}\right)\lambda_{-}\left(\lambda_{-}-\lambda_{+}\right)}, \tag{2.15}$$

where

$$\lambda_{+}=-\frac{N_{\mathrm{a}}}{\mathscr{D}_{\mathrm{ac}}}-\frac{N_{\mathrm{b}}}{\mathscr{D}_{\mathrm{bc}}}, \tag{2.16}$$

$$\lambda_{-}=-\frac{N_{\mathrm{a}}+N_{\mathrm{b}}}{\mathscr{D}_{\mathrm{ab}}}. \tag{2.17}$$

These results depend on two surface concentrations (y_{a}^{0} and y_{b}^{0}) and two fluxes (N_{a} and N_{b}). The concentrations at the top of the tube are then given by evaluating these results at L, yielding

$$y_a(L) = y_a^L = 0, \tag{2.18}$$

$$y_b(L) = y_b^L = 0. \tag{2.19}$$

Of the six parameters (y_a^0 , y_b^0 , y_a^L , y_b^L , N_a and N_b) involved in equations (2.14) through (2.19), any four can be specified by boundary conditions; the remaining two are then specified self-consistently through algebraic equations (2.18) and (2.19). Carty and Schrodt used boundary conditions (2.9), (2.10), (2.11), (2.18), and (2.19), making the fluxes dependent variables whose values were determined through self-consistency conditions $y_i^L = 0$ (excluding air). We will explore a number of alternative choices here.

In order to draw the concentration distributions in Figure 2-2, binary diffusion coefficients are also needed. The binary diffusion coefficients of acetone in air, $\mathcal{D}_{ac}$, and of methanol in air, $\mathcal{D}_{bc}$, are experimentally available. Literature values are $\mathcal{D}_{ac} = 0.1372$ cm^2/s and $\mathcal{D}_{bc} = 0.1991$ cm^2/s [8,9]. The diffusion coefficient of acetone through methanol in the presence of air, $\mathcal{D}_{ab}$, is not as readily available. Carty and Schrodt estimated the value using kinetic theory: $\mathcal{D}_{ab} = 0.0848$ cm^2/s [10].

The dotted line in Figure 2-2 shows the analytical solution for the concentration profiles based on boundary conditions (2.9), (2.10), (2.11), (2.18), and (2.19) reported by Carty and Schrodt. To test the consistency of their result, Carty and Schrodt also calculated the fluxes of acetone and methanol using equations (2.18), and (2.19), finding them to be $N_a = 1.781 \times 10^{-7}$ mol·cm^2·s^{-1} and $N_b = 3.186 \times 10^{-7}$ mol·cm^2·s^{-1}, in fair agreement with their measured fluxes N_a and N_b, which deviated by 0.11% and 2.1% from the computed values, respectively. Agreement with experimental mole-fraction

distributions was significantly worse than that with the flux data: mole fractions at the seven sampling points along the Stefan tube deviated by 8.3%, greater than the intrinsic measurement error. To investigate this discrepancy, and to develop finite-difference algorithms that could be benchmarked against analytical solutions, we developed a computer program to solve equations (2.2)–(2.6) with a variety of boundary conditions.

The computer program was developed to solve the coupled ordinary governing equations (2.2)–(2.6) using an implicit finite-difference scheme. Initially, the solution by Carty and Schrodt was duplicated using three natural boundary conditions: equation (2.9) two measured steady-state fluxes ($N_a = 1.779 \times 10^{-7}$ mol·cm^2·s^{-1} and $N_b = 3.121 \times 10^{-7}$ mol·cm^2·s^{-1}), and two surface-concentration boundary conditions, (2.10) and (2.11). The result was satisfactory: the difference between this result and Carty and Schrodt's analytic solution was found to be less than the numerical error of the program ($\epsilon = 10^{-12}$). This result showed that the computer program was working properly, and provided a basis for further investigations into the sources of discrepancies between theoretical results and Carty and Schrodt's experimental data.

2.4 Possible sources of error in Carty and Schrodt's analysis

2.4.1 Calculated interfacial concentrations as boundary conditions

One possible source of the error in the Carty and Schrodt's data fitting was the use of VLE data as boundary conditions at the liquid surface. VLE data is, by definition, measured at equilibrium; it is possible that the vapor composition at the liquid surface could differ significantly from the VLE data in the dynamic steady-state condition of

Carty and Schrodt's experiment. Alternatively, slight changes in temperature at the liquid surface due to evaporation, imprecision of the ambient temperature, or slight relative humidity could cause the actual surface VLE to differ from the literature data.

To relax the restriction placed by the VLE data at the liquid surface, the governing equations were solved using alternative boundary conditions. Instead of equations (2.10) and (2.11), experimentally measured fluxes were used as liquid-surface boundary conditions. The resulting deviation from experimental mole-fraction profiles was somewhat less; the deviation of the acetone concentration stayed high, at 6.8%.

2.4.2 Calculated binary diffusion coefficient of acetone and methanol

Another possible source of discrepancy between Carty and Schrodt's model output and experimental data is the value used for the binary diffusion coefficient of acetone in methanol, $\mathcal{D}_{ab}$, which was estimated based on kinetic theory [10]. To check this error source, we took our investigation a step further: using the experimental fluxes as boundary conditions, $\mathcal{D}_{ab}$ was determined by a least-squares curve-fitting process, using the experimental concentration profiles and two experimental values for $\mathcal{D}_{ac}$ and $\mathcal{D}_{bc}$ [8,9]. The best-fit process was repeated with other boundary conditions as well, to investigate coupled effects of the assumptions. The smallest deviation from the experimental concentration profiles, 2.7% (see Figure 2-2 and Table 2-1), was found when experimental fluxes were directly used as the boundary conditions. This process yielded a $\mathcal{D}_{ab}$ value of 0.0214 cm^2/s.

Although the fit of the concentration profiles was improved by this method, the result also leads to further questions. The acetone/methanol Stefan-Maxwell diffusivity

Boundary condition	Fixed $\mathcal{D}_{ab}$		Curve-fitted $\mathcal{D}_{ab}$	
	$\mathcal{D}_{ab}$ (cm^2/s)	%	$\mathcal{D}_{ab}$ (cm^2/s)	%
y_a, y_b @ interface (VLE data)	0.0848	8.3%	0.0113	5.2%
N_a, N_b (experiment)	0.0848	4.5%	0.0214	2.7%

Table 2-1 Average percent deviations between experimental data and theory, using different boundary conditions and different acetone/mehtanol diffusion coefficients.

that best fit the experimental data is a factor of four smaller than the theoretical value given by Carty and Schrodt.

2.5 Discussion/steps to gas kinetic theory

One further concern is that Carty and Schrodt's analysis was based on an unrealistic assumption that air is a single-component gas, whereas air is actually a mixture of nitrogen (78%), oxygen (21%), argon (< 1%), *etc*. To examine the impact of this simplification, we generalized our computer program to model Stefan-Maxwell diffusion of an arbitrary number of components. A logical test would be to use five components: acetone, methanol, nitrogen, oxygen, and argon. However, this approach requires ten binary diffusion coefficients, several of which have not been previously reported. Experiments would be an ideal way to obtain them – but appropriate numerical methods for property estimation would be preferable, saving both time and effort.

One method to evaluate transport properties like thermal conductivity, viscosity, and diffusion coefficients within dilute gases is to exploit the Chapman-Enskog solution to the Boltzmann gas equation [11-14]. In this method, transport coefficients are given as functions of collision integrals. The particles are modeled as a group of colliding pairs, which obey classical momentum and energy conservation laws through an intermolecular potential that expresses the attractive and repulsive forces exerted by the particles. Once collision integrals are known for a given potential function, and the intermolecular potentials for given species are parameterized, the estimation of gas properties over wide ranges of composition becomes possible. Very accurate calculations of collision integrals, as well as transport properties for some single-component gases, are reported in

Appendix A. The groundwork for future analysis of multicomponent transport scenarios is therefore present. Since the calculations necessary to compute Stefan-Maxwell coefficients require parameterization of intermolecular pair potentials, this effort will provide a substantial project for future research.

2.6 References

[1] J. H. Arnold, "Studies in diffusion: III. Unsteady-state vaporization and absorption," Transactions of the American Institute of Chemical Engineers, vol. 40, no. 3, pp. 0361–0378, Jun. 1944.
[2] E. L. Cussler and E. N. Lightfoot, "Multicomponent diffusion in restricted systems," AIChE Journal, vol. 9, no. 5, pp. 702–703, 1963.
[3] R. Carty and T. Schrodt, *Ind. Eng. Chem. Fundamen.* 14(3) (1975) 276-278.
[4] G. Colonna and A. Laricchiuta, *Computer Physics Communications* 178, 809 (2008).
[5] R. Eslamloueyan and M. Khademi, *Chemometrics and Intelligent Laboratory Systems* 104, 195 (2010).
[6] D. C. Freshwater and K. A. Pike, "Vapor-liquid equilibrium data for systems of acetone-methanol-isopropanol," *Journal of Chemical & Engineering Data*, vol. 12, no. 2, pp. 179–183, Apr. 1967.
[7] C. W. Monroe and J. Newman, "Onsager Reciprocal Relations for Stefan–Maxwell Diffusion," *Industrial & Engineering Chemistry Research*, vol. 45, no. 15, pp. 5361–5367, Jul. 2006.
[8] J. Richardson, *Chem. Eng. Sci.* 10 (1959) 234-242.
[9] R. Mrazek, C. Wicks, and K. Prabhu, *J. Chem. Eng. Data* 13 (1968) 508-510.
[10] J. Bae and T. Reed III, *Ind. Eng. Chem. Fundamen.* 10 (1971) 36-41.
[11] S. Chapman and T. Cowling, 2nd Ed. Cambridge, 1960.
[12] J. Hirschfelder, R. Bird, and E. Spotz, *J. Chem. Phys.* 16 (1948) 968-981.
[13] J. Hirschfelder, C. Curtiss, and R. Bird, Wiley, New York, 1954.
[14] E. Akhmatskaya and L. Pozhar, *USSR Comput. Maths. Math. Phys.* 26(2) (1986) 185-190.

Chapter 3 Increasing the rate capability of batteries with electrolyte flow

This chapter shifts the focus to transport in electrochemical systems. In addition to the mass balances and transport equations from chapter 2, analysis of electrochemical systems also requires a local charge balance, which requires that electrical state variables be introduced to the Stefan-Maxwell theory. The electric potential (voltage) is introduced within Stefan-Maxwell theory through the electrochemical potential constitutive law from equation (1.7). Voltage gradients (or current flow) provide a driving force for 'migration', defined as the motion of charged species due to the action of an externally imposed electric field. The current density is introduced as a variable describing charge flux through Faraday's law (1.8). A suitable charge balance is supplied by the electroneutrality condition (1.9), since the volume elements under consideration in typical transport systems are very large in comparison to the Debye length. Under these typical model conditions, the modified Stefan-Maxwell equation yields the equations used to describe mass transport in isothermal, isobaric binary electrolytes (the 'concentrated-solution theory' of Newman [1]), equations (1.8) through (1.15). Transport modeling in the remainder of this thesis is based on concentrated-solution theory.

In this chapter, I investigate the effect of forced electrolyte convection on the performance of traditional zinc/manganese-oxide alkaline batteries. A theoretical analysis describes how electrolyte flow driven through a battery cell alters its efficiency and power, as in the 'convection battery' configuration recently proposed by Suppes *et al*.

[2,3]. Concentrated-solution theory rationalizes the observation that imposition of electrolyte flow parallel to the current through a separator can reduce overpotential losses, and is used to quantify the overpotential reduction in terms of the flowrate and physical properties of the electrolyte and separator. The model results are consistent with the experimental observations of alkaline convection batteries by Suppes *et al*. It is notable that relatively low flowrates in convection batteries allow fine-tuned control over their limiting currents. Thus it appears that current-coaxial flow could be used to permit very high charge rates in rechargeable convection-battery cells.

3.1 Introduction

In 2011, Suppes *et al*. proposed the 'convection-battery' configuration [2,3], defined as a system in which a pump drives electrolyte flow through a battery cell. The cell is constructed like a typical cylindrical packed-bed reactor, but with separate layers of packing for the anode, separator, and cathode. Experiments by the Suppes group showed that a convection battery's output voltage at a given state of charge was elevated by electrolyte flow. In this chapter, convection-battery separators are analyzed to rationalize how flow reduces the voltage losses across them. More importantly, electrolyte flow through a separator is shown to increase its tolerance for high electric currents. This increased rate capability could allow major reductions in the durations of charge or discharge periods. Rechargeable convection batteries could be particularly useful for automotive applications, where it may be possible to exploit electrolyte flow to reduce significantly the period needed to charge a high-energy battery pack.

The primary sources of voltage loss in a traditional battery are mass transfer and reaction kinetics. Either of these effects can be rate limiting during high-current operation of the battery cell. This work focuses on mass-transfer effects.

Much research has focused on using convection to reduce mass-transfer limitations within porous electrodes. The flow direction used to force convection within electrodes is usually either exactly perpendicular to or exactly parallel to the ionic current—operational modes that here will be called 'current-perpendicular flow' and 'current-coaxial flow', respectively. (In electrolyzer or porous-electrode design, these are sometimes called 'flow-by' and 'flow-through' configurations.) Alkire and Gracon [4] combined theory and experiment to show that current-coaxial flow allows porous electrodes to operate at higher current, presumably by regulating the rate of reactant supply. In the redox-flow-battery literature, experiments have also shown that an increased current-perpendicular electrolyte flowrate causes a corresponding increase in the maximum current an electrode can support [5-9]. Trainham and Newman [10] provided modeling to compare the current/voltage responses and economics of both flow-through and flow-by electrode designs for flow batteries.

A convection battery differs from a typical electrolyzer or flow-battery cell in that current-coaxial convective flow is driven through the separator domain, as well as through the electrodes. To the best of our knowledge, no previous studies have analyzed how the convection-battery configuration impacts mass-transfer limitations in separators. The analysis here aims to assess whether forced convection through separator domains can allow cells to sustain higher currents, and consequently, to deliver—or, in secondary (rechargeable) batteries, receive—higher power.

The limiting current—the current that causes the charge-carrier concentration to vanish at one of the electrode/separator boundaries—measures the upper bound of the charge or discharge rate that a separator can tolerate. Below, a model is developed to rationalize how changes in electrolyte flowrate can affect a convection battery separator's limiting current, and to quantify the differences in concentration overpotential that arise from electrolyte flow.

Almost any traditional battery can in principle be built in a convection-battery configuration. Limited experimental data exists in the literature for the validation of theoretical models of convection batteries, however. To allow comparison between model results and experiments, this work will focus on the primary alkaline convection battery used by Suppes *et al*. [2,3]. The alkaline convection-battery system is a logical choice for modeling because discharge data (both with and without electrolyte flow) are available in the literature; furthermore, the alkaline electrolyte's transport properties are well known.

A schematic diagram of a primary alkaline convection battery is provided in Figure 3-1, which also shows the half-reactions that occur in the anode and cathode during discharge with a 2 M aqueous KOH electrolyte.[1] To permit current-coaxial convection throughout, the battery cell is constructed in a packed-bed configuration, wherein the electrodes comprise pellets of solid active materials (Zn and MnO_2) and the

[1] The cathodic reaction mechanism of the alkaline Zn/MnO_2 battery has been observed to change during operation at high power, a condition that may cause performance to be limited by electrode kinetics [11]. Since the main focus here is the rate capability of separators, it is assumed for simplicity that the reactions shown on Figure 3-1 occur at all discharge currents. A change in reaction mechanism alters the value of ΔV_{rxn} in the separator's boundary conditions (*cf*. Equations. (3.6) and (3.8)), but this effect is usually negligible, as discussed after Equation (3.17).

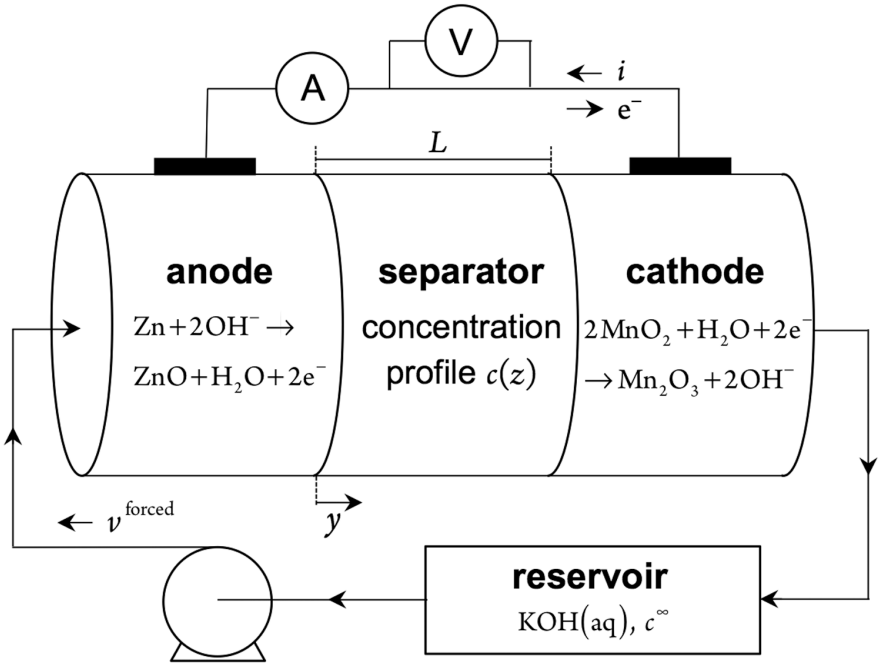

Figure 3-1 Schematic diagram of an alkaline convection-battery cell [2,3]. Reproduced form reference 12.

separator is an electrically insulating packing material (such as glass beads or a thin porous membrane). A large, well-mixed reservoir of electrolyte resides outside the cell, and is pumped through the packed bed while the battery discharges. Suppes *et al*. measured how overpotential in this configuration decreases when current-coaxial electrolyte flow is imposed. For a cell with 1.27 cm^2 cross section discharging into a load of 550 Ω, potential losses with flow were 10–50 mV less than they were without it.

The following analysis generally describes separators under current-coaxial flow, with the specific aim of rationalizing the observations Suppes *et al*. made for primary Zn/MnO_2 convection batteries. The separator's limiting current is found to be very sensitive to the Péclet number of the flow, suggesting that one can manipulate the rate capability of convection-battery separators significantly with very low electrolyte flow velocities. Although validated by data from an alkaline battery, the conclusions made here should apply to packed-bed plug-flow convection batteries in general, as long as transport in the separator is the main factor limiting cell performance.

3.2 Model formulation

3.2.1 Boundary conditions

In all batteries electric currents drive interfacial reactions, which induce flux of material through the separator. In traditional batteries, bulk flow of the electrolyte toward or away from the electrode can arise from the volume change that occurs as the cell reaction proceeds from reactants to products, but this effect is usually insignificant. (Although not driven by buoyancy, this electrochemical phenomenon is commonly called

'free convection' [13].) The fundamental distinction of the convection-battery configuration is that bulk flow of the electrolyte is driven through the separator by a pump, inducing an additional, convective flux of charge carriers – 'forced convection' – normal to the electrode/separator interfaces. For species j, let $\vec{N}_j^{\text{rxn}}$ represent the part of molar flux that arises from heterogeneous reactions, and $\vec{N}_j^{\text{forced}}$, the part that owes to forced convection.

Interfacial fluxes arising from heterogeneous reactions can be described following the approach established by Newman and Thomas-Alyea [1]. A general half-reaction is written as

$$\sum_j s_j \mathrm{M}_j^{z_j} \rightarrow n\mathrm{e}^-, \tag{3.1}$$

where M_j is the chemical formula of species j, z_j its equivalent charge, and s_j its stoichiometric coefficient in the reaction. (For a half-reaction written as a reduction, s_j is positive for a product and negative for a reactant.) Conservation of charge mandates that the number of electrons in the reaction, n, should satisfy

$$z_{e^-} n = \sum_j s_j z_j, \tag{3.2}$$

where $z_{\mathrm{e}^-} = -1$ equivalent/mole is the equivalent charge of electrons. In accord with Faraday's law, the total species flux $\vec{N}_j$ through a location on the separator boundary (labeled with the subscript 'surf') is

$$\left(\vec{N}_j \cdot \vec{n}\right)\Big|_{\text{surf}} = \left[\left(\vec{N}_j^{\text{forced}} + \vec{N}_j^{\text{rxn}}\right) \cdot \vec{n}\right]_{\text{surf}} = \left[\left(c_j \vec{v}^{\text{forced}} + \frac{s_j \vec{i}}{F z_{e^-} n}\right) \cdot \vec{n}\right]_{\text{surf}}, \tag{3.3}$$

where $\vec{n}$ is a surface normal vector, c_j is the interstitial molar concentration of species *j* in the electrode's pores, $\vec{v}^{\text{forced}}$ is the convective velocity, $\vec{i}$ is the current density, and *F* is Faraday's constant.

The convective velocity $\vec{v}^{\text{forced}}$ introduced in equation (3.3) has a subtle definition. Species fluxes through the separator depend on the rates of both reaction and convection, but it is intuitively clear that one can control the convective velocity (driven mechanically) independently of the current (driven electrically); $\vec{v}^{\text{forced}}$ represents only the independently variable portion of the bulk velocity, which does not exactly identify with standard reference velocities for convection. One example of a standard reference velocity is the volume-average velocity $\vec{v}^{\blacksquare}$, defined as

$$\vec{v}^{\blacksquare} = \sum_j c_j \overline{V}_j \vec{v}_j = \sum_j \overline{V}_j \vec{N}_j, \tag{3.4}$$

where $\vec{v}_j$ is the velocity of component *j* and $\overline{V}_j$ is its partial molar volume. Note that $c_j \overline{V}_j$ represents the local volume fraction of component *j* in the solution.

Through equation (3.3), $\vec{v}^{\text{forced}}$ can be related to the more familiar reference velocity $\vec{v}^{\blacksquare}$. Substitution of equation (3.3) into equation (3.4), followed by summation over all species and application of the isothermal, isobaric state equation

$$\sum_j c_j \bar{V}_j = 1, \tag{3.5}$$

yields

$$\left(\vec{v}^{\,\text{forced}} \cdot \vec{n}\right)\Big|_{\text{surf}} = \left[\left(\vec{v}^{\,\blacksquare} + \frac{\vec{i}}{nF}\Delta\bar{V}_{\text{rxn}}\right)\cdot\vec{n}\right]_{\text{surf}}. \tag{3.6}$$

Thus the forced-convection velocity relates to the volume-average flow velocity in the separator, but is corrected for the change in the liquid volume induced by heterogeneous reactions across the separator boundaries,

$$\Delta\bar{V}_{\text{rxn}} = \sum_k \bar{V}_k s_k. \tag{3.7}$$

If the electrolyte concentration is fairly uniform in the electrode (a reasonable assumption at sufficient flowrates [4,10]) and the reservoir is well mixed, then at the separator's boundaries each species concentration matches its concentration in the reservoir, c_j^{∞}. With these restrictions the simpler boundary condition

$$\left(\vec{N}_j \cdot \vec{n}\right)\Big|_{\text{surf}} = \left[\left(c_j^{\infty}\vec{v}^{\,\blacksquare} - \frac{\vec{i}}{nF}s_j + \frac{\vec{i}}{nF}c_j^{\infty}\Delta\bar{V}_{\text{rxn}}\right)\cdot\vec{n}\right]_{\text{surf}} \tag{3.8}$$

describes material flux through a porous electrode/separator interface when current flow and current-coaxial forced convection both occur. (Note that when there are mass-transfer limitations within the electrode domains, c_j^{∞} in equation (3.8) must be replaced by the concentration of *j* at the interface between the electrode and the separator, which generally differs from its concentration in the reservoir.)

3.2.2 Flux laws and balance equations

Aqueous KOH has been used as the electrolyte in alkaline convection batteries [2,3]. Thus one can readily employ the concentrated-solution theory for binary electrolytic solutions, for which ionic flux laws have been derived in terms of excess fluxes relative to $\vec{v}^{\blacksquare}$ [14]. The standard transport properties for binary electrolytes include transference numbers t_+^0 and $t_-^0 = 1 - t_+^0$, which parameterize cationic and anionic migration, respectively, and a diffusivity D, which parameterizes bulk electrolyte diffusion (*cf.* equations (1.13) and (1.14)). (For simplicity these properties are assumed constant with respect to composition.)

Since the separator is a porous medium, the transport equations should be further modified to account for porosity ϵ, finally yielding general ionic flux laws

$$\frac{\vec{N}_j}{\epsilon} = \frac{t_j^0}{\epsilon z_j F}\vec{i} - D\sqrt{\epsilon}\vec{\nabla}c_j + c_j\frac{\vec{v}^{\blacksquare}}{\epsilon} \qquad j = +,-. \tag{3.9}$$

Here division of superficial fluxes by ϵ converts them to interstitial values [15]; multiplication by $\sqrt{\epsilon}$ applies the Bruggeman correction for tortuosity to D [16]. An explicit flux law for solvent ($j = 0$) is unnecessary; it follows from kinematic relations. Within equation (3.9), $\vec{v}^{\blacksquare}$ is treated as a superficial velocity. (All fluxes through porous media will be treated as superficial in this work, a distinction that is also important for the analyses in chapters 4 and 5.)

Since the stoichiometric coefficients ν_j in a formula unit of electrolyte satisfy

$$z_+ \nu_+ + z_- \nu_- = 0, \tag{3.10}$$

and since local electroneutrality (equation (1.9)) holds, either of the ion concentrations can be expressed in terms of a total local electrolyte concentration

$$c = \frac{c_+}{\nu_+} = \frac{c_-}{\nu_-}. \tag{3.11}$$

Electroneutrality further implies that the current density is locally solenoidal,

$$\vec{\nabla} \cdot \vec{i} = 0. \tag{3.12}$$

Assuming plug flow and a one-dimensional geometry in the *y* direction (*cf.* Figure 3-1), insertion of equation (3.9) into either transient ion balance

$$\frac{\partial c}{\partial t} = -\vec{\nabla} \cdot \vec{N}, \tag{3.13}$$

followed by the assumption of local electroneutrality (1.9), yields a form of the convective diffusion equation that holds throughout the separator domain,

$$\frac{\partial c}{\partial t} + v \blacksquare \frac{\partial c}{\partial y} = \epsilon \sqrt{\epsilon} D \frac{\partial^2 c}{\partial y^2}. \tag{3.14}$$

This material balance equation describes convective diffusion in electrochemical systems. Either ion balance also implies the auxiliary integral condition

$$c^\infty L = \int_0^L c(t,y)\, dy. \tag{3.15}$$

The system of equations (3.8), (3.9), (3.14), and (3.15) generally describes transient diffusion in convection-battery separators when the electrolyte concentrations in the electrode domains match the concentration in the reservoir (*cf.* Figure 3-1).

A general assessment of separator performance can be provided by an analysis of the governing system at steady state, which allows the separator's limiting current to be determined. To establish the steady-state concentration distribution in the separator, equation (3.14) can be solved with

$$\frac{\partial c}{\partial t} = 0, \tag{3.16}$$

subject to the boundary condition found by substituting equation (3.9) into equation (3.8), along with the integral constraint expressed by equation (3.15).

3.2.3 Non-dimensionalization

Adoption of dimensionless quantities reveals some critical parameters that control the overall physics. Let

$$\xi = \frac{y}{L},\ \theta = \frac{c}{c^{\infty}},\ \mathrm{Pe} = \frac{v^{\blacksquare} L}{2\epsilon\sqrt{\epsilon} D},\ \text{and}\ I = \frac{iL}{2\epsilon\sqrt{\epsilon} F D c^{\infty}} \left(\frac{t_+^0}{\nu_+ z_+} - \frac{s_+}{\nu_+ z_{e^-} n} + \frac{c^{\infty}}{z_{e^-} n} \Delta \overline{V}_{\mathrm{rxn}} \right) \tag{3.17}$$

represent the dimensionless position in the separator region ξ, ion concentration θ, dimensionless fluid velocity Pe (a modified Péclet number), and dimensionless current density I. On the basis that $c^{\infty} \Delta \overline{V}_{\mathrm{rxn}}$ tends to be very small in comparison to transference numbers, it is typically reasonable to assume that

$$\Delta\bar{V}_{\text{rxn}} \approx 0. \tag{3.18}$$

(This assumption is not as strict as the assumption of extreme dilution, which has the same consequence, but is much more restrictive on the applicability of the transport formulation.) Observe that diffusivities are typically of the order of $10^{-9}\ \text{m}^2\text{s}^{-1}$, so relatively low flowrates can cause Péclet numbers to be extremely large.

3.3 Analysis and discussion

The dimensionless concentration distribution that satisfies the governing system is

$$\theta\left(\xi; I, \text{Pe}\right) = 1 - \frac{I}{\text{Pe}}\left\{1 + \left[\text{Pe} - \frac{\text{Pe}}{\tanh\left(\text{Pe}\right)}\right] e^{2\text{Pe}\xi}\right\}. \tag{3.19}$$

Péclet numbers and dimensionless currents can be positive or negative; note that the dimensionless concentration has the symmetry property

$$\theta\left(\xi; I, \text{Pe}\right) = \theta\left(1 - \xi; -I, -\text{Pe}\right), \tag{3.20}$$

in line with physical expectations. Figure 3-2 shows concentration distributions at several flowrates with fixed current $I = 1$, corresponding to the limiting current without net electrolyte flow ($v^{\blacksquare} = 0$ or $\text{Pe} = 0$). A positive Pe ($v^{\blacksquare} > 0$) delivers additional electrolyte to the anode, eliminating mass-transport limitations and making the electrolyte concentration deviate from zero at $\xi = 0$. Negative Pe values are not depicted in Figure 3-2 because they increase mass-transport limitations, and are consequently impractical for applications. The observed responses to positive or negative Pe owe to the fact that

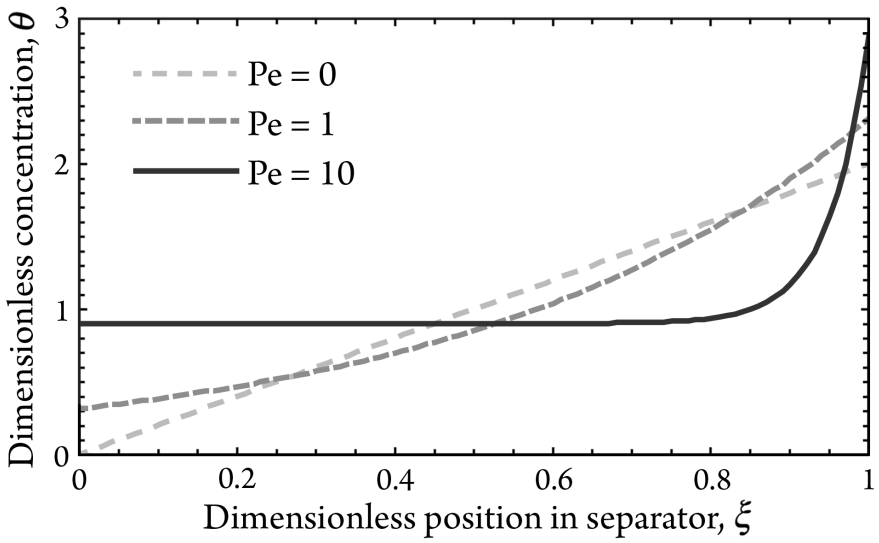

Figure 3-2 Co-current forced convection reduces mass-transport limitations in separators. Dimensionless concentration distribution as a function of positive Péclet number Pe > 0, at dimensionless current density $I = 0$ (the limiting current with no flow). Reproduced form reference 12.

anions react in an alkaline flow battery; if cations reacted — as they do in lithium-ion batteries — the impact of Pe on mass-transfer limitations would reverse, and countercurrent flow would reduce transport limitations.

The dimensionless limiting current I_L can be found through equation (3.19). If electric current is co-current with the volumetric flow ($I > 0$), then at I_L the electrolyte concentration in an alkaline convection battery separator vanishes at $\xi = 0$,

$$\frac{1}{I_L(\mathrm{Pe})} = 1 + \frac{1}{\mathrm{Pe}} - \frac{1}{\tanh(\mathrm{Pe})}. \tag{3.21}$$

Alternatively, if the two flows are countercurrent, then I_L is reached when the electrolyte concentration vanishes at the cathode, $\xi = 1$. Note that countercurrent scenarios can be described using equation (3.21) by applying the symmetry property explained after equation (3.19).

In Figure 3-3 dimensionless limiting currents I_L for current-coaxial flow are plotted against Pe; positive Pe values describe co-current flow, whereas negative values describe countercurrent flow. The corresponding volumetric flowrate Q and current density i are provided in real units on the opposing axes to give a more tangible physical sense of the dimensionless quantities. Several parameters describing the experimental setup of Suppes *et al*. [2,3] were used to redimensionalize I_L and Pe: geometric factors $L = 2$ cm and cross-sectional diameter 1.27 cm; the porosity of a random spherical packing $\epsilon = 0.432$ [17]; and the diffusivity and cation transference number of 2 M aqueous KOH, $D = 2.72 \times 10^{-9}$ m^2/s and $t_+^0 = 0.23$, respectively [1,18].

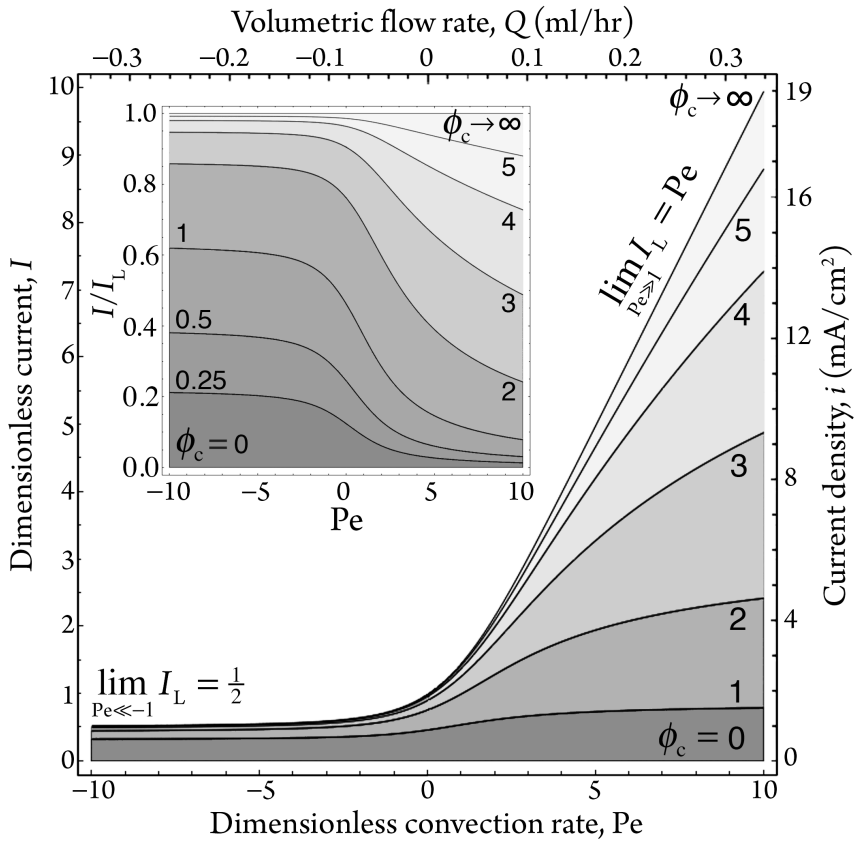

Figure 3-3 Limiting currents can be controlled by varying the rate of current-coaxial forced convection. Contour plot showing dimensionless concentration overpotential ϕ_c as a function of I and Pe. In the inset, I is scaled by the dimensionless limiting current I_L. At constant current, concentration overpotential decreases as Pe increases. Reproduced form reference 12.

Figure 3-3 shows that I_L converges rapidly to asymptotic limits

$$\lim_{\mathrm{Pe}\gg 1} I_L = \mathrm{Pe} \quad \text{and} \quad \lim_{\mathrm{Pe}\ll -1} I_L = \frac{1}{2}. \tag{3.22}$$

Low electrolyte diffusivity amplifies the effect of forced convection: I_L rises by an order of magnitude with a volumetric flowrate as low as 0.3 mL/hr. Although this effect is amplified artificially because of the very large separator thickness used by Suppes *et al.* ($L = 2$ cm), it is nevertheless clear that very slow flows can increase limiting currents dramatically. Flowrates of a few milliliters per minute should achieve the same effect in separators with more practical thicknesses. In any case, the convection-battery configuration may make possible significant reductions in charge or discharge times.

Through equation (3.19) the reduction in voltage loss arising from electrolyte flow can also be calculated. Under the assumption that the electrolyte is ideal, the MacInnes equation (modified form of Ohm's law) governing the distribution of potential Φ in the separator is given by equation (1.16). Integration of the second term in the MacInnes equation (1.16) across the separator thickness and insertion of the dimensionless parameters from equations (3.17) yields the net concentration overpotential Φ_c. A dimensionless concentration overpotential ϕ_c can then be identified as

$$\phi_c = \frac{-F z_+ z_- \Phi_c}{RT\left(z_- t_+^0 + z_+ t_-^0\right)} = \ln\left[\frac{\left(1 - \frac{I}{\mathrm{Pe}}\right)\sinh\left(\mathrm{Pe}\right) + I e^{\mathrm{Pe}}}{\left(1 - \frac{I}{\mathrm{Pe}}\right)\sinh\left(\mathrm{Pe}\right) + I e^{-\mathrm{Pe}}}\right]. \tag{3.23}$$

Figure 3-3 also provides contours that show how ϕ_c depends on I and Pe. As the limiting-current line in Figure 3-3 is approached, the concentration overpotential diverges. Although earlier analyses have argued that concentration gradients vanish in the

separators of convection batteries [3], causing minimal overpotential, equation (3.19) contrarily shows that ϕ_c depends strongly on Pe.

Equation (3.23) rationalizes the overpotential decrease observed by Suppes *et al*. after co-current current-coaxial flow was applied to an initially stagnant alkaline convection battery [2]. In the limits of large and small Péclet number,

$$\lim_{\mathrm{Pe}\to 0} \phi_c = \ln\frac{1+I}{1-I} \quad \text{and} \quad \lim_{\mathrm{Pe}\gg I,1} \phi_c = \ln\left(1+2I\right). \tag{3.24}$$

The difference between these two formulas can be used to compute the steady-state concentration-overpotential reduction $\Delta\phi_c$ for alkaline convection-battery separators with large-Péclet-number, co-current, current-coaxial flow,

$$\Delta\phi_c = \lim_{\mathrm{Pe}\gg I,1} \phi_c - \lim_{\mathrm{Pe}\to 0} \phi_c = \ln\left[\frac{\left(1-I\right)\left(1+2I\right)}{1+I}\right]. \tag{3.25}$$

This final result allows direct computation of the voltage changes observed experimentally in alkaline convection batteries. Since the previously investigated alkaline convection battery was observed at room temperature using a 2 M KOH electrolyte,

$$\Delta\Phi_c = \Delta\phi_c \cdot 14 \text{ mV}. \tag{3.26}$$

In the experiments of Suppes *et al*. [2,3], the load was fixed at $R = 550\ \Omega$. At potential $V = 1.2$ V, the total current can be found by applying Ohm's law to the load. Division by the cross-sectional area of the separator yields $i = 1.9\ \mathrm{mA/cm^2}$, corresponding to $I = 0.92$. Using equation (3.25), $\Delta\phi_c = -2.1$. Conversion back to a dimensional potential shows that $\Delta\Phi_c = -30$ mV.

Although the present calculation is based on very rough approximations, it obtains a result consistent with experimental observation: $-\Delta\Phi_c$ in the range of 10-50 mV. Error could arise from the assumptions made regarding separator porosity and tortuosity. Although a pseudo-steady-state assumption is probably reasonable when Péclet numbers are large, transients may be significant when flow is very slow. Additional overpotential increases could also occur due to concentration accumulation or depletion in the electrodes, an effect that is amplified when flow is stopped.

3.4 Optimal flowrate

From an engineering point of view, flowrate control might be an important factor in using a convection battery, because varying pumping loads could change the battery's operating cost. Two conflicting factors determine the power efficiency of a convection battery. The electrical power efficiency rises with flowrate, since concentration overpotentials are decreased by electrolyte flow; but mechanical power efficiency falls with flowrate, owing to the parasitic power demands of pumping systems. Therefore, it is worthwhile to seek an optimal flowrate to optimize the net power efficiency of a convection-battery system.

3.4.1 Power gain by overpotential decrease

As shown in chapter 3.3, forced convection of electrolyte through a traditional battery cell can increase its output voltage by decreasing the concentration overpotential.

Concentration overpotential is associated with an ohmic power loss through equation (1.16),

$$P_c = iA\Phi_c = -\frac{iART\left(z_- t_+^0 + z_+ t_-^0\right)}{Fz_+ z_-}\ln\left[\frac{\left(1-\frac{I}{\mathrm{Pe}}\right)\sinh(\mathrm{Pe}) + Ie^{-\mathrm{Pe}}}{\left(1-\frac{I}{\mathrm{Pe}}\right)\sinh(\mathrm{Pe}) + Ie^{\mathrm{Pe}}}\right]; \tag{3.27}$$

the power savings due to application of electrolyte flow, ΔP_c, is then given through equation (1.16) by

$$\Delta P_c = -iA\left(\Phi_c - \lim_{\mathrm{Pe}\to 0}\Phi_c\right) = -\frac{iART\left(z_- t_+^0 + z_+ t_-^0\right)}{Fz_+ z_-}\ln\left[\frac{\left(1-\frac{I}{\mathrm{Pe}}\right)\sinh(\mathrm{Pe}) + Ie^{-\mathrm{Pe}}}{\left(1-\frac{I}{\mathrm{Pe}}\right)\sinh(\mathrm{Pe}) + Ie^{\mathrm{Pe}}}\cdot\frac{1+I}{1-I}\right]. \tag{3.28}$$

This power savings is reflected by a reduction in the energy that the battery releases as heat, and a corresponding increase in useful work that the battery can do.

3.4.2 Power loss by friction

The convection-battery configuration does have a potential disadvantage: pump operation can be energetically costly. As fluid flowrate increases, there is an increase in heat dissipation due to the frictional losses associated with fluid motion through the porous electrodes and separator. The amount of energy dissipated in the separator of a cylindrical packed-bed convection battery can be estimated using the Ergun equation [19], which correlates the hydraulic pressure drop Δp to the volumetric flowrate (Péclet number). The product of the pressure drop and flowrate then yields the rate of energy dissipation by fluid friction,

$$\Delta P_{\mathrm{f}} = \frac{50\left(1-\varepsilon\right)^{2} a_{\mathrm{V}}^{2} \mu D^{2} A}{3L}\mathrm{Pe}^{2} + \frac{7\varepsilon^{1.5}\left(1-\varepsilon\right) a_{\mathrm{V}} \rho D^{3} A}{3L^{2}}\mathrm{Pe}^{3}. \tag{3.29}$$

Here μ and ρ are the dynamic viscosity and density of the liquid; a_V is the surface-to-volume ratio of the particles that comprise the packing. (Although it is not usually involved in the Ergun equation, the diffusivity D appears in equation (3.29) because the Péclet number was used as a representative volumetric flowrate.) Equation (3.29) shows that frictional losses increase with the rate of liquid flow. At low flowrates, the dissipation increases with Pe^2; at high flowrates, a Pe^3 dependence dominates. As one would expect, there is no frictional dissipation when $\mathrm{Pe} = 0$.

3.4.3 Optimal flowrate

Summation of the power gained from decreasing concentration overpotentials and power lost to friction in pumping yields total power loss ΔP_{loss}

$$\Delta P_{\mathrm{loss}} = \Delta P_{\mathrm{c}} + \Delta P_{\mathrm{f}}. \tag{3.30}$$

Figure 3-4 shows the net power loss as a function of the flowrate at a fixed dimensionless current density, $I = 500$. When the Péclet number is small (low flowrate), the concentration overpotential dominates the power loss; as the flowrate increases losses due to fluid friction begin to dominate. Interestingly, an optimal flowrate is present between these two extremes, showing that there is an optimal fluid flowrate that

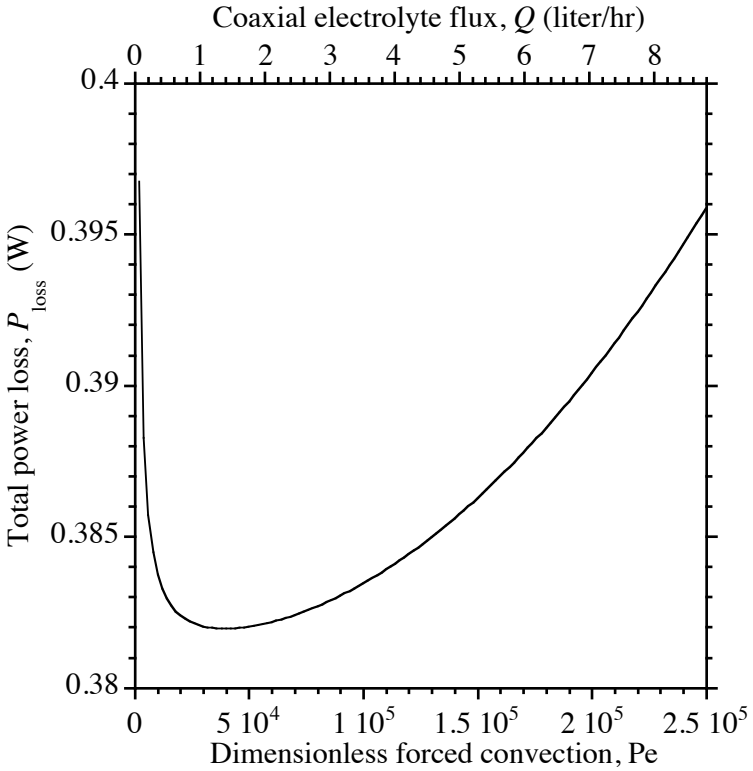

Figure 3-4 The total power losses P_{loss} is demonstrated as a function of the dimensionless forced convection rate, Pe at $I = 500$. The power losses are from the friction in the porous medium and the concentration overpotential of the nonuniform ion distribution. The concentration overpotential effect is dominant when the flow is slow; however, the friction loss is dominant factor in the fast flow.

minimizes the net power loss due to concentration overpotential in the separator and pumping fluid through it. Since the power gain from decreased overpotential also depends on the current density, the optimal dimensionless flowrate will also vary with the dimensionless applied current, as shown in Figure 3-5.

3.5 Conclusions

Preliminary analysis of an alkaline convection-battery separator suggests that current-coaxial forced convection may provide significant benefits when applied to traditional battery cells. Convection reduces mass-transfer limitations; the corresponding reduction in concentration overpotential at steady state can be estimated readily with equation (3.25). Most importantly, equation (3.21) was developed to show that forced electrolyte convection affects limiting currents dramatically. Thus, if rate limitations associated with the cell reactions or electrode materials are minimal, the charge/discharge times of rechargeable convection batteries can in principle be made arbitrarily short by imposing relatively slow electrolyte flows.

To evaluate the benefits of the convection-battery configuration fully, parasitic losses owing to the power demands of pumping systems were considered as well. When weighing the benefits of the convection-battery configuration it is clearly necessary to include the cost associated with driving fluid flow through the battery, *i.e.*, the power demand associated with pumping. It appears that there is a domain of Péclet number where the benefits of concentration-overpotential reduction outweigh the pumping cost.

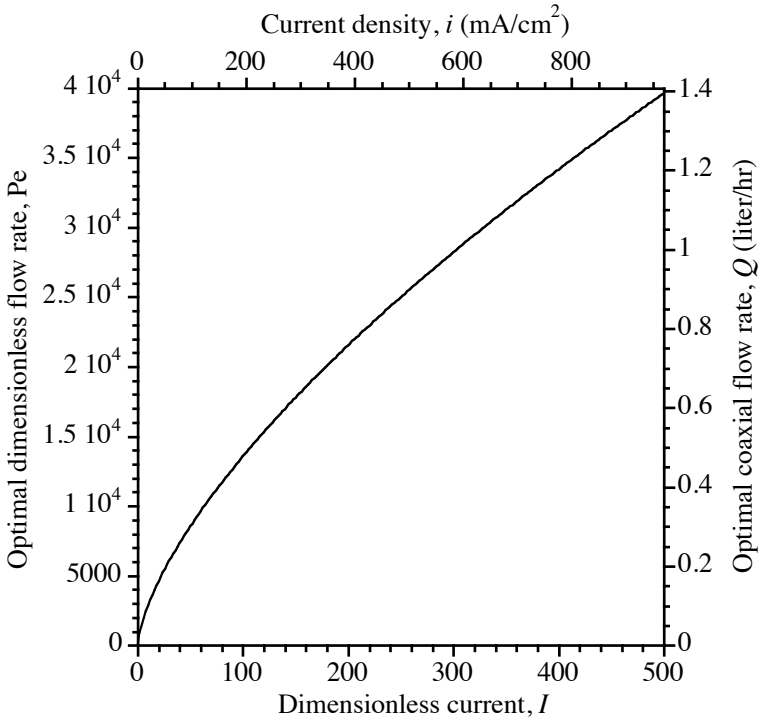

Figure 3-5 The optimal dimensionless flowrate, Pe, for the best power efficiency is presented as a function of the dimensionless current, I.

Furthermore, pumping costs are reasonably low, considering the dramatic affect of Péclet number on the maximum charge/discharge rate. In the future, for a complete assessment of the convection-battery configuration, the model should be extended to account for interfacial kinetic limitations and composition variation within the electrodes, which were neglected here.

3.6 References

[1] Newman JS, Thomas-Alyea KE. Electrochemical systems. 3rd ed. New Jersey: Wiley-IEEE; 2004.
[2] Suppes GJ, Sawyer BD, Gordon MJ. High-energy density flow battery validation. AIChE J 2011;57(7):1961–7.
[3] Sawyer B, Suppes G, Gordon M, Heidlage M. Impact of electrode separator on performance of a zinc/alkaline/manganese dioxide packed-bed electrode flow battery. J Appl Electrochem 2011;41(5):543–50.
[4] Alkire R, Gracon B. Flow-through porous electrodes. J Electrochem Soc 1975;122(12):1594–601.
[5] Bek R, Zamyatin A. Mass transfer coefficient and area accessible to electrolysis in flow-through graphitic-carbon-fiber electrodes. Sov Electrochem 1978;14(8):1034–9.
[6] Kinoshita K, Leach SC. Mass-transfer study of carbon felt, flow-through electrode. J Electrochem Soc 1982;129(9):1993–7.
[7] Schmal D, Erkel J, Duin PJ. Mass transfer at carbon fibre electrodes. J Appl Electrochem 1986;16(3):422–30.
[8] Delanghe B, Tellier S, Astruc M. Mass transfer to a carbon or graphite felt electrode. Electrochim Acta 1990;35(9):1369–76.
[9] Zhou H, Zhang H, Zhao P, Yi B. A comparative study of carbon felt and activated carbon based electrodes for sodium polysulfide/bromine redox flow battery. Electrochim Acta 2006;51(28):6304–12.
[10] Trainham JA, Newman J. A comparison between flow-through and flow-by porous electrodes for redox energy storage. Electrochim Acta 1981;26(4):455–69.
[11] Linden D, Reddy TB, Handbook of batteries. New York: Mc-Graw Hill; 2002.
[12] S. U. Kim and C. W. Monroe, “Increasing the rate capability of batteries with electrolyte flow,” Applied Energy, vol. 103, pp. 207–211, Mar. 2013.
[13] Bockris JO, Reddy AK, Gamboa-Aldeco ME. Modern electrochemistry 2A: fundamentals of electrodics. 2nd ed. Springer; 2001.
[14] Newman J, Chapman TW. Restricted diffusion in binary solutions. AIChE J 1973;19(2):343–8.
[15] Dunning JS. Analysis of porous electrodes with sparingly soluble reactants.

Ph.D. thesis. University of California, Los Angeles; 1971.
[16] Bruggeman DAG. Calculation of various physics constants in heterogenous substances i. Dielectricity constants and conductivity of mixed bodies from isotropic substances. Annalen Der Physik 1935;24(7):636–64.
[17] Ouchiyama N, Tanaka T. Porosity estimation for random packings of spherical particles. Indust Eng Chem Fund 1984;23(4):490–3.
[18] Newman J, Bennion D, Tobias CW. Mass transfer in concentrated binary electrolytes. Ber Bunsenges Phys Chem 1965;69:608–12.
[19] S. Ergun, Chem. Eng. Prog. 48, 89 (1952).

Chapter 4 Thermoelectrical modeling of large-format prismatic lithium-ion cells

Owing to their large energy densities and low packaging cost, large-format prismatic lithium-ion cells are becoming ubiquitous. Thermal management is crucial for large batteries due to their small surface-to-volume ratios, which can lead to local degradation of active materials within the battery, or catastrophic thermal runaway of the battery as a whole [1]. In this chapter, we extend Newman-Tobias porous-electrode theory [2] by coupling its local charge balances to a local energy balance. The model is shown to predict the transient thermal response of a prismatic lithium-ion battery pouch cell well. The approach taken here simplifies the standard Dualfoil model [3-5] by neglecting mass transport phenomena in the battery interior. Despite this simplification, the model predicts the thermal response of 15-Ah A123 prismatic pouch cells within experimental error.

4.1 Motivation

Early in 2013, two cases of aircraft cabin fires originating from high-capacity lithium-ion batteries made world headlines [6-9]. A postmortem analysis by the National Transport Safety Board reported several signs of internal short-circuits and thermal runaway within the airplane batteries [10]. Figure 4-1(a) compares exemplar and damaged lithium-ion battery packs from GS-Yuasa Inc. Figure 4-1(b) and (c) illustrate

(a)

(b) (c)

Figure 4-1 Boeing event lithium-ion battery (a) exemplar and burned JAL event battery, (b) exemplar and damaged cell CT scan image, and (c) damaged electrode; yellow circle indicates a hole at the center of the electrode. Reproduced from reference 10.

the signs of thermal runaway and internal shorts within failed batteries. The electrolytic solutions in the battery cells comprise mixed carbonate solvents, with boiling points between 91 °C (for dimethyl carbonate, DMC) and 248 °C (for ethylene carbonate, EMC). These are low enough that resistive heating or exothermic chemical reactions causes outgassing, explaining why the jellyrolls are warped and the tabs are dislocated in the CT scan of the damaged cell from Figure 4-1(b). Although the GS-Yuasa case is still under investigation, these figures are enough to suggest that more accurate thermal management systems are needed, which leads naturally to the development of faster, more accurate electrothermal battery models.

Several researchers have also observed that in large-format cells of various types, spatial non-uniformity of temperature within the cell volume can significantly impact battery performance [11-15]. An example of thermal inhomogeneity is shown in Figure 4-2; one can see that the domain near the tab at the upper left is significantly warmer than its surroundings after a long period of cell operation. Such 'hot spots' are typical in large-format cells; understanding where and how they occur is critical for evaluating the safety of a given battery configuration.

Even if they do not cause catastrophic failure of the battery cell, inhomogeneities in the thermal history of battery materials may affect cycle life. Battery degradation with respect to time and cycling is presently very poorly understood, and is typically modeled almost wholly empirically, partially because of a lack of mechanistic understanding [16,17]. Since temperature tends to affect phenomena like mechanical fatigue, side reactions, and other factors associated with aging, it worthwhile to develop more detailed, microscopically informed thermal models.

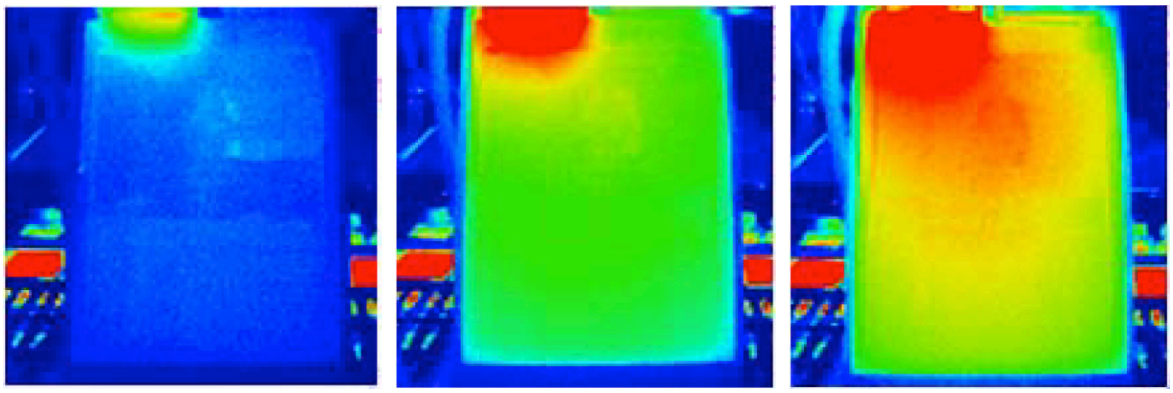

(a) (b) (c)

Figure 4-2 Three infrared images of 14.6 Ah lithium-ion battery cell from LG Chem Inc. The images are taken at (a) 2 minutes, (b) 10 minutes, and (c) 18 minutes, respectively. These show how temperature profile develops. The battery was discharged at a constant 3C rate [15]. Reproduced from reference 15.

Present day battery-cell designs are not optimized to minimize temperature inhomogeneity, and therefore may not achieve the highest possible safety and health targets. In order to understand how to optimize cells, one needs models with predictive capability. This requires developing an understanding of the fundamental transport and kinetic properties of battery materials within a specific battery chemistry. By fitting our coupled electrothermal model to experimental data gathered from an existing battery cell, we obtained reliable measurements of such properties. With those quantities in hand, it should be possible to model alternative battery-cell geometries reliably in the future.

In this chapter, I first describe some experiments that motivate the theoretical study, which were developed for model testing and performed by Jason Siegel (Anna Stefanopoulou group, UM Mechanical Engineering) and Lynn Secondo (Monroe group). I then develop an extended Newman-Tobias electrothermal model, provide a dimensional analysis of it, evaluate parameter sensitivity, and demonstrate a procedure by which the experimental data was used to establish the thermoelectrical properties of the materials in an A123 15Ah Li-$FePO_4$ (LFP) battery pouch-cell. For solving the inverse problem of property estimation with the model, data were gathered using a periodic galavanostatic charge/discharge scheme (an 'excitation test') that allowed the battery to be run at a constant current magnitude without large fluctuations in its overall state of charge (SOC). Despite its apparent lack of complexity (relative to the Dualfoil package), our four-parameter model, which neglects all mass-transfer effects, matches experimental data within error. For the A123 battery, the model fit yields a set of material-property values that are consistent with measurements from the literature.

4.2 Experiments

4.2.1 Experimental setup

Surface-temperature profiles were measured in a Z-Plus thermal chamber (Cincinnati Sub-Zero Inc., USA), with ambient temperature held fixed at 25°C by forced convection. Sixteen T-type thermocouples from OMEGA Engineering Inc., USA, with resolution of 0.5°C, were placed on the surface of the battery to track its temperature during operation. Tests were performed on 15-Ah LFP pouch cells from A123 Inc., to which thermocouples were attached with adhesive tape, as shown in Figure 4-3(a). The exact placement of the 16 thermocouples on the pouch-cell surface is illustrated schematically in Figure 4-3(b). The irregular thermocouple spacing was chosen based on literature observations of temperature distributions in other large-format batteries (*cf.* Figure 4-2) [15], which suggested greater heating (and greater thermal gradients) near the tabs. Higher spatial density of temperature measurements near the tabs also helped to achieve higher precision when locating the maximum temperature.

4.2.2 Battery preconditioning

Batteries were cycled in the thermal chamber using a Bitrode battery tester (Bitrode Inc., USA). Before each experimental thermal test, the battery was electrically preconditioned at the desired ambient temperature (25 °C in these tests) by first charging at a 1C rate up to the open-circuit voltage corresponding to 100% SOC (3.6V for the A123 15Ah LFP cells used here). Practically, charging at this rate corresponds to a nontrivial amount of overpotential. To ensure that the desired equilibrium SOC was

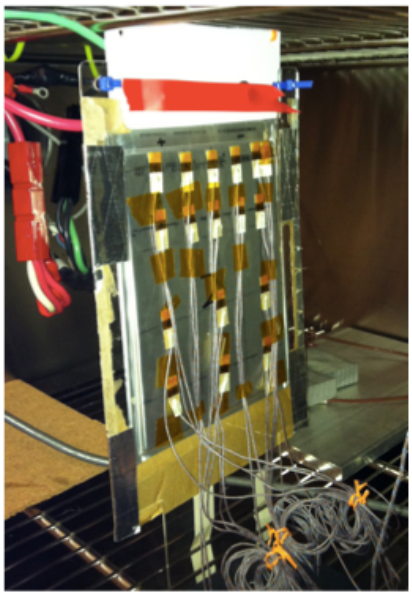

(a)

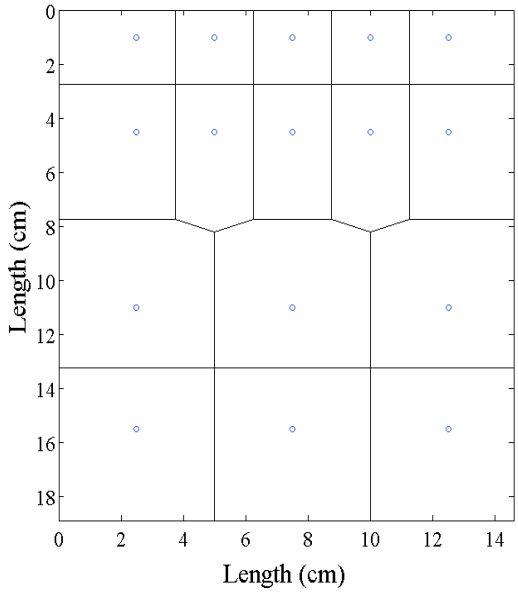

(b)

Figure 4-3 (a) Experimental setup of the 15-Ah A123 LFP pouch cell (190 mm x 146 mm x 6.5 mm) in the thermal chamber, with thermocouple array attached. (b) Schematic diagram showing the thermocouple locations schematically, on a Voronoi diagram used to establish area elements for spatial temperature averaging.

reached, the cell voltage was subsequently held constant while the current was allowed to relax until it reached C/100 (a cutoff rate of 0.15 A for A123 15Ah LFP). Typical current and potential data from pre-test battery conditioning are shown in Figure 4-4. After preconditioning, the desired initial SOC for testing was attained by coulomb counting during a discharge, using the reported 15Ah capacity as the assumed capacity. All tests reported here initiated at a 50% SOC, achieved via discharging from the highest charge condition at 1C for 30 minutes. After this discharging, the cell was then held at open circuit (0C) until each of the thermocouples on the cell surface reached ambient temperature, typically requiring a rest time of one hour. Thermal relaxation appears to be the rate-limiting process: during the thermal relaxation steps, no significant voltage changes were observed.

4.2.3 Excitation test control scheme

Most of the material properties of the battery are known to depend on SOC [18-23]. Therefore, a control scheme involving short-duration charges and discharges with fixed periodicity was introduced to allow the study of rate and temperature effects without inducing significant changes in the volume-averaged thermodynamic state. Square-wave excitation tests with variable wave period p and amplitude A were performed around an average SOC value of 50% (see Figure 4-5 for an illustration of the input signal). Around 50% SOC, the open-circuit potential of the battery exhibits a plateau with respect to charge state, further ensuring that the properties are relatively constant. Below, transient temperature-distribution data are reported during excitation tests with period p = 100s and amplitudes of A = 5C and A = 1C.

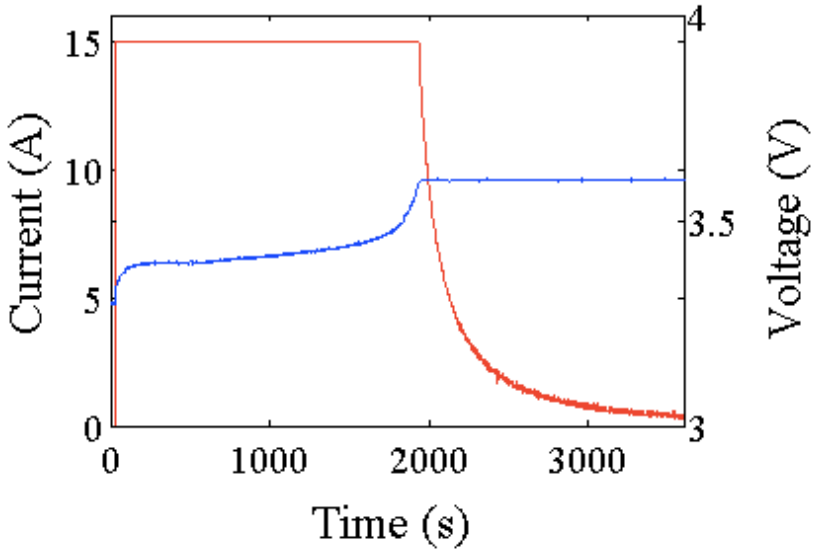

Figure 4-4 Current/voltage data during preconditioning of an A123 15 A-h LFP cell at an ambient temperature of 25 °C.

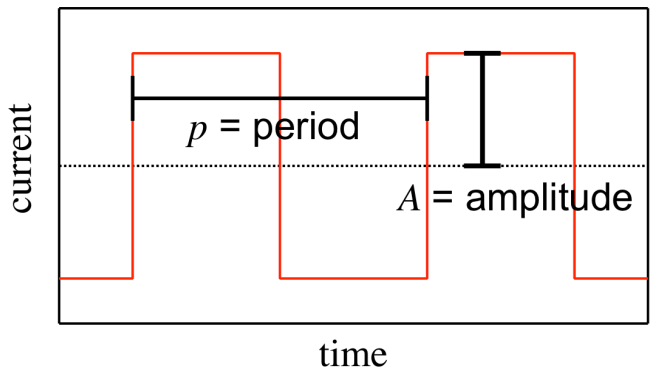

Figure 4-5 Control scheme for excitation tests. The scheme repeats charge and discharge periodically, maintaining a relatively constant SOC during testing.

4.2.4 Experimental results

Figure 4-6 presents experimental results from two different excitation tests of the A123 prismatic cell. The reported average temperature represents a "surface average". To compute surface averages, the area sampled by each thermocouple was taken from a Voronoi tessellation, as in Figure 4-3(b). The Voronoi tessalation divides a surface containing a finite number of nodes into cells, each of which contains all points whose distances from the node are less than or equal to their distances from any other node. The sizes of the Voronoi cells relative to the total battery-surface area were used as weighting factors when computing the spatially averaged temperature. (This mimics discretely the process of integrating distributions over surfaces to compute their geometric averages, used by the COMSOL simulation package.)

Figure 4-6(a) shows that the surface temperature of the battery is highly non-uniform during excitation tests, even though the average SOC is relatively constant. Thus additional factors than thermodynamic state take part in the thermal response. One would expect some extent of Joule heating (heat generated by current flow through electrical resistance) during the excitation, which, being always exothermic, should cause the surface temperature to rise. More intriguing are the oscillations in temperature in the steady periodic state, shown most clearly in Figure 4-6(b), and also possibly observable through the noise in Figure 4-6(c). These oscillations are surprising since the rate of Joule heating should be relatively constant throughout the test, since power $\sim I^2R$ and I always has the same magnitude. Thermal oscillations at a fixed current magnitude (temperature falling relative to the average during charge steps and rising during discharges) suggest there is reversible heat generation or consumption with the passage of current.

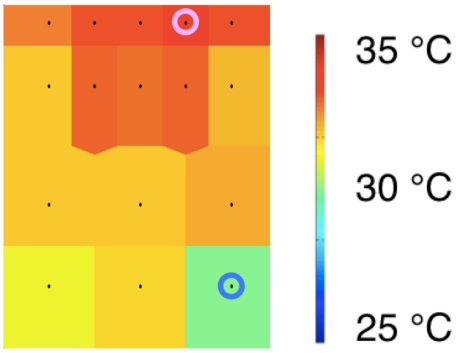

(a)

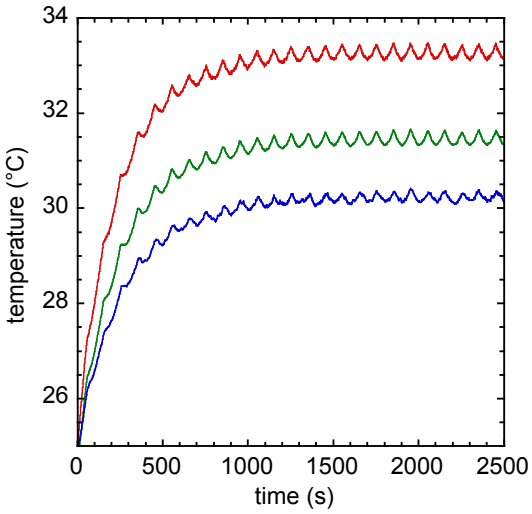

(b)

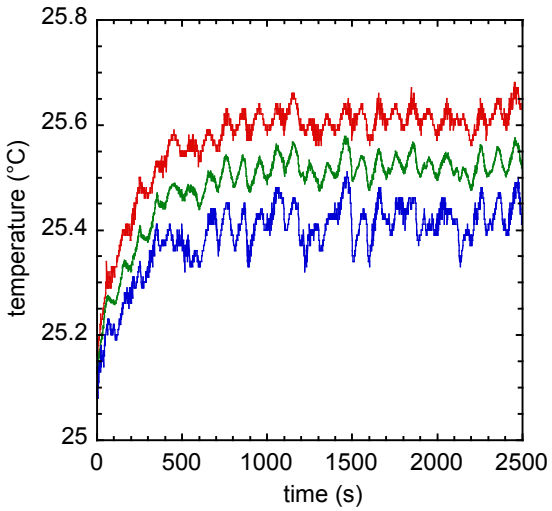

(c)

Figure 4-6 Experimental results. (a) Surface temperature profile for an excitation test with A = 5C, p = 100s after 1 hour. The thermocouple locations exhibiting the maximum and minimum temperatures are circled. (b) Transient maximum (red), minimum (blue), and surface-averaged (green) thermocouple readings during an excitation test with A = 5C, p = 100s; (c) excitation test with A = 1C, p = 100s.

Such behavior is typically associated with the reversible heat – that is, the entropy – of the cell reaction, which can act as a heat source or heat sink, depending on the sign of the current. Reaction entropy has been quantified for a number of battery systems and electrode materials [1,19,21-23].

4.3 Modeling

4.3.1 Previous thermoelectrochemical modeling

Two fundamental phenomena are combined in electrothermal modeling: charge transport and heat transport. The approach to modeling heat transfer is common across groups, but there are two distinct philosophies of charge-transport modeling: equivalent-circuit modeling [24-28] and electrochemical mass-transport modeling [2-5,29-32]. Both methods describe the electrical response of lithium-ion battery cells quite accurately, but their levels of sophistication regarding the cell electrochemistry differ significantly.

For fast calculation, equivalent-circuit models (ECMs) have been widely used to provide phenomenological relationships between current/voltage input and voltage/current output of battery constituents, cells, or systems [24-28]. An ECM treats the battery cell as a network of resistors and capacitors, which in principle model the electrical response to microscopic phenomena such as internal mass diffusion (in solid and liquid phases), migration, charge transfer, and interfacial capacitance. Open-circuit voltage and arbitrary voltage sources are sometimes included to account for the observed dependence of the system response on instantaneous SOC, applied current, and temperature. ECMs are computationally efficient, motivating their use for real-time

control systems, such as SOC and state-of-health (SOH) estimators or power-management systems for HEVs [27].

For thermoelectrochemical modeling, Fleckenstein *et al*. have modeled a battery cell as an aggregate of volume elements through which charge transport is governed by ECMs, which are coupled to a general thermal energy balance that accounts for heat accumulation, conduction, and local heat generation in each volume element [33]. The charge balance communicates irreversible Joule heating and reversible reaction heat into the local thermal-energy balance. Also, the thermal model in principle communicates back to the ECMs, through functions that establish the temperature dependences of resistances and capacitances. (Temperature dependences of ECM parameters were not included in Fleckenstein *et al*.'s analysis.)

Fleckenstein *et al*.'s model was found to match experimental temperature distribution data effectively for a 32113-type 4.4-Ah LFP battery (company, country), but discharge data from a very narrow range of applied currents was used for model validation. It is possible that outside the 6.8C-9.2C rate range used by the authors the ECM employed breaks down, preventing accurate data fitting.

Electrochemical mass-transport models [2-5,29-32] have also been used to underpin thermoelectrochemical simulations. The standard Dualfoil scheme is the most common mechanistically based electrochemical model [3-5]. Fuller *et al*. developed a lithium-ion battery-cell model based on porous electrode theory, concentrated-solution theory (describing mass transport and ionic conduction in liquid-electrolyte phases), Ohm's law (describing charge transport in solid phases), and intercalation kinetics (at

solid/electrolyte interfaces). Dualfoil augments the Newman-Tobias porous-electrode model by accounting for concentration polarization in the separator, pore-filling electrolyte, and solid intercalation media.

Bernardi *et al*. accounted for energy generation within a battery, under the assumption that, owing to the relatively small thickness of individual cells (typically much less than 1/2 mm), their temperatures are locally uniform [34]. Srinivasan and Wang [29] provided the most complete coupling of Dualfoil to a local heat balance. In a 2D geometry, they solved the electrochemical and thermal model equations simultaneously by discretizing the partial differential equations involved and using an implicit linear multistep solution method. Recently, Christensen *et al*. suggested a new approach for 3-D thermoelectrochemical modeling [30-32], which will be applied to large-capacity Li-ion NMC cells in chapter 5.

4.3.2 Newman-Tobias model (electrical porous-electrode theory)

The Newman-Tobias porous-electrode model [2] describes charge transport within porous electrodes, and suggests a few key dimensionless parameters that govern the charge distribution and reaction distribution within them. Newman and Tobias modeled porous electrodes with a 'macrohomogeneous approach' that expresses the microscopic geometry of porous materials in terms of a local porosity and a local surface-to-volume ratio. Each simulation volume element comprises conductive solid (phase 1) and conductive liquid (phase 2), which both conduct charge and can exchange it through local interfacial charge transfer. Newman and Tobias's original paper provides analysis of the

current, potential, and reaction distributions in planar porous electrodes with both linear and Tafel interfacial kinetics, assuming that the electrode in question is isothermal [2]. They introduce a few dimensionless parameters that control the distribution of current, and study their effect on reaction distributions in detail.

Porous electrodes have been widely used because interfacial charge-transfer rates generally scale with surface area, and porous electrodes tend to afford very high surface-to-volume ratios a_V. Figure 4-7 schematizes the charge transport and exchange processes that occur in a planar porous electrode as it experiences an applied current. In the model, the detailed microscopic geometry shown in Figure 4-7(a) is neglected, excepting for its description in terms of a_V and the electrode porosity ϵ; the solid and liquid are treated as "volume-averaged" phases, which in each differential control volume support parallel charge conduction (through their bulk) and exchange (across their interface within the element), as depicted in Figure 4-7(b). (The figure also establishes sign conventions for current and interfacial charge exchange; the overall current density i is positive when cathodic; positive current associated with charge exchange, i_n, flows into the electrolyte from the solid.)

The fundamental model comprises dynamic charge balances on the solid and liquid phases, designated with subscripts 1 and 2, respectively:

$$\nabla \cdot \vec{i}_1 = a_V i_n, \tag{4.1}$$

$$\nabla \cdot \vec{i}_2 = -a_V i_n. \tag{4.2}$$

(a)

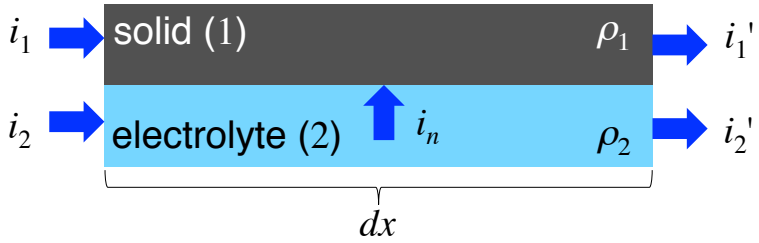

(b)

Figure 4-7 A schematic diagram showing (a) a charging anode in 1-D and (b) magnified one part.

Note that in combination with Gauss's law and the local electroneutrality condition, overall charge conservation within each volume element implies that the sum of both currents is solenoidal, $\nabla \cdot \left(i_1 + i_2 \right) = 0$.

The generation terms in equations (4.1) and (4.2) describe the kinetic current, which relates to the flux of charge across the liquid/solid interface due to electrochemical reactions. For an elementary electrochemical reaction, charge-transfer kinetics is described by the Butler-Volmer equation

$$i_n = i_0 \left\{ \exp\left(-\frac{\beta n F}{RT} \eta_s \right) - \exp\left[\frac{(1-\beta) n F}{RT} \eta_s \right] \right\}, \tag{4.3}$$

in which β is a symmetry factor, i_0 is the exchange-current density (a kinetic rate constant), and η_s is the surface overpotential. Surface overpotential relates to the local voltages of the solid and liquid, and the open-circuit potential U, through

$$\eta_s = \Phi_1 - \Phi_2 - U. \tag{4.4}$$

The open-circuit potential is a thermodynamic property, measured at equilibrium (in an isothermal electrochemical system, 'equilibrium' corresponds to a situation where there is no current and the cell voltage is constant). Generally U may depend on the local state of charge (SOC) of the electrode, and is described for many materials by a Nernst equation [35]. If solid-phase diffusion is rate-limiting, U may also include a concentration overpotential arising from concentration polarization within the solid intercalation compounds in the electrodes. This feature is neglected here, but is included in the Dualfoil model in the next chapter.

To close the problem, flux laws are needed to relate the local current densities in the liquid and solid to their local potentials. Newman and Tobias used versions of Ohm's law in each phase,

$$\nabla\Phi_1 = -\rho_1\vec{i}_1, \tag{4.5}$$

$$\nabla\Phi_2 = -\rho_2\vec{i}_2, \tag{4.6}$$

where ρ_i is the bulk resistivity of phase i. (Note that Ohm's law as it stands is naturally a good model for charge transport in solids; for ion transport in liquids, Ohm's law can be derived from MacInnes equation (1.16) under the assumption that concentration gradients in the liquid electrolytic solution are negligible; note that $\rho_2 = 1/\kappa_2$, where the ionic conductivity is given by equation (1.17).) Equations (4.1)-(4.6) comprise the most general form of the Newman-Tobias model, providing the governing system of interior equations used in the three-dimensional simulations described later in this chapter.

In their seminal paper [2], Newman and Tobias analyzed equations (4.1)-(4.6) for a one-dimensional electrode geometry (an electrode of thickness δ in the x direction) under two extremes of the reaction kinetics. When interfacial kinetics is fast, i_0 tends to be large in comparison to in; consequently overpotential is small, and

$$i_n \approx i_0\left\{1-\frac{\beta nF}{RT}\eta_s+\ldots-1-\frac{(1-\beta)nF}{RT}\eta_s-\ldots\right\}=-\frac{i_0 nF}{RT}\eta_s. \tag{4.7}$$

Consequently, fast reaction rates correspond to a 'linear kinetic regime'. Similarly, when interfacial kinetics is slow, overpotential is large, and the kinetic expression simplifies asymptotically to an exponential relationship between transfer current and overpotential –

the so-called Tafel regime. In this discussion (and since interfacial kinetics in Li-ion batteries tends to be fast) linear kinetics will be assumed for simplicity.

In the linear kinetic regime, the transfer current can be expressed simply as

$$\rho_{\mathrm{k}} i_n = a_V \left(\Phi_1 - \Phi_2 - U\right), \tag{4.8}$$

in which the kinetic resistivity ρ_{k} depends on temperature, the surface-to-volume ratio of the solid phase, and the interfacial exchange-current density through

$$\frac{1}{\rho_{\mathrm{k}}} = \frac{i_0 nF}{a_V RT}. \tag{4.9}$$

Newman and Tobias obtain an analytical solution to the one-dimensional problem by first inserting equation (4.10) into the charge balance on the solid (equation (4.1)), taking the gradient of both sides, then inserting the expressions of Ohm's law from equations (4.5) and (4.6), yielding the master equation

$$\nabla\left(\nabla \cdot \vec{i}_1\right) = \frac{1}{\rho_{\mathrm{k}}}\left(\rho_1 \vec{i}_1 - \rho_2 \vec{i}_2\right). \tag{4.10}$$

Note that U does not appear here, although in lithium-ion batteries, it is generally a function of the extent of intercalation that has occurred in a solid electrode material. Following Newman and Tobias, we take the open-circuit potential to be constant, under the assumption that changes in the local charge state are minimal in the experiments being modeled. (Although any constant would suffice, we set $U = 0$ for the remainder of this analysis for simplicity.)

In a 1-D geometry (as in Figure 4-7), the solenoidal character of the total current density allows equation (4.10) to be solved analytically. The total current satisfies

$$i = i_1(x) + i_2(x). \tag{4.11}$$

That is, although the local currents in the solid and liquid may change, the total current density in each volume element remains constant. In the situation shown in Figure 4-7, two boundary conditions arise naturally:

$$i_1(x = 0) = 0, \tag{4.12}$$

$$i_1(x = \delta) = i. \tag{4.13}$$

At $x = 0$, the interface with the separator, the conductive solid material has an insulating boundary; therefore the electric current is entirely ionic, passing only through the electrolyte. In comparison, at $x = \delta$, the liquid and solid meet at a solid, electronically conductive current collector; therefore, the current flows only through the solid phase.

4.3.3 General energy balance

Our work extends Newman-Tobias theory by incorporating a detailed local energy balance. The general form of this balance for a single, stationary, isobaric, multicomponent phase is given by Deen [36]:

$$C_p \frac{\partial T}{\partial t} = -\nabla \cdot \left(-k\nabla T + \sum_i \overline{H}_i \vec{J}_i + \vec{q}^{(x)} \right) + \sum_i \overline{H}_i \left(\nabla \cdot \vec{J}_i - R_i \right), \tag{4.14}$$

where C_p is the volumetric heat capacity, k the thermal conductivity, and $\vec{q}^{(x)}$ is the Dufour energy flux density (heat flux driven by concentration gradients); $\overline{H}_i$, $\vec{J}_i$, and R_i are the partial molar enthalpy, molar flux density relative to the mass-average velocity, and homogeneous generation rate of species i, respectively. (Note that the molar-flux densities in equation (4.14) relate to the local current density through Faraday's law, equation (1.8).)

The term on the left of equation (4.14) represents the local accumulation of enthalpy. The terms under the divergence on the right account for heat flux by conduction, net excess flux of latent heat, and the Dufour effect; the last term accounts for enthalpy generation, primarily by chemical reaction, but also by material accumulation (through the divergence of excess flux). Assuming that the Dufour flux can be neglected – shown by a variety of sources to be a good assumption in battery systems [21-23], equation (4.14) simplifies down to

$$C_p \frac{\partial T}{\partial t} = \nabla \cdot \left(k \nabla T\right) - \sum_i \vec{J}_i \cdot \nabla \overline{H}_i - \sum_i \overline{H}_i R_i . \tag{4.15}$$

The second term on the right of equation (4.15) accounts for Joule heating as follows. Current density relates to flux densities through Faraday's law equation (1.8), written in terms of molar fluxes as

$$\vec{i} = F \sum_i z_i \vec{J}_i , \tag{4.16}$$

using thermodynamics in terms of electrochemical potentials, it can be shown that the change in partial molar enthalpy of a charged species relates to the electric potential Φ through

$$\nabla \overline{H}_i = z_i F \nabla \Phi. \tag{4.17}$$

Together with Ohm's law, in the general form

$$\vec{i} = -\frac{1}{\rho} \nabla \Phi. \tag{4.18}$$

(where ρ represents the phase's effective resistivity) the right side of equation (4.15) can be rearranged to get a term that accounts for Joule heating by conduction through the bulk (simple I^2R heating)

$$C_p \frac{\partial T}{\partial t} = \nabla \cdot \left(k \nabla T \right) + \rho \left\| \vec{i} \right\|^2 - \sum_i \overline{H}_i R_i. \tag{4.19}$$

The last term in equation (4.19) accounts for local heat generation by reaction.

Assuming that equation (4.19) applies to a volume element of a porous electrode, and that the bulk generation of reaction enthalpy comes from interfacial charge-transfer reactions, equation (4.19) becomes

$$C_p \frac{\partial T}{\partial t} = \nabla \cdot \left(k \nabla T \right) + \rho \left\| \vec{i} \right\|^2 + \rho_{\mathrm{k}} i_n^2 - \frac{a_V T \Delta \overline{S}_{\mathrm{rxn}}}{nF} i_n. \tag{4.20}$$

(See the appendix to this chapter for the details of this connection), where $\Delta \overline{S}_{\mathrm{rxn}}$ is the local reaction entropy.

Use of equation (4.20) assumes that the solid and liquid within a given porous simulation volume element are in thermal equilibrium; the heat capacity and thermal conductivity that appear should be taken to be effective properties of the mixed phases. The resistivity that appears is also effective; to more properly account for how it arises, the joule heat should be broken into its two constituent contributions,

$$\rho\left|\left|\vec{i}\right|\right|^2 = \rho_1\left|\left|\vec{i}_1\right|\right|^2 + \rho_2\left|\left|\vec{i}_2\right|\right|^2 . \tag{4.21}$$

$$C_{p,\mathrm{eff}}\frac{\partial T}{\partial t} = \nabla\cdot\left(k_{\mathrm{eff}}\nabla T\right) + \rho_1\left|\left|\vec{i}_1\right|\right|^2 + \rho_2\left|\left|\vec{i}_2\right|\right|^2 + \rho_{\mathrm{k}} i_n^2 - \frac{a_V T\Delta\overline{S}_{\mathrm{rxn}}}{nF} i_n \tag{4.22}$$

Equation (4.22) is the final, practically useful form of the electrochemical thermal energy balance, and is similar to the equation proposed by Srinivasan and Wang [29]. The terms on the right respectively account for heat conduction, Joule heating in the solid, Joule heating in the liquid, Joule heating by interfacial charge transfer, and the reversible heat of reaction associated with that charge transfer.

To get information relevant to typical prismatic battery cells, we assume that the separator side of electrode is insulating,

$$\left.\frac{\partial T}{\partial x}\right|_{x=0} = 0, \tag{4.23}$$

and that the exterior surface at the current collector is cooled by convection,

$$h\left[T\left(\delta\right) - T_\infty\right] = -k_{\mathrm{eff}}\left.\frac{\partial T}{\partial x}\right|_{x=\delta} . \tag{4.24}$$

Here h is an interfacial heat-transfer coefficient.

Table 4-1 summarizes the final set of equations used for analytic solutions and numerical simulations, which will be used in the later sections. The first five equations come from Newman-Tobias theory, and the last equation is the associated energy balance. Note that even this ostensibly 'simple' formulation of an electro-thermal porous-electrode transport model and associated boundary conditions contains many parameters. It is already difficult to see what properties affect the system response, and in what ways.

4.4 Analytic solution

4.4.1 Dimensional analysis and steady-state solution in 1D

Dimensional analysis of the equation system reveals that the physics is controlled by the following parameters:

Control parameter:
$$I = \frac{iR}{a_V n F k_{eff}}; \tag{4.25}$$

Material properties:
$$\sigma = \frac{\Delta \bar{S}_{rxn} \delta_{eff} a_V}{R},\ \alpha^2 = \left(\frac{\rho_1 + \rho_2}{\rho_k} \right) \left(\delta_{eff} a_V \right)^2,\ \mathrm{Bi} = \frac{h \delta_{eff}}{k_{eff}} \text{ and } s = \frac{\rho_2}{\rho_1 + \rho_2}. \tag{4.26}$$

These describe the applied current, along with material characteristics that can be understood as a dimensionless reaction heat σ, a ratio of electric bulk resistance to kinetic resistance α^2, a Biot number Bi (describing the relative importance of interfacial heat transfer in units of bulk heat conduction), and a dimensionless ratio between the electric solid- and liquid-phase resistivies s.

Table 4-1 Final set of equations for thermoelectrochemical modeling.

Physics	Equation	Eqn number
Charge conservation in solid	$\nabla \cdot \vec{i}_1 = a_V i_n$	(4.1)
Charge conservation in liquid	$\nabla \cdot \vec{i}_2 = -a_V i_n$	(4.2)
Ohm's law in solid	$\nabla \Phi_1 = -\rho_1 \vec{i}_1$	(4.5)
Ohm's law in liquid	$\nabla \Phi_2 = -\rho_2 \vec{i}_2$	(4.6)
Interfacial charge transfer	$\rho_k i_n = a_V \left(\Phi_1 - \Phi_2 \right)$	(4.8)
Energy balance	$C_{p,\text{eff}} \frac{\partial T}{\partial t} = \nabla \cdot \left(k_{\text{eff}} \nabla T \right) + \rho_1 \left\| \vec{i}_1 \right\|^2 + \rho_2 \left\| \vec{i}_2 \right\|^2 + \rho_k i_n^2 - \frac{a_V T \Delta \overline{S}_{\text{rxn}}}{nF} i_n$	(4.22)

Note that s is always very close to unity, since the solid phase is so much more conductive than the electrolyte phase. This assumption was adopted to simplify all subsequent analysis.

The control parameter and material properties determine relationships between the dimensionless position ξ, time τ, and the reaction and temperature distributions, X and θ, defined as

Independent variables:

$$\xi = \frac{x}{\delta_{\text{eff}}} \text{ and } \tau = \frac{k_{\text{eff}} t}{C_{p,\text{eff}} \delta_{\text{eff}}^2}, \tag{4.27}$$

Dependent variables:

$$X = \frac{i_1}{i} \text{ and } \theta(\xi) = \frac{R^2 T}{\rho_k n^2 F^2 k_{\text{eff}}}. \tag{4.28}$$

Incorporating the dimensionless quantities and $s = 1$ converts governing equations (4.10) and (4.22) for a 1-D geometry at steady state to

$$\frac{\partial^2 X}{\partial \xi^2} - \alpha^2 (X - 1) = 0, \tag{4.29}$$

$$\frac{d^2\theta}{d\xi^2} + (X-1)^2 + \frac{1}{\alpha^2}\left(\frac{dX}{d\xi}\right)^2 + \frac{\sigma}{I}\frac{dX}{d\xi} = 0. \tag{4.30}$$

The following four boundary conditions close the system of two second-order differential governing equations:

$$X(\xi = 0) = 0, \tag{4.31}$$

$$X(\xi = 1) = 1, \tag{4.32}$$

$$\left.\frac{\partial\theta}{\partial\xi}\right|_{\xi=0} = 0, \tag{4.33}$$

$$\mathrm{Bi}\theta(\xi = 1) = -\left.\frac{\partial\theta}{\partial\xi}\right|_{\xi=1}. \tag{4.34}$$

Following Newman and Tobias [2], the solution equation (4.29) subject to boundary conditions (4.31) and (4.32) is obtained by reduction of order, yielding

$$X(\xi) = 1 - \cosh(\alpha\xi) + \coth(\alpha)\sinh(\alpha\xi). \tag{4.35}$$

Given equation (4.35), the thermal part of the problem can also be solved analytically:

$$\theta(\xi) = \left[1 + \mathrm{Bi}(1-\xi)\right]\left(\frac{\sigma}{\mathrm{Bi}I} + \frac{\coth\alpha}{\alpha\mathrm{Bi}}\right) + \frac{\sigma\left[1 - \cosh\left[\alpha(1-\xi)\right]\right]}{I\alpha\sinh\alpha} - \frac{\sinh^2\left[\alpha(1-\xi)\right]}{2\alpha^2\sinh^2\alpha}. \tag{4.36}$$

Solutions (4.35) and (4.36) are not coupled, but they provide enough of a basis for looking at the effects of dimensionless parameters on simulation output.

Figure 4-8 shows how changing the key material properties affects the steady-state system response with a given applied current $I = 10$. The reaction heat, kinetic resistance, and Biot number are varied around baseline values of $\sigma = 13$, $\alpha = 1$, and Bi = 0.1. Figure 4-8(a) shows the effect of changing σ across values of 13, 0, and –13. The reaction heat changes the shape of the temperature profile significantly (even inducing an inflection point in the distribution for negative values), although the reaction distribution

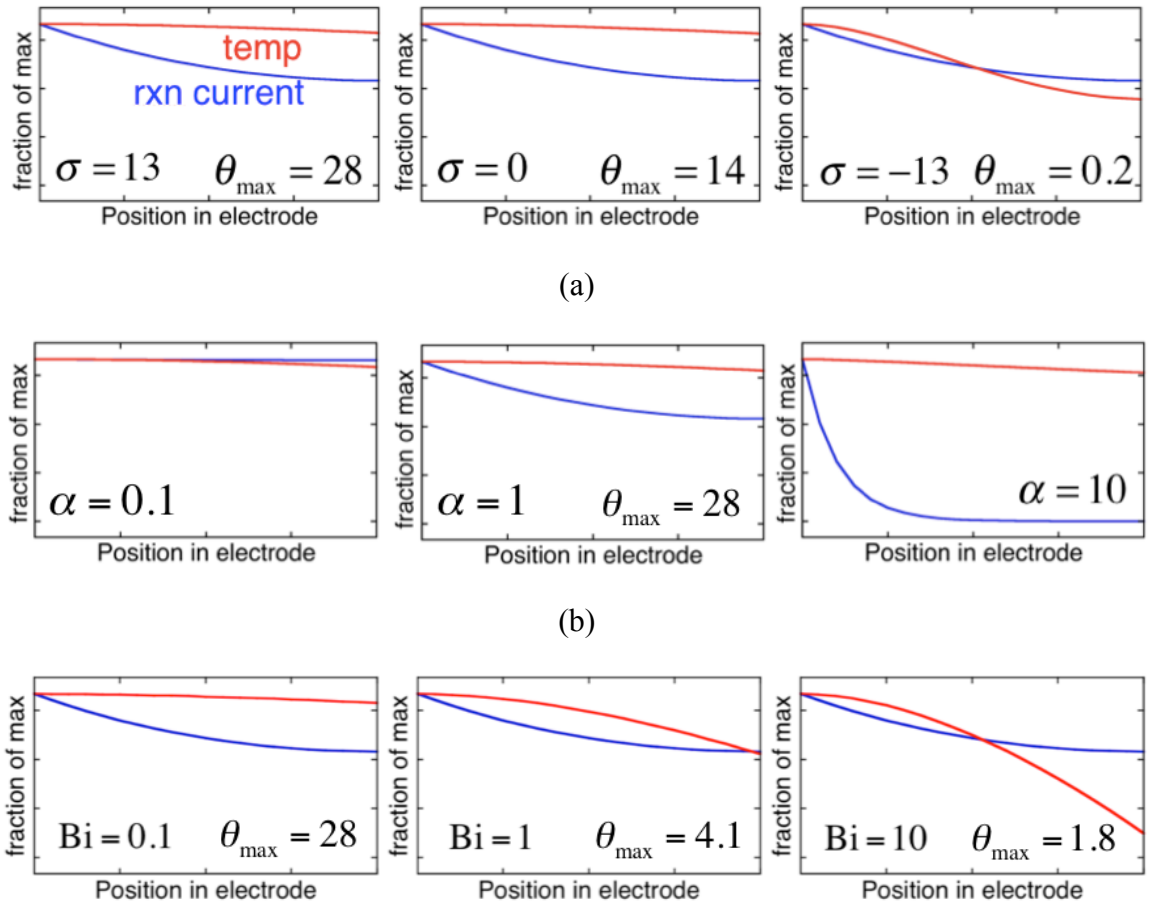

Figure 4-8 The effects of dimensionless parameters on temperature distribution and reaction current in 1D. Test results of (a) reaction heating, (b) the dimensionless ratio between electric bulk resistance and kinetic resistance, and (c) Biot number are shown. Left side of each graph is separator side; right side is current-collector side.

does not change. Figure 4-8(b) shows how profiles are affected by α values of 0.1, 1, and 10. This parameter affects the average temperature as well as the reaction-rate distribution; the effect on the reaction rate is much more significant than that on the temperature distribution, however. Also, as α increases, the reaction distribution becomes more concentrated toward the separator side of the electrode. Figure 4-8(c) shows the effect of Biot number, Bi = 0.1, 1, and 10. In accord with physical intuition, higher Biot numbers drop the average temperature and increase the concavity of the temperature distribution. Being a thermal property, the Biot number has no effect on the reaction distribution.

4.5 Numerical solution

The analytic solution and dimensional analysis in the previous section suggest that three dimensionless material properties primarily control the system response with a given cell geometry. A transient 3-D model was developed to model the A123 15 Ah LFP pouch cell. It was hypothesized that the transient thermal response observed in experiments, which was spatially non-uniform, could be fit by a model to back out estimates of the material properties of the battery. The dimensionless material parameters identified during the analysis in section 4.4 were varied for data fitting.

COMSOL Multiphysics commercial software was used to implement finite-element numerical analysis. The generic partial-differential-equation solver in COMSOL was used to implement the extended Newman-Tobias model equations from table 4-1, with the boundary conditions between current collectors and the positive and negative

electrode domains summarized in Figure 4-9. In the current collectors, Ohm's law was used with a solenoidal current-density ($\nabla \cdot \vec{i} = 0$). The heat equation in the current collector involves no reaction heat.

Once the set of model equations was programmed, material properties, obtained from a literature search were included [29,35,37,38]. Initial results of an excitation-test simulation using these initial estimates of the material properties are shown in Figure 4-10(a). Note that the theoretical relaxation time matches the experimental relaxation time fairly well. The time taken for relaxation to the periodic state can be controlled relatively easily (and independently) by varying the heat capacity of the battery cell in a thermal simulation, effectively changing the units of time involved in the dimensionless time τ. The volumetric heat capacity was varied from expected literature values to achieve the good match of relaxation time shown in the figure.

To implement a better fit of the periodic steady-state response, model sensitivity to the material properties was investigated. The dimensional analysis from the previous section indicates that three dimensionless material properties (σ, α^2, and Bi in equations (4.26)) control the overall behavior. Parameters σ, α^2, and Bi can be varied independently within simulations by changing the dimensional properties $\Delta\overline{S}_{\text{rxn}}$, $\rho_1 + \rho_2$, and h, respectively.

Model sensitivity was evaluated by testing the effects of changing the three dimensionless material parameters on three characteristic features of the periodic steady-state response: the time-averaged mean temperature T_{avg}, the difference between the time-averaged maximum temperature and the time-averaged mean temperature $T_{\max} - T_{\text{avg}}$, and

Figure 4-9 Bandmap of 3-D numerical modeling.

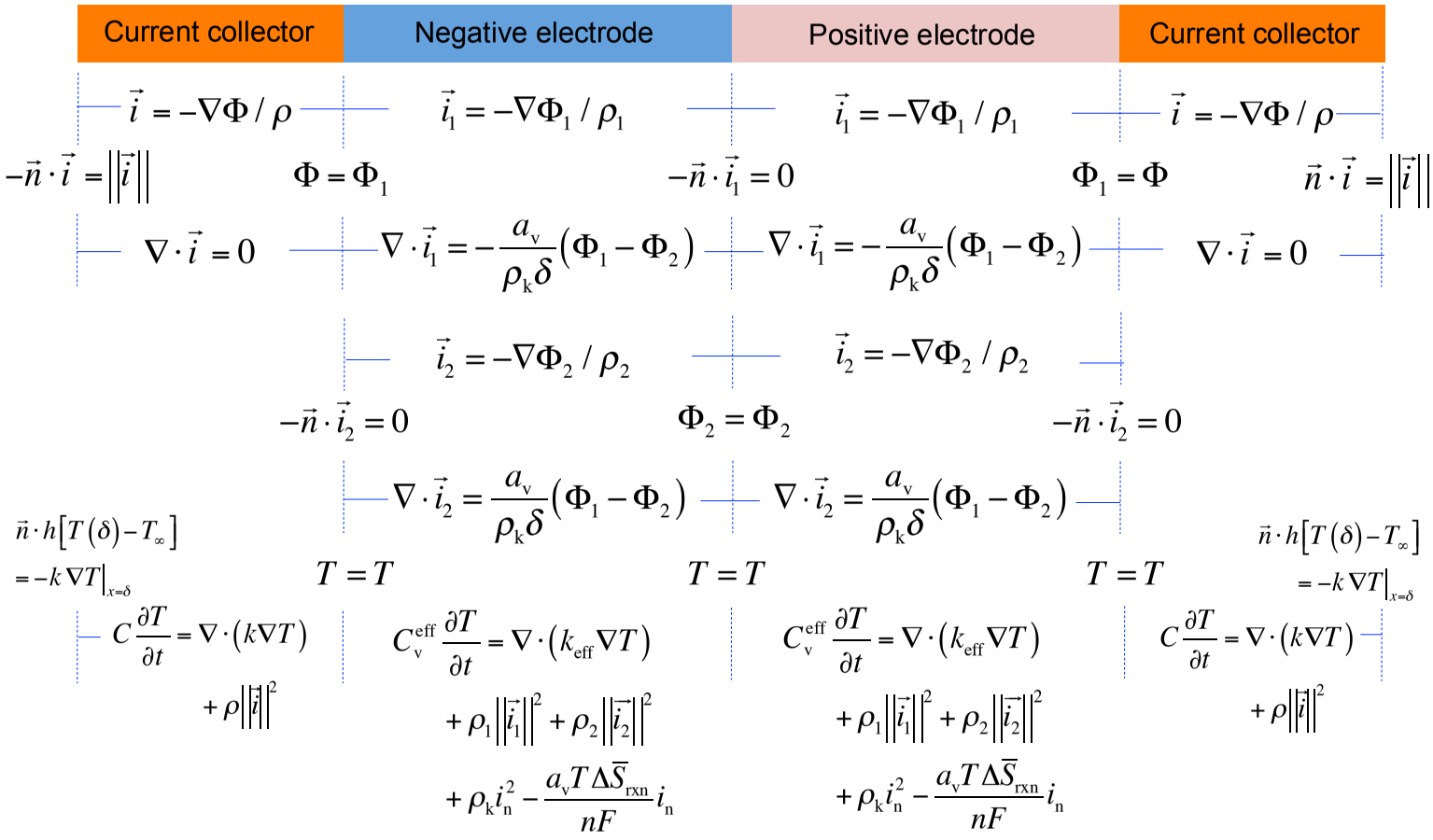

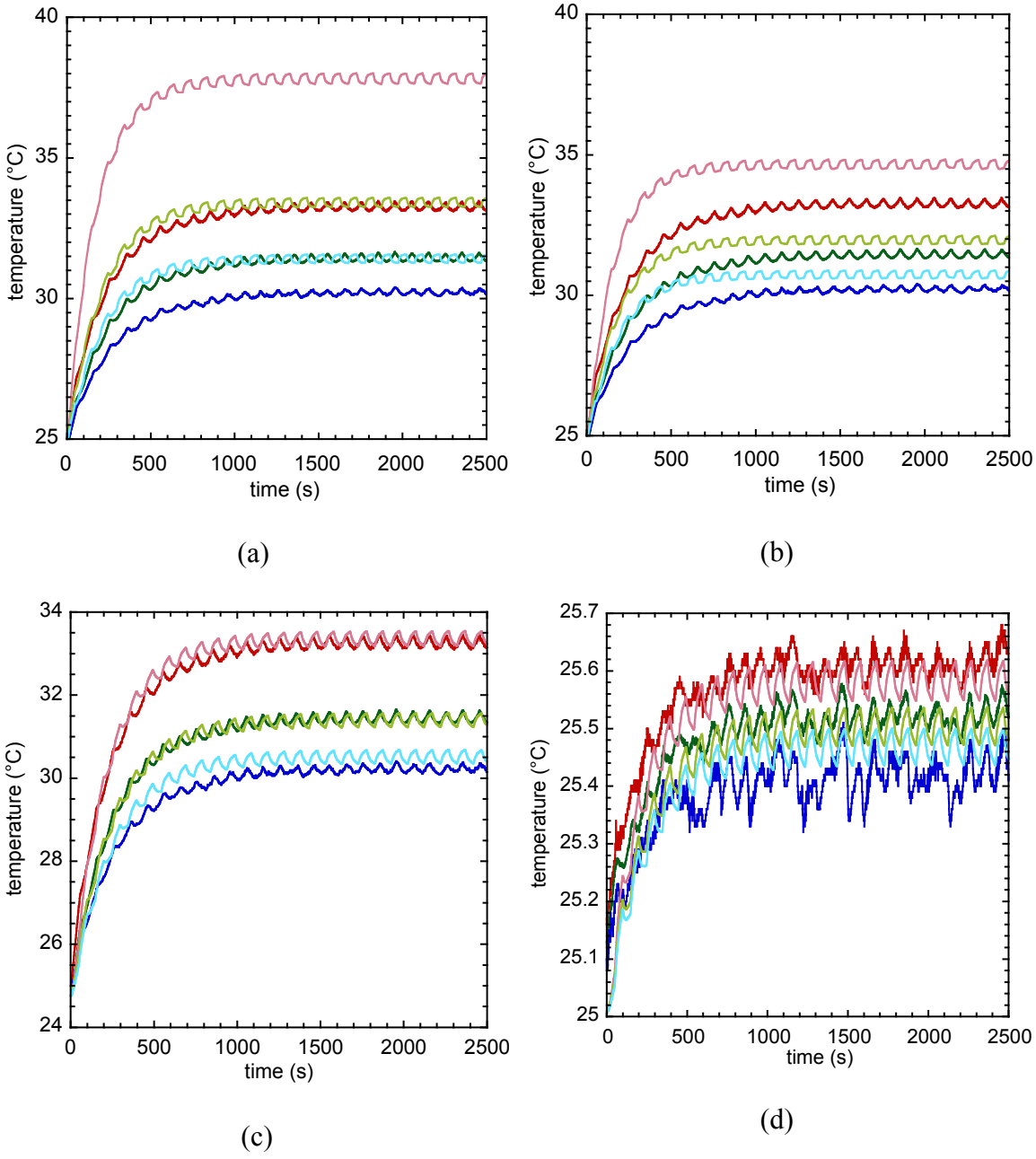

Figure 4-10 Comparisons of experimental (light lines) and theoretical (dark lines) transient temperature responses of the A123 15 Ah LFP pouch cell for excitation tests with A = 5C and p = 100s ((a), (b), and (c)) and A=1C and p = 100s (d). The set of dimensionless numbers for each graph: (a) σ = 15086, α^2 = 544.38, Bi = 0.073667 (b) σ = 16293, α^2 = 954.11, Bi = 0.11418, (c,d) σ = 28825.4, α^2 = 1354.6, Bi = 0.15371.

the amplitude of the temperature fluctuations in the periodic steady state, ΔT_{fluc}. These factors were selected as representative output characteristic because the spatial-average and maximum temperatures are critical to battery safety, and the fluctuation amplitude contains information about the entropy of the cell reaction.

Model sensitivity can be summarized qualitatively using a Jacobian matrix that expresses variations in the three representative output characteristics with respect to the material properties. The Jacobian used to analyze model sensitivity was

$$\boldsymbol{J} = \begin{bmatrix} \partial T_{\text{avg}} / \partial \sigma & \partial T_{\text{avg}} / \partial \alpha^2 & \partial T_{\text{avg}} / \partial \text{Bi} \\ \partial \left(T_{\text{max}} - T_{\text{avg}} \right) / \partial \sigma & \partial \left(T_{\text{max}} - T_{\text{avg}} \right) / \partial \alpha^2 & \partial \left(T_{\text{max}} - T_{\text{avg}} \right) / \partial \text{Bi} \\ \partial \Delta T_{\text{fluc}} / \partial \sigma & \partial \Delta T_{\text{fluc}} / \partial \alpha^2 & \partial \Delta T_{\text{fluc}} / \partial \text{Bi} \end{bmatrix}. \tag{4.37}$$

With four different runs of the transient excitation-test simulation – one baseline calculation, followed by three calculations that perturb σ, α^2, and Bi around the baseline – this matrix can be calculated numerically with fair accuracy. Once known, the Jacobian can be used to implement a step of a multi-dimensional goal seek by the Newton-Raphson method. To first order, the target (experimental) values of the properties relate to the initial baseline guesses and the Jacobian through

$$\begin{bmatrix} T_{\text{avg}}^{\text{expl}} \\ T_{\text{max}}^{\text{expl}} - T_{\text{avg}}^{\text{expl}} \\ \Delta T_{\text{fluc}}^{\text{expl}} \end{bmatrix} = \begin{bmatrix} T_{\text{avg}}^{0} \\ T_{\text{max}}^{0} - T_{\text{avg}}^{0} \\ \Delta T_{\text{fluc}}^{0} \end{bmatrix} + \boldsymbol{J} \begin{bmatrix} \sigma_1 - \sigma_0 \\ \alpha_1^2 - \alpha_0^2 \\ \text{Bi}_1 - \text{Bi}_0 \end{bmatrix} + O\left(\begin{bmatrix} \left\| \sigma_1 - \sigma_0 \right\|^2 \\ \left\| \alpha_1^2 - \alpha_0^2 \right\|^2 \\ \left\| \text{Bi}_1 - \text{Bi}_0 \right\|^2 \end{bmatrix} \right), \tag{4.38}$$

where ‘expl’ in the superscript represents a targeted experimental value of a property.

After finding the rough match of experimental output shown in Figure 4-10(a), each of the three dimensionless parameters (σ, α^2, and Bi) was perturbed by about 10%, and the consequent changes in T_{avg}, $T_{\max} - T_{\text{avg}}$, and ΔT_{fluc} were tracked to see the effects on the periodic steady-state response. The resulting Jacobian matrix was

$$\boldsymbol{J}_1 = \begin{bmatrix} 0\text{K} & 0.00699427\text{K} & -114.154\text{K} \\ 0\text{K} & -0.000869227\text{K} & -52.1958\text{K} \\ -2.5683\times10^{-5}\text{K} & -0.000201948\text{K} & -0.306737\text{K} \end{bmatrix}. \tag{4.39}$$

This shows that the dimensionless reaction heat σ affects only the fluctuating-temperature amplitude T_{fluc}. On the basis that the entries in the rightmost column are large, one might think that the Biot number dominates the system response; bear in mind, however, that the orders of the dimensionless numbers σ, α^2, and Bi are 10^5, 10^2, and 10^{-2}, respectively. Thus all three factors have relatively significant effects on the periodic steady-state temperatures.

One can read $T_{\text{avg}}^{\text{expl}}$, $T_{\max}^{\text{expl}}$, and $\Delta T_{\text{fluc}}^{\text{expl}}$ directly from a plot of experimental excitation data; the temperatures T_{avg}^{0}, $T_{\max}^{0}$, and $\Delta T_{\text{fluc}}^{0}$ can be obtained from a simulation with initial property guesses σ_0, α_0^2, and Bi_0. Once these numbers and the Jacobian are obtained, equation (4.38) can be inverted (neglecting terms of quadratic order and higher) to calculate a new set of guesses for the dimensionless parameters: σ_1, α_1^2, and Bi_1. These updated material properties can be included in the simulation by altering the values of $\Delta\overline{S}_{\text{rxn}}$, $\rho_1 + \rho_2$, and h in the code; the updated properties yield a curve that fits the experimental data better (as in Figure 4-10(b)). At this stage, a second Jacobian matrix

can be numerically calculated; repeating the application of equation (4.38) yields updated properties that provide the best fit in Figure 4-10(c). Note that the nontrivial entries in the second Jacobian were observed to differ somewhat from their values in the first, suggesting significant nonlinearity of the model output with respect to the dimensionless material parameters.

Figure 4-10(d) illustrates the extrapolative capability of the model. Theory and experiment match for excitation data at a different C rate (A = 1 C) than the rate used for parameter estimation (A = 5 C). It is worthwhile to note that the simulation matches experimental data at both C rates well within the experimental error of temperature measurement (~0.5 °C). The match supports the assertion that a simple thermo-electrochemical model based on Newman-Tobias theory with linear kinetics suffices.

The output shown in Figures 4-10(c) and 4-10(d) show that the dimensionless quantities that control the system response are accurate. The goal-seeking procedure used to achieve this fit involved changing dimensional quantities whose effects on individual dimensionless parameters were independent, however, leading dimensional properties in the simulation to have incorrect values. The model contains 10 dimensional properties. Given that the 7 dimensionless control parameters, dependent variables, and material properties must remain invariant for the data to be fit well, a choice of 3 independent dimensional properties can be used to fix the units on all the other dimensional properties. To establish the 7 free dimensional property values, the heat capacity C_p = 700 J/kg-K, effective thickness δ_{eff} = 0.0026 m (half of the battery thickness), and current density i = 15 A * C rate /(cross-sectional area of current collector) were used.

The ratio of $k_{\text{eff}} / C_{p,\text{eff}}\delta_{\text{eff}}^2$ in dimensionless time τ should be constant; therefore, to maintain invariance of dimensionless time, given dimensional values of C_p and δ_{eff}, the effective thermal conductivity k_{eff} is fixed; once k_{eff} is known, the invariance of the Biot number can be used to fix the convective heat transfer coefficient h; *etc*. The final, consistent set of dimensional properties is listed in Table 4-2. As expected, when the simulation was run with these updated dimensional properties, the output did not change.

All the values in Table 4-2 appear reasonable. The convective heat transfer coefficient h and the exchange current density i_0 are very similar to previously reported values [29]. The surface-to-volume ratio a_V is difficult to measure directly, but is well within an expected range [35]. The effective thermal conductivity k_{eff}, the electrical resistances ρ_1 and ρ_2, and reaction-entropy change ΔS_{rxn} are slightly different from literature values, but they are of the same order of magnitude [29]. Since the composition of the A123 battery materials is not exactly known, this difference is justified.

4.6 Conclusion

A thermoelectrochemical model that modifies the isothermal Newman-Tobias model to account for a local thermal energy balance was developed and used to match experimental temperature-distribution data for a cycling A123 15 Ah LFP Li-ion pouch cell. Three critical dimensionless variables were found to control the response in a 1-D galvanostatic steady state; the same parameters were found to control the output of a 3-D simulation of a current-square-wave excitation test. Although the extreme non-uniform

Table 4-2 Final set of equations for thermoelectrochemical modeling.

Dimensionless number	Suggested property	Literature values
$\tau = \frac{k_{\text{eff}} t}{C_{p,\text{eff}} \delta_{\text{eff}}^2}$	$k_{\text{eff}} = 0.249$ W/m-K	$k_{\text{eff}} = 1 \sim 5$ W/m-K [29]
$\text{Bi} = \frac{h \delta_{\text{eff}}}{k_{\text{eff}}}$	$h = 14.74$ W/m^2-K	$h = 10 \sim 200$ W/m^2-K
$I = \frac{iR}{a_V nF k_{\text{eff}}}$	$a_V = 1.2 \times 10^6$ m^{-1}	$a_V = 10^7$ m^{-1} [35]
$\sigma = \frac{\Delta \overline{S}_{\text{rxn}} \delta_{\text{eff}} a_{\text{V}}}{R}$	$\Delta \overline{S}_{\text{rxn}} / nF = 0.794$ mV/K	$\Delta \overline{S}_{\text{rxn}} / nF \sim 0.3$ mV/K [29]
$\theta(\xi) = \frac{R^2 T}{\rho_{\text{k}} n^2 F^2 k_{\text{eff}}}$	$\rho_{\text{k}} = 10^9$ Ω-m $(i_0 = 1.33$ A/m$^2)$	$i_0 = 0.8 \sim 1.1$ A/m^2 [29]
$\alpha^2 = \left(\frac{\rho_1 + \rho_2}{\rho_{\text{k}}} \right) (\delta_{\text{eff}} a_{\text{V}})^2$	$\rho_1 = 0.00107$ Ω-m; $\rho_2 = 0.133$ Ω-m	$\rho_1 = 0.018$ Ω-m $\rho_2 = 0.77$ Ω-m [37, 38]

temperature of the A123 battery is a sign of suboptimal battery-cell design, it provides a tool by which one can use external measurements of cell surface temperature to estimate properties of materials within the cell. Using dimensional analysis and an iterative procedure based on a numerically computed goal-seeking algorithm, estimates of the A123 15 Ah LFP battery's material properties were obtained. It was shown that the model had extrapolative capability; best-fit parameters obtained from a model fit at high C rate could be used to predict the output at a lower C rate.

4-A Appendix: thermodynamic analysis

A thermodynamic analysis relating the heat generation by reaction term in equation (4.22) to interfacial charge-transfer reaction parameters is illustrated below.

$$\sum_i \bar{H}_i R_i$$
$$= \sum_i \left(\mu_i + T\bar{S}_i\right) R_i$$
$$= \sum_i \left(\mu_i + T\bar{S}_i\right) s_i r$$
$$= r \sum_i \left(s_i \mu_i + T s_i \bar{S}_i\right)$$
$$= \frac{a_v i_n}{nF} \sum_i s_i \mu_i + T \frac{a_v \sum_i s_i \bar{S}_i}{nF} i_k$$
$$= -\eta_s a_v i_n + \frac{a_v T \Delta\bar{S}_{rxn}}{nF} i_n$$
$$= -\frac{a_v RT}{i_0 nF} i_n^2 + \frac{a_v T \Delta\bar{S}_{rxn}}{nF} i_n$$

Irreversible Reversible

$\bar{H}_i$: partial molar enthalpy of species i $\left(\bar{H}_i = \mu_i + T\bar{S}_i\right)$

$$\bar{H}_i = \frac{\partial H_i}{\partial n_i}[=]\frac{\text{J}}{\text{mol}}$$

R_i : production rate of species i

$$R_i = s_i r [=] \frac{\text{mol}}{\text{m}^3 \cdot \text{s}}$$

r : total reaction rate, $r = \frac{a_v i_n}{nF}[=]\frac{1}{\text{m}^3 \cdot \text{s}}$

η_s : overpotential, $\eta_s[=]\text{V}$

$$\eta_s = \frac{1}{nF}\sum_i s_i \mu_i = \Phi_e - \Phi_s$$

$\Delta\bar{S}_{rxn}$: partial molar entropy change of reaction, $\Delta\bar{S}_{rxn}[=]\text{J/mol}\cdot\text{K}$

$$\Delta\bar{S}_{rxn} = \sum_i s_i \bar{S}_i$$

i_n : local reaction rate @ interface, $i_n[=]\text{A/m}^2$

$$i_n = \frac{i_0 nF}{RT}\eta_s$$

4.7 References

[1] T. M. Bandhauer, S. Garimella, and T. F. Fuller, Journal of The Electrochemical Society **158**, R1 (2011).
[2] J. S. Newman and C. W. Tobias, **109**(12), 1183 (1962).
[3] M. Doyle, T. Fuller, and J. Newman, "Modeling of Galvanostatic Charge and Discharge of the Lithium Polymer Insertion Cell," *J. Electrochem. Soc.*, vol. 140, no. 6, pp. 1526–1533, Jun. 1993.
[4] T. Fuller, M. Doyle, and J. Newman, "Simulation and Optimization of the Dual Lithium Ion Insertion Cell," *J. Electrochem. Soc.*, vol. 141, no. 1, pp. 1–10, Jan. 1994.
[5] T. F. Fuller, M. Doyle, and J. Newman, "Relaxation Phenomena in Lithium-Ion-Insertion Cells," *J. Electrochem. Soc.*, vol. 141, no. 4, pp. 982–990, Apr. 1994.
[6]http://www.nbcnews.com/travel/boeing-787-dreamliner-catches-fire-bostons-logan-airport-1B7832998 (last visited Aug. 17, 2013)
[7]http://www.reuters.com/article/2013/01/07/us-boeing-787-boston-idUSBRE9060JB20130107 (last visited Aug. 17, 2013)
[8]http://online.wsj.com/article/SB10001424127887323482504578227621155767836.html?KEYWORDS=boeing+fire (last visited Aug. 17, 2013)
[9]http://www.lemonde.fr/economie/article/2013/01/17/les-boeing-787-cloues-au-sol-le-systeme-des-batteries-examine_1818123_3234.html (last visited Aug. 17, 2013)
[10] Deborah A.P. Hersman, "Investigative Update of Battery Fire Japan Airlines B-787-Jan 7, 2013", National Transport Safety Board.
[11] K. H. Kwon, C. B. Shin, T. H. Kang, and C.-S. Kim, "A two-dimensional modeling of a lithium-polymer battery," Journal of Power Sources, vol. 163, no. 1, pp. 151–157, Dec. 2006.
[12] G.-H. Kim, K. Smith, K.-J. Lee, S. Santhanagopalan, and A. Pesaran, "Multi-Domain Modeling of Lithium-Ion Batteries Encompassing Multi-Physics in Varied Length Scales," Journal of The Electrochemical Society, vol. 158, no. 8, pp. A955–A969, 2011.
[13] U. S. Kim, J. Yi, C. B. Shin, T. Han, and S. Park, "Modeling the Dependence of the Discharge Behavior of a Lithium-Ion Battery on the Environmental Temperature," J. Electrochem. Soc., vol. 158, no. 5, pp. A611–A618, May 2011.
[14] U. S. Kim, J. Yi, C. B. Shin, T. Han, and S. Park, "Modelling the thermal behaviour of a lithium-ion battery during charge," Journal of Power Sources, vol. 196, no. 11, pp. 5115–5121, Jun. 2011.
[15] S. Peck and M. Pierce, "Development of a Temperature-Dependent Li-ion Battery Thermal Model," SAE International, Warrendale, PA, 2012-01-0117, Apr. 2012.
[16] P. Ramadass, B. Haran, R. White, and B. N. Popov, "Mathematical modeling of the capacity fade of Li-ion cells," *Journal of Power Sources*, vol. 123, no. 2, pp. 230–240, Sep. 2003.
[17] R. Wright, C. Motloch, J. Belt, J. Christophersen, C. Ho, R. Richardson, I. Bloom, S. Jones, V. Battaglia, G. Henriksen, T. Unkelhaeuser, D. Ingersoll, H. Case, S. Rogers, and R. Sutula, "Calendar- and cycle-life studies of advanced technology development program generation 1 lithium-ion batteries," Journal of Power Sources, vol. 110, no. 2, pp. 445–470, Aug. 2002.

[18] M. R. Zakin, R. O. Brickman, D. M. Cox, and A. Kaldor, "Dependence of metal cluster reaction kinetics on charge state. I. Reaction of neutral (Nbx) and ionic (Nb+x, Nb−x) niobium clusters with D2," The Journal of Chemical Physics, vol. 88, no. 6, pp. 3555–3560, Mar. 1988.
[19] H. Maleki, S. Al Hallaj, J. R. Selman, R. B. Dinwiddie, and H. Wang, J. Electrochem. Soc., 146, 947 (1999).
[20] S. Al Hallaj, R. Venkatachalapathy, J. Prakash, and J. R. Selman, J. Electrochem. Soc., 147, 2432 (2000).
[21] K. E. Thomas and J. Newman, "Heats of mixing and of entropy in porous insertion electrodes," Journal of Power Sources, vol. 119–121, no. 0, pp. 844–849, Jun. 2003.
[22] K. E. Thomas and J. Newman, "Thermal Modeling of Porous Insertion Electrodes," *J. Electrochem. Soc.*, vol. 150, no. 2, pp. A176–A192, Feb. 2003.
[23] K. E. Thomas, C. Bogatu, and J. Newman, "Measurement of the Entropy of Reaction as a Function of State of Charge in Doped and Undoped Lithium Manganese Oxide," Journal of The Electrochemical Society, vol. 148, no. 6, pp. A570–A575, 2001.
[24] M. W. Verbrugge and R. S. Conell, "Electrochemical and Thermal Characterization of Battery Modules Commensurate with Electric Vehicle Integration," J. Electrochem. Soc., vol. 149, no. 1, pp. A45–A53, Jan. 2002.
[25] Xinfan Lin, Hector E. Perez, Jason B. Siegel, Anna G. Stefanopoulou, Yonghua Li, R. Dyche Anderson, Yi Ding, and Matthew P. Castanier. "Online parameterization of lumped thermal dynamics in cylindrical lithium ion batteries for core temperature estimation and health monitoring," IEEE Transactions on Control System Technology, 2013
[26] Hector E. Perez, Jason B. Siegel, Xinfan Lin, Yi Ding, and Matthew P Castanier, "Parameterization and validation of an integrated electro-thermal lfp battery model," *ASME Dynamic Systems Control Conference*, Oct 2012.
[27] Kim, Y.; Siegel, J. B. & Stefanopoulou, A. G. A Computationally Efficient Thermal Model of Cylindrical Battery Cells for the Estimation of Radially Distributed Temperatures," *American Control Conference,* 2013
[28] Kim, Y.; Mohan, S.; Siegel, J. B.; Stefanopoulou, A. G. & Ding, Y. "The Estimation of Radial Temperature Distribution in Cylindrical Battery Cells under Unknown Cooling Conditions," IEEE Conference on Decision and Control, 2013
[29] V. Srinivasan and C. Y. Wang, "Analysis of Electrochemical and Thermal Behavior of Li-Ion Cells," J. Electrochem. Soc., vol. 150, no. 1, pp. A98–A106, Jan. 2003.
[30] J. Christensen, P. Albertus, and D. Cook, "3D Thermoelectrochemical model of a Li-ion model" AABC (Adv. Automotive Batt. Conf.) Jan 24th, 2011.
[31] J. Christensen, P. Albertus, and D. Cook, "3D Thermoelectrochemical model of a Li-ion model" JECS, 2013. (In preparation)
[32] S. U. Kim, C. W. Monroe, P. Albertus, D. Cook and J. Christensen, "Thermoelectrochemical simulations of performance and abuse in 50-Ah automotive cells." J. Power Sources, (in preparation)
[33] M. Fleckenstein, O. Bohlen, M. A. Roscher, and B. Bäker, "Current density and state of charge inhomogeneities in Li-ion battery cells with LiFePO4 as cathode material due to temperature gradients," *Journal of Power Sources*, vol. 196, no. 10, pp. 4769–4778, May 2011.

[34] D. Bernardi, E. Pawlikowski, and J. Newman, "A General Energy Balance for Battery Systems," J. Electrochem. Soc., vol. 132, no. 1, pp. 5–12, Jan. 1985.
[35] J. Newman and K. E. Thomas-Alyea, *Electrochemical Systems,* 3rd ed. Wiley-Interscience, 2004.
[36] W. M. Deen, *Analysis of transport phenomena*. New York: Oxford University Press, 2012.
[37] M. Doyle and Y. Fuentes, "Computer Simulations of a Lithium-Ion Polymer Battery and Implications for Higher Capacity Next-Generation Battery Designs," J. Electrochem. Soc., vol. 150, no. 6, pp. A706–A713, Jun. 2003.
[38] S. G. Stewart, "Determination of Transport Properties and Optimization of Lithium-Ion Batteries," Ph.D. Thesis, University of California at Berkeley, December, 2007.

Chapter 5 Thermoelectrochemical simulations of performance and abuse in 50-Ah automotive Li-ion cells

This chapter also deals with thermoelectrochemical simulations, but extends the basic model discussed in the previous chapter to account for mass-transfer effects within the battery cell. Simultaneous charge and mass transfer in two-phase porous electrodes is simulated here using the standard Dualfoil model [1-3], augmented with a local thermal energy balance, equation (4.22). For this effort, a more sophisticated meshing procedure than that used in chapter 4 was needed for two reasons: (1) Dualfoil operates under an assumption that simulation volume elements are locally isothermal; and (2) Combined thermal and electrochemical/diffusive transport simulation is too computationally expensive. Thus a mapping between two mesh systems – one used for electrochemical computations, and one for thermal computations – was essential.

The Dualfoil model includes mass diffusion in solid-particle, pore-filling-liquid, and separator domains, requiring several additional transport equations that augment the basic Newman-Tobias model [4] used in chapter 4. One practical ramification of this added model complexity is that simulations require significantly greater computation times. Although the duration of a simulation depends somewhat on the meshing used, a given simulation with the Newman-Tobias model tends to run in about a fifth the time taken for a comparable simulation with Dualfoil. (Note that the Newman-Tobias-type

calculations from chapter 4 took from 4-8 hours to complete; the thermal extension of Dualfoil reported here requires more than a day per run on a comparable CPU.)

After testing the effects of different thermal boundary conditions (natural and forced convection), various tests are also executed with the developed model, especially focusing on safety issues such as lithium plating (which occurs at extreme voltages, even at low temperatures) and thermal runaway (which occurs due to chemical instability at high temperatures, even at moderate voltages). The work summarized in this chapter was performed in collaboration with researchers at Robert Bosch Research and Technology Center in Palo Alto, California.

5.1 Introduction

Thermal phenomena in lithium-ion batteries have received significant interest recently, as they significantly impact both aging and safety [5,6]. Many groups have researched how temperature affects capacity fade and power fade [7-15]. Higher ambient operating temperatures have been shown to result in greater capacity fade, which has been attributed to degradation of the negative electrode [7,8] and loss of cyclable lithium due to SEI growth [9]. Thomas *et al*. [10] reported that the internal impedances of battery cells depend on storage temperature, suggesting that thermal phenomena may also play a part in power fade.

Most aging models (such as those in references [8] and [15]) rely on semi-empirical equations that provide expected capacity or power fades as functions of time, state of charge (SOC), and operation or storage temperature. These phenomenological approaches to battery aging have neglected the effects of thermal and chemical

inhomogeneities inside the battery cell. In other words, the impact of temperature gradients and the resulting current-density and SOC gradients inside the anode/separator/cathode 'jellyroll' have not been considered, even though temperature can be highly non-uniform in some battery geometries, particularly during prolonged charge or discharge at high C rate [16,17]. Temperature and the extent of cell reaction (*i.e.*, local SOC) both influence the rates of aging processes; if these are highly inhomogeneous locally, it is possible that the global effects on aging could be significant.

Fleckenstein *et al*. suggested an interesting method to approach local inhomogeneity within the battery cell [6]. They modeled a 32113 cylindrical cell using an equivalent-circuit-based model (ECM) [18,19] for the electrochemical response of each volume element in the battery interior. Using the local values of current from the ECMs, the Joule heating (I^2R) and local reversible heats of reaction ($IT\ dU/dT$) could be evaluated in each volume element, coupling the local ECMs to a partial differential equation describing the detailed local heat balance. Although Fleckenstein *et al*.'s model yields a local temperature distribution, and can match experimental data effectively, it has the same limitation of other ECMs: the resistors and capacitors involved in the electrical model do not have clear physical interpretations. Thus it is difficult to use fits of data to get information about degradation processes.

Recently Christensen *et al*. introduced a different method to analyze thermal inhomogeneity in 18650 lithium-ion cells [20,21]. They suggested expanding the one-dimensional electrochemical cell-sandwich model (the standard Dualfoil model) [1-3] instead of relying on an ECM. The Dualfoil model is based on detailed models of interfacial electrochemistry and multi-phase electrochemical transport. Within Dualfoil,

lithium transport in the electrolyte and both electrodes is modeled explicitly, as are interfacial reaction kinetics and reaction thermodynamics. Typical implementations of Dualfoil assume the cell sandwich to exist at a nearly uniform temperature, suggesting that the Biot number of the battery cell is relatively small and its internal heat conductance is relatively high [22]. Dualfoil receives current or voltage as input variables, and returns voltage or current (respectively), along with additional information such as SOC, extent of concentration polarization in the separator, and surface overpotentials in the anode and cathode. See 5-A Appendix for the Dualfoil equations used in this work.

Bosch researchers proposed several techniques to couple the Dualfoil model to a local energy-balance equation. The key is to separate the thermal and electrochemical problems, solving the two models sequentially at a given timestep. This approach allows the spatial domain of the problem to be separately meshed for the electrochemical and thermal phenomena. (This is appropriate, since the characteristic length scales for the mass-transfer processes in a single layer of the jellyroll differ significantly from the characteristic length scale for heat transfer across the cell.) The entire battery was divided into a number of electrochemical volume elements, each of which was modeled by a one-dimensional cell-sandwich model essentially identical to the original implementation of Dualfoil, but modified for the curvature of the layer. At the same time, the battery cell was divided into a set of thermal volume elements, which do not necessarily coincide with the electrochemical elements. Exemplary thermal and electrochemical meshings used for the past simulations by Christensen *et al.* [20,21] are reprinted in Figure 5-1. Generally the thermal meshing is finer than the electrochemical meshing; to implement

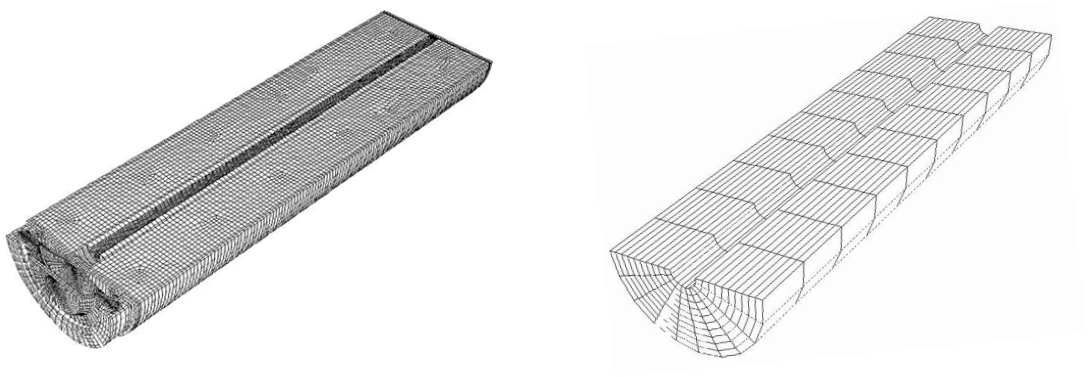

Figure 5-1 Two different meshings of an 18650 (18 mm x 65 mm cylindrical) Li-ion battery cell. (a) Thermal mesh (b) electrochemical mesh. Reproduced from reference 20.

simulations, each electrochemical volume element is taken to exist at the average temperature of the thermal elements it contains. The solution process is as follows: first, the electrochemical problem is solved throughout the cell; once convergence is reached, the heat-generation rate in each electrochemical element is passed to the thermal model; the temperature in each thermal element is subsequently updated, and the updated temperatures are returned to the electrochemical elements for the next time step.

Although the characteristic length for mass transport is on the order of the thickness of a single layer of the jellyroll, the effect of locally varying temperature is fairly weak. Thus the work by Christensen *et al.* justified the use of a coarser-grained electrochemical meshing, showing that the local electrochemical response was minimally affected by temperature gradients for electrochemical volume elements below a certain size [20,21]. On the other hand, the desire to observe local variation of local electrochemical variables such as current density, electrode charge state, and overpotential – not to mention the computational expense of Dualfoil – places an upper bound on the electrochemical mesh size. Thus there should be an optimal electrochemical mesh size that describes local electrochemical transport sufficiently accurately, contains cells across which temperature gradients are minimal, and is computationally efficient.

This work expands Christensen *et al*.'s method to larger lithium-ion batteries, and provides a tool for simulating aging and assessing battery safety. Large-capacity lithium-ion cells have received significant interest in the past several years because of the high energy demands set by a variety of applications, including transportation [23]. In the past, electric-vehicle batteries have comprised packs of 18650 batteries (2~3 Ah capacity per cell). The market is moving to larger capacity cells such as the LEV50 (50-Ah per cell):

their surface-to-volume ratio is lower, reducing packaging cost; the total energy density of the battery system (including the battery casing itself, as well as peripherals such as mounting brackets, exhaust-gas manifolds, and control circuitry) can be increased, saving space. But the same reductions in surface-to-volume ratio that lower costs and raise energy density make thermal management more difficult, calling for a better understanding of coupled electrochemical/thermal processes.

5.2 Model description

A representation of the GS Yuasa LEV50 cell geometry was created, using details of the casing configuration from the company website [24]. The battery geometry used for our simulation is shown in Figure 5-2, which also illustrates the thermal mesh. Information about the battery interior was unavailable (it is intellectual property of GS Yuasa Inc.); therefore, plausible assumptions were made about the geometric configuration and materials used within the cell interior. The mesh was built using Gambit (Ansys Inc.) [25]. The whole thermal mesh is composed of 1mm^3 hexahedral volume elements, for a total of 678,862. In contrast, the electrochemical model used to describe the jellyroll within the cell comprises larger ($230\ \text{mm}^3$) volume elements, for a total of 3,375 ($= 15^3$); the electrochemical volume elements were taken to be simple parallelepipeds, delineated by 15 mesh points each in the x, y, and z directions of the jellyroll. The current collector parts do not require the electrochemical mesh because there is no electrochemical reaction or mass diffusion; however, volumetric heat generation (Joule heating) is separately evaluated, and is included in the thermal equation.

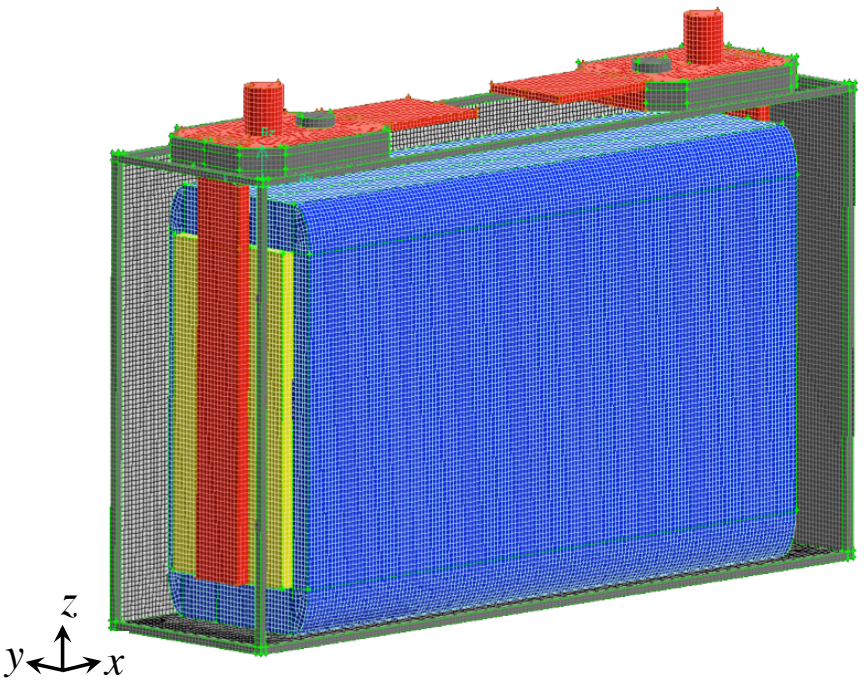

Figure 5-2 Thermal meshing of the GS Yuasa LEV50 cell geometry (the exterior casing is 171 mm L x 44 mm W x 115 mm H). The blue domain represents the jellyroll; yellow represents copper, and red, nickel. An additional aluminum current collector on the right side of the battery cell is obscured by the jellyroll. (The jellyroll and current collectors are also subdivided by the electrochemical mesh.) An extremely low-pressure gas (or vacuum) was assumed to occupy the space between the jellyroll and the casing.

Since the battery geometry is prismatic, the code mapping between electrochemical cells and thermal cells [20,21] was rewritten to use a three-dimensional Cartesian coordinate rather than a cylindrical coordinate, as well (*i.e.*, the Dualfoil implementation was simplified to mirror the original geometry used by Doyle *et al*. [1-3]). For details about the procedures used to map temperatures between electrochemical and thermal simulation steps, see references 20 and 21.

Different domains within the cell were modeled with different heat-generation terms in the local energy balance. For the jellyroll, all possible sources of electrochemical heat generation were included: irreversible Joule heating from the internal impedances of the electrodes and separator, as well as reversible heating from entropy change in each electrode material. For the current collectors, only irreversible Joule heating was included. No heat generation terms were included in the stainless-steel housing domain, which was assumed to be electrically isolated from the jellyroll and tabs.

The thermal properties used to parameterize different domains of the cell are summarized in Table 5-1. The Fluent material database provided property values for steel, nickel, copper, and aluminum, taken from a variety of sources [26-28]. Properties of the jellyroll were also taken from another literature [29].

In general, the jellyroll consists of a spirally wound electrode stack. In the case of cylindrical cells, the jellyroll is macroscopically modeled as a homogenous hollow cylinder with anisotropic heat conduction properties because more layers per length increase the thermal contact resistance – exhibiting low radial, and high axial and polar, thermal conductivities [6]. Although the GS Yuasa cell is also spirally wound, the

Table 5-1 Assumed thermal properties of the GS-Yuasa LEV50 [26-29]. Anisotropic thermal conductivities are included in the jellyroll [6] (see Figure 5-3(b) for more information about the thermal conductivities in the *z* direction).

Volume	Material	k (W/m-K)	ρ (kg/m^3)	c_p (J/kg-K)
Jellyroll	Multiple	*x*: 28 *y*: 1.5 *z*: 1.5, 28	2708.2	781.38
Housing	Steel	16.27	8030	502.48
Current collector	Nickel	91.74	8900	460.6
	Copper	387.6	8978	381
	Aluminium	202.4	2719	871

configuration of the winding makes it better considered as a multilayer sandwich over the majority of its volume. Figure 5-3(a) is taken from a patent [30], which illustrates the spiral winding configuration and suggests how anisotropic thermal conductivity should be taken into account in a macro-homogeneous thermal model of the jellyroll. The heat transfer is anisotropic because the current-collector layers within the jellyroll have much higher thermal diffusivity than the separator. Therefore, on a layer of the jellyroll normal to the *y* direction in Figure 5-2, heat conduction in the *y* direction will be apparently much slower than it is in the *xz* plane.

Note that Table 5-1 shows that two different thermal conductivity values were used in the *z* direction for the jellyroll, because of the complexity added by the jellyroll winding. Figure 5-3(a) shows that at the top and bottom of the jellyroll, there are small domains where the layers predominantly occupy the *xy* plane, *i.e.*, where the separator is normal to *z*. In these domains the thermal conductivity in the *z* direction was reduced to the same value in the *y* direction. A user-defined function was written and included in the Fluent code to implement this property variation. Note that the thermal conductivity tensor was assumed to be diagonal for simplicity.

Figure 5-4 shows local temperature distributions that arise within the LEV50 after 550s of discharge at a 4C rate (200 A), assuming (a) anisotropic and (b) isotropic thermal conductivity. (In the isotropic case, a uniformly high conductivity, k_z = 28 W/m-K, was used.) The battery was taken to be in initial equilibrium with an ambient temperature of 298 K; a heat-transfer coefficient of h = 40 W/m^2-K, corresponding to forced convection, was used on the outer boundary of the stainless-steel housing; the bottom of the housing was taken to be thermally insulated, as it is in many practical automotive batteries.

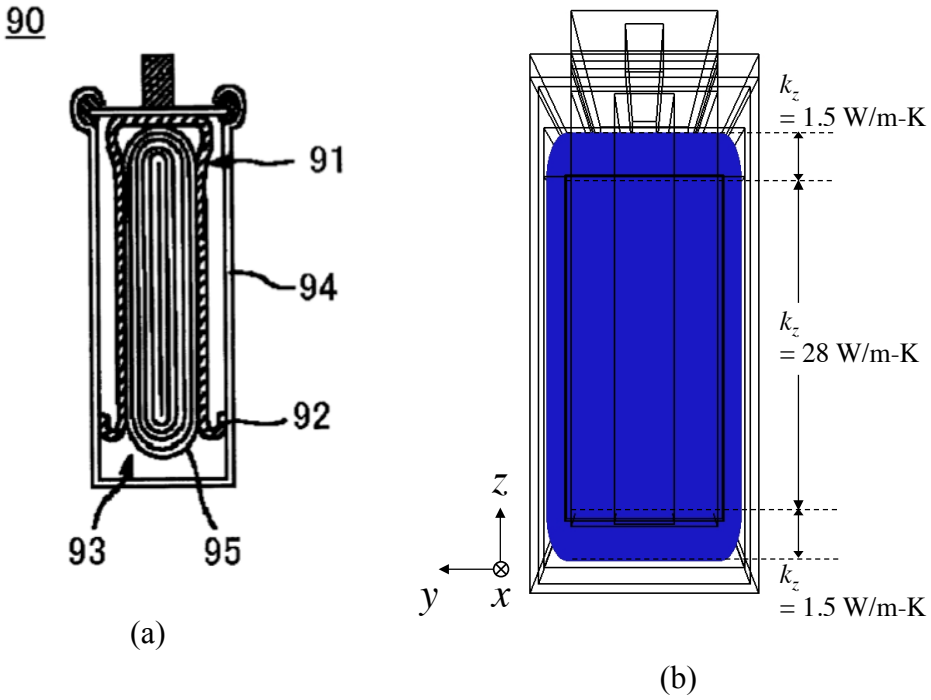

Figure 5-3 (a) An exemplary picture of jellyroll inside a battery; (b) distribution of non-uniform *z* direction thermal conductivity, implemented in the Fluent program. (a) is reproduced from reference 30.

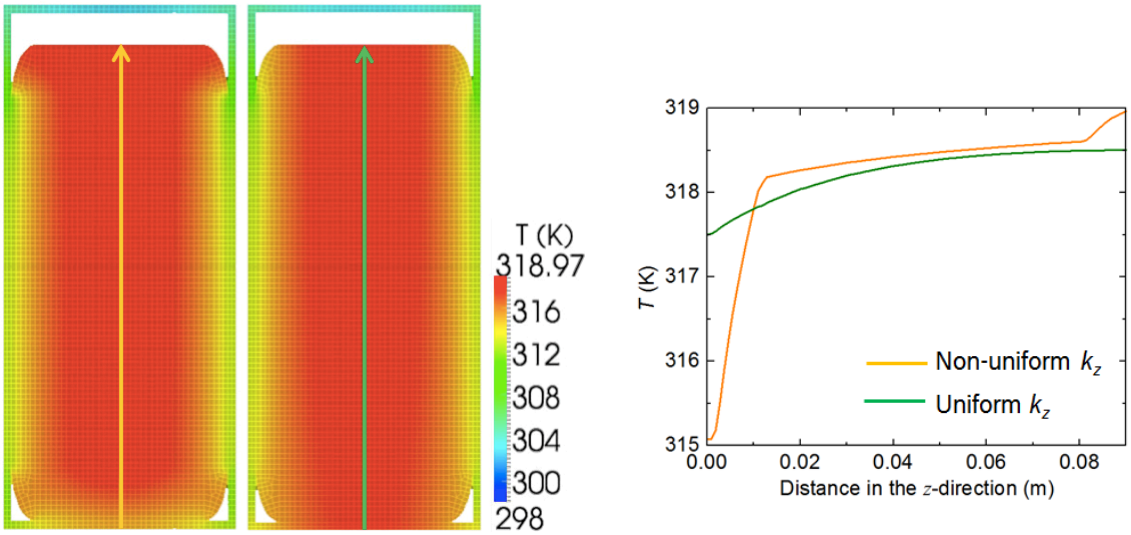

(a) (b) (c)

Figure 5-4 Low thermal conductivity at the top and bottom of the jellyroll affects on the local temperature distribution: (a) anisotropic thermal conductivity of Figure 5-3(b), (b) uniformly high thermal conductivity in the z direction, and (c) comparison of the temperature along the arrow in (a) and (b).

Figure 5-4(c) shows the centerline temperature in the z direction; the base of the centerline is located at the body-center point of the battery bottom plate (in the xy plane). One can see that lower thermal conductivity in the z direction at the top and bottom of the jellyroll leads to significant differences in the temperature distribution in the lower portion of the jellyroll. Both of the cases have thermally insulated boundary at the bottom, but the lower thermal conductivity results greater temperature gradient in the top and bottom region of the jellyroll. Lower thermal conductivity results in higher overall temperature and greater local temperature gradients. These facts are important because the local temperature and its gradients are critical to battery safety and cycle life.

5.3 Performance results

5.3.1 Thermal boundary conditions

The developed simulation tool was used to test the impact of local internal temperature on battery performance. First, the effects of different thermal boundary conditions on the internal temperature distribution within the battery cell were assessed. Four different boundary conditions were simulated with a 4 C discharge current (200 A) and initial uniform temperature of 298 K. (An insulating boundary condition at the bottom face of the battery housing was used in all cases.) Figure 5-5(a) shows four different temperature distributions that arise from different thermal boundary conditions on the battery housing and tabs. Cases 1 and 2 in Figure 5-5(a) use natural-convection boundary conditions on the battery housing, h = 8 W/m^2-K; cases 3 and 4 used forced

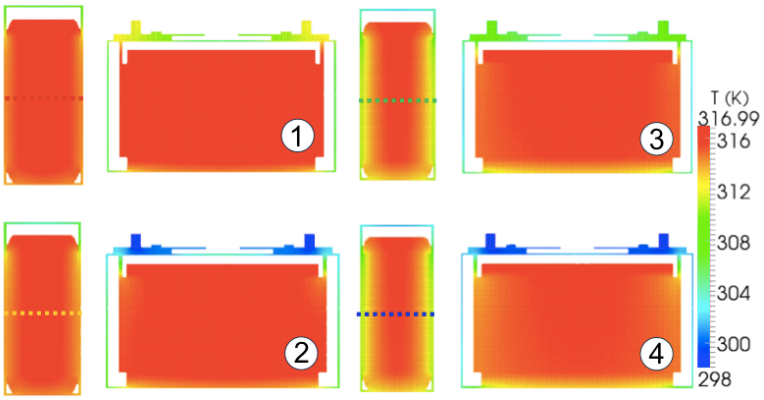

(a)

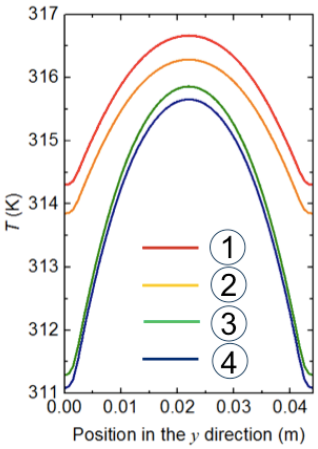

(b)

Figure 5-5 The effects of different boundary conditions on the local temperature distribution.

convection there, h = 40 W/m^2-K; cases 1 and 3 use thermal boundary conditions on the tabs that match the housing; cases 2 and 4 assume isothermal conditions (298 K) at the surfaces of the tabs. Conditions of constant tab temperature were tested because in practice, batteries are usually connected to large thermal masses maintained at ambient temperature (such as the vehicle being powered), to which heat is readily conducted through electrically conductive wiring.

A more detailed comparison can be made using Figure 5-5(b), which compares centerline temperature distributions from Figure 5-5(a). In line with physical expectations, natural convection (cases 1 and 2) results in higher peak and average temperature, whereas forced convection (cases 3 and 4) results in greater temperature gradients. In cases 2 and 4, the forced low temperature at the tabs induces much higher heat fluxes there, lowering the overall temperature relative to cases 1 and 3.

5.3.2 Local distribution of temperature

The evolution of temperature profiles within the jellyroll is illustrated in Figure 5-6, which shows several different instants after the start of a 4C (200 A) discharge. The simulation was stopped at t = 556 s, when a cell voltage of 3.0V was reached. Owing to the convection from the cell exterior, the temperature at the central part of the jellyroll was always significantly higher than its exterior surfaces. As time elapsed, the relative difference between maximum and minimum temperature in the jellyroll rose, eventually reaching about 9 °C at the end of the simulation.

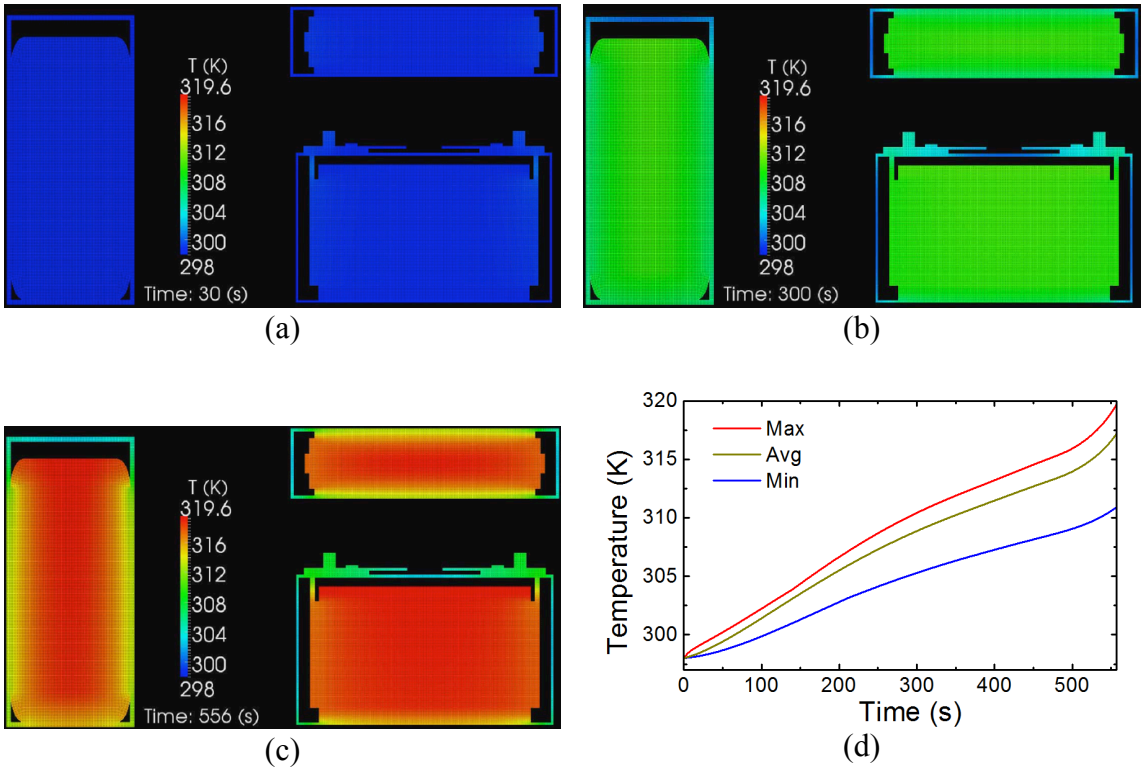

Figure 5-6 Non-uniform temperature distribution at three different instants during a constant-current discharge started in equilibrium with the ambient temperature: (a) 30s, (b) 300s, and (c) 556s; (d) maximum, minimum, and volume-average temperature of the jellyroll throughout the discharge duration.

5.3.3 Local distribution of the current density

The local transient distribution of current density shows more subtle features. Deviation of local current density from the average is illustrated in Figure 5-7. In general the upper central part of the jellyroll sustains higher current density than other parts; and, the outer part, close to the housing, has lower current density than average. Interestingly, the deviation from average current fluctuates significantly at fixed locations, as shown in Figure 5-7(d): in the time domains labeled 1, 3, and 5 on the figure, the deviation from the average current increases; it decreases in domains 2 and 4.

A possible explanation for the features of the transient current distribution is provided as follows. Increases in local temperature induce increases in local current density, because of the way the local electrochemical properties – diffusion coefficients, interfacial reaction rates, and conductivities – vary with local temperature. (The temperature dependence of the properties used in this simulation has been fairly well established from independent characterization efforts [31-36].) This increase in local current causes the local SOC in each electrode to vary significantly from its average; the natural response of the open-circuit potential (*i.e.*, equilibrium cell potential) is to fall in response to this SOC change, correspondingly reducing the overpotential driving discharge and decreasing the deviation of local current density. The overall mechanism is illustrated schematically in Figure 5-8.

Generally, the temperature of the central part of the jellyroll is higher than its outer side due to the outward heat flux from the casing into the surroundings. The mass diffusivity D, the reaction rate constant k, and the resistance of the solid electrolyte

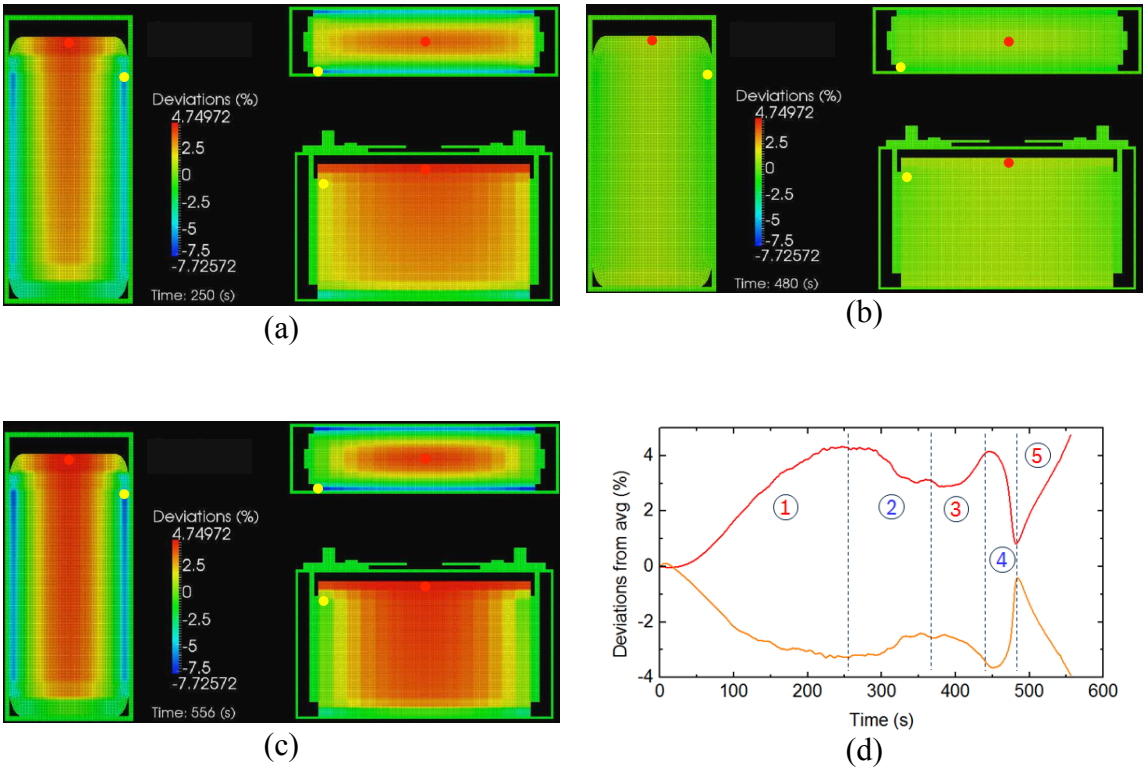

Figure 5-7 (a, b, c) Non-uniform electric current distribution at the three different instants shown in Figure 5-6; and (d) transient deviations from the average current at two distinct locations within the jellyroll; locations are marked with red and yellow circles in (a), (b), and (c).

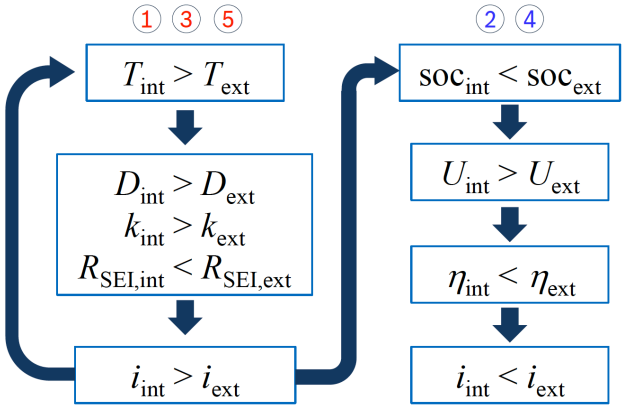

Figure 5-8 A suggested explanation for the fluctuating current distribution deviations. Subscripts ‘int’ and ‘ext’ indicate properties in the interior and exterior parts of the jellyroll, respectively.

interface (SEI) layers R_{SEI} in the jellyroll are sensitive to the temperature; these coefficients follow the Arrhenius law as follows:

$$D(T) = D^0 \exp\left(\overline{E_{a1}} \frac{T - T_{\text{ref}}}{T * T_{\text{ref}}}\right), \tag{5.1}$$

$$k(T) = k^0 \exp\left(\overline{E_{a2}} \frac{T - T_{\text{ref}}}{T * T_{\text{ref}}}\right), \tag{5.2}$$

$$R_{\text{SEI}}(T) = R_{\text{SEI}}^0 \exp\left(-\overline{E_{a3}} \frac{T - T_{\text{ref}}}{T * T_{\text{ref}}}\right), \tag{5.3}$$

where the superscript 0 demonstrates that the coefficient is at the reference state, $\overline{E_{aj}}$ are activation energies (different for each property), and T_{ref} is a reference temperature.

Experimental measurements show that higher temperature increases lithium diffusivity in liquid-electrolytes and solid intercalation materials [32], as well as increasing reaction rate constants at solid/electrolyte interfaces [33]; higher temperatures decrease the resistivities of the solid/electrolyte interphase (SEI) layers on porous-electrode surfaces [36]. Each of these dependences helps to reduce electrical (or mass-transfer) resistance as temperature increases. Since the resistance generally falls less than the square of the corresponding increased current, local increases in temperature also drive a feedback mechanism, where Joule heating due to current flow causes the temperature to further increase.

Another effect involves the thermodynamics of the cell reaction. Figure 5-9 (a) demonstrates the open-circuit potential (OCP) (*i.e.*, the equilibrium potential of the reaction) as a function of the SOC of the anode material, which is evaluated based on the

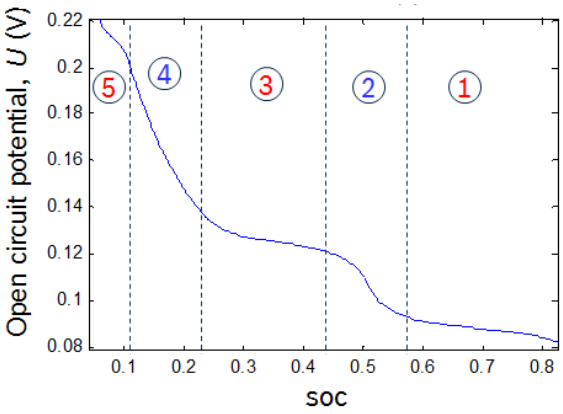

(a)

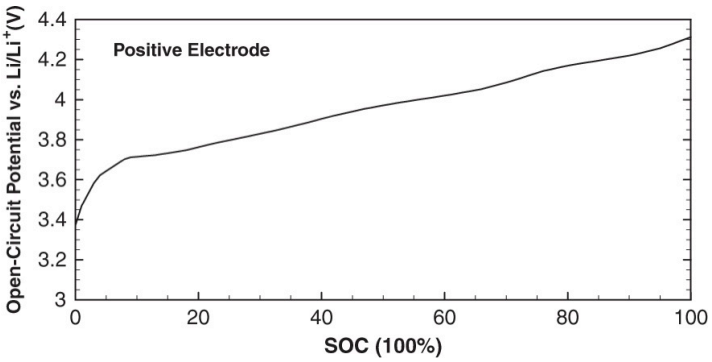

(b)

Figure 5-9 The open circuit potentials as a function of the state of charge (SOC) of the surface of anode particles (a) anode of graphite and (b) cathode of NMC. (b) is reproduced from reference 37. For anode (a), the regions 2 and 4 have relatively greater gradient then other regions; therefore the small SOC difference in the regions 2 and 4 results in the larger open circuit potential difference. For cathode (b), no significant gradient is observed between 10 ~ 100% SOC region.

local lithium content of and extent of concentration polarization within the solid. Regions 2 and 4 show greater changes in OCP than the other three regions; in these domains of the charge state, small differences in SOC will result in larger changes in open-circuit potential than they will in other regions. This changes the surface overpotential η, following $\eta = V - U$, where V is the applied voltage and U, the local OCP. Through the Butler-Volmer equation, η drives interfacial reactions faster, inducing higher local current density. Because of the smaller OCP gradients with respect to SOC, in regions 1, 3, and 5, the thermal effects on internal resistance dominate. One might think that the cathode has similar effects on OCP; however, Figure 5-9 (b) shows the OCP of the cathode used for our model, nickel-manganese-cobalt oxide (NMC). The OCP of NMC does not exhibit a significant change in gradient between 10 and 100% SOC [37]. Under 10% SOC, the change in NMC equilibrium potential might affect the overall OCV of the cell; such an effect would still support the argument in Figure 5-8.

5.4 Implications for battery safety

Local temperature and current distributions can provide information about failure mechanisms in automotive battery systems. Two key failure mechanisms are lithium-metal plating and thermal runaway. Tests pertinent to these safety issues were performed using the developed simulation tool.

5.4.1 The lithium plating side reaction

During charging, lithium ions ideally intercalate into the porous graphite negative electrode (typically called the anode, although it acts as a cathode during the charging

process). If the surface overpotential at the anode is near zero or negative, thermodynamics drive lithium metal to plate on the solid surface instead. As lithium plating continues, dendrites can form; dendrite propagation can cause internal short circuits and consequent catastrophic battery failure. The process of lithium plating on a porous graphite negative electrode has been imaged *in situ* by Harris *et al.* [38].

To examine lithium plating, a charge step at 4C from an initial state of 50% SOC was simulated with forced-thermal-convection boundary conditions on the battery housing and tabs, at four different ambient temperatures. Charging was stopped when the battery voltage reached a cutoff of 4.35 V. Figure 5-10(a) shows typical data at 20°C, which shows the outer area of the jellyroll to have the most negative overpotential. suggesting that more lithium plating is likely to occur there. Anode surface overpotentials that occur during 4C charging in ambient temperatures of 10 °C, 15 °C, 20 °C, and 25 °C are shown in Figure 5-10(b). Lower ambient temperature appears to increase the propensity for lithium plating at high current. All in all, lithium plating is more likely at the outer surface of the jellyroll, and could be severe in low-temperature ambients.

5.4.2 Thermal runaway

High ambient temperatures also lead to safety concerns. When a lithium-ion battery is exposed to a high enough temperature, the heating triggers a spontaneous exothermic chemical reaction, in a process typically called ‘thermal runaway’ [5]. Hatchard *et al*. modeled thermal runaway using a theoretical description of a proposed SEI decomposition reaction [39]. The reaction was hypothesized to proceed *via* two

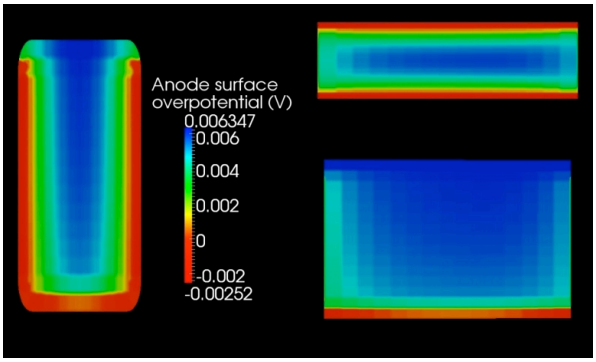

(a)

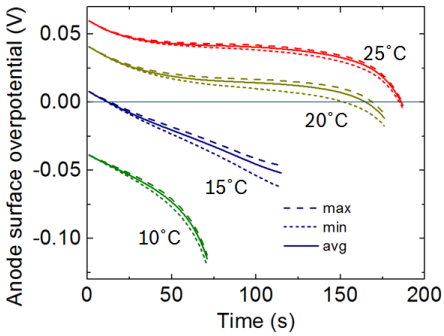

(b)

Figure 5-10 The local distribution of anodic surface overpotential. (a) A case of 4C recharge in a 20°C ambient shows that the outer area of the jellyroll has more Li plating after 160s. (b) Anode surface overpotentials with different ambient and initial temperatures demonstrate that lower ambient temperatures result in more Li plating.

steps: first, in the range 90–120°C, the metastable SEI phase reorganizes into a stable SEI film; second, around 150°C, anode-intercalated lithium reacts with the electrolyte to thicken the stable SEI film. Both reaction steps are highly exothermic, accompanied by a significant release of heat. To account for thermal runaway, a heat generation term was added to the energy balance that describes the Hatchard SEI thermal reorganization and growth mechanism. (See 5-B Appendix for the model equations.)

Figure 5-11 shows thermal runaway at four different ambient temperatures. In each simulation, the battery was initially equilibrated at 25°C, and the forced boundary condition was applied. The ambient temperatures are varied from 140 to 155°C. One can see that an ambient temperature of 140°C is too low to trigger the exothermic reaction; higher temperatures lead to faster thermal runaway with higher peak temperatures.

5.5 Conclusion

A simulation tool was created to investigate the impact of design changes on battery performance and thermal response of a commercial automotive cell (the GS-Yuasa LEV50 50 Ah NMC battery). For simulations, the standard Dualfoil model was coupled to a local energy balance to get transient temperature distributions within the battery. Simulations in three dimensions were necessary because of the complicated components within the battery; anisotropic heat conduction in the jellyroll was also taken into account. Using the simulation tool, various boundary conditions and initial conditions were tested to assess their impacts on battery performance. Higher cooling rates reduced the uniformity of the current density and temperature, as expected.

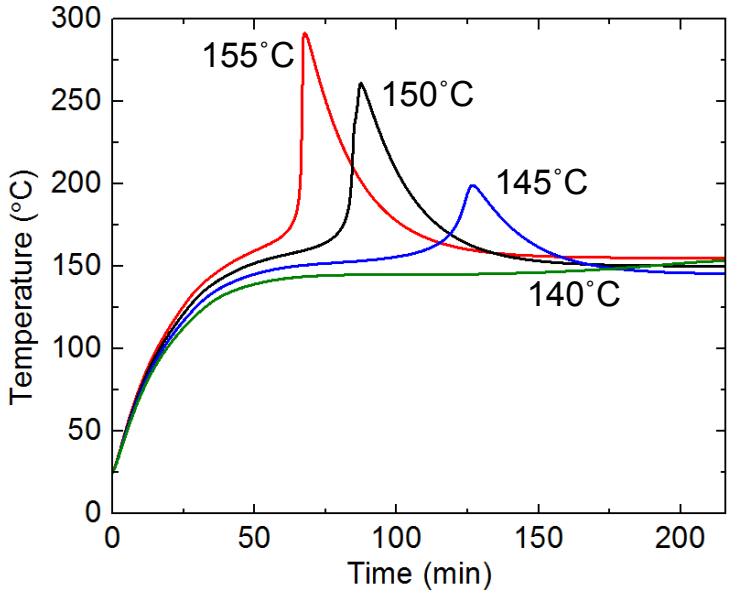

Figure 5-11 The thermal runaway simulation (oven test) at four different ambient temperatures.

Transient solutions of the local distributions of temperature and the electric current density were obtained. These showed the merits of the detailed electrochemical model, which rationalized swings in current homogeneity that occur due to temperature-dependence of local properties and variations in the local SOC. Extreme conditions were tested for thermal runaway as well, and the critical ambient temperature for triggering thermal runaway was found to be about 145°C.

5-A Appendix: Dualfoil [1-3,21,22]

Mass balance: ion transport in the electrolyte

$$\varepsilon \frac{\partial c}{\partial t} = \nabla \cdot \left(D_{eff} \nabla c + \frac{i_2 \left(1 - t_+\right)}{F} \right)$$

Mass balance: Li transport in the active material

$$\frac{\partial c}{\partial t} = \nabla \cdot \left(D \nabla c \right)$$

Charge balance: distribution of ionic/electronic current

$$a j_{i,n} = \frac{-s_i}{nF} \nabla \cdot i_2$$

Ohm's law: ionic current in the electrolyte

$$i_2 = -\kappa \nabla \Phi_2 + 2\frac{\kappa RT}{F}\left(1 - t_+\right)\left(1 + \frac{\partial \ln f_{+-}}{\partial \ln c}\right)\nabla \ln c$$

Ohm's law: electric current in the solid matrix

$$I - i_2 = -\sigma \nabla \Phi_1$$

Butler-Volmer equation: electrochemical reaction rates

$$j_{i,n} = \frac{-s_i}{nF} i_0 \left[\exp\left(\frac{\alpha_a F}{RT} \eta_s \right) - \exp\left(-\frac{\alpha_c F}{RT} \eta_s \right) \right]$$

Tafel equation: cathodic side reaction rate

$$i_{\text{side}} = -i_0 \exp\left(-\frac{\alpha_c F}{RT} \eta_s \right)$$

Heat generation rate: based on local reaction rate, SOC

$$\dot{q} = -\int_V \sum_k a i_{n,k} U_{H,k} dv - IV$$

5-B Appendix: thermal abuse model [39]

Heat balance:

$$\frac{\partial(\rho c_p T)}{\partial t} = -\nabla(k \nabla T) + S_{abuse},$$
$$S_{abuse} = S_{sei} + S_{ne} + S_{pe}$$

SEI Reaction (metastable to stable SEI):

$$\Delta x_f = -A_1 x_f^n \exp\left(\frac{-E_1}{K_b T} \right) \Delta t$$

, where x_f is the amount of lithium-containing metastable species in SEI.

Negative solvent reaction

$$\Delta x_i = -A_2 x_i \exp\left(\frac{-z}{z_0} \right) \exp\left(\frac{-E_2}{K_b T} \right) \Delta t$$

$$\Delta z = A_2 x_i \exp\left(\frac{-z}{z_0} \right) \exp\left(\frac{-E_2}{K_b T} \right) \Delta t$$

, where x_i is the amount of lithium intercalated within carbon, and z is the dimensionless measure of SEI thickness.

Positive solvent reaction

$$\Delta\alpha = A\exp\left(\frac{-E}{K_b T}\right)\alpha^m(1-\alpha)^n[-\ln(1-\alpha)]^p \ \Delta t$$

, where $\Delta\alpha$ is the fractional degree of conversion of cathode.

Heat generation

$$S_{pe} = HWA\exp\left(\frac{-E}{K_b T}\right)\alpha^m(1-\alpha)^n[-\ln(1-\alpha)]^p$$

$$S_{sei} + S_{ne} = H_1 W_1 A_1 x_f^n \exp\left(\frac{-E_1}{K_b T}\right) + H_2 W_2 A_2 x_i \exp\left(\frac{-z}{z_0}\right)\exp\left(\frac{-E_2}{K_b T}\right)$$

5.6 References

[1] M. Doyle, T. F. Fuller, and J. Newman, "Modeling of Galvanostatic Charge and Discharge of the Lithium/Polymer/Insertion Cell," *J. Electrochem. Soc.*, vol. 140, no. 6, pp. 1526–1533, Jun. 1993.

[2] T. F. Fuller, M. Doyle, and J. Newman, "Relaxation Phenomena in Lithium-Ion-Insertion Cells," *J. Electrochem. Soc.*, vol. 141, no. 4, pp. 982–990, Apr. 1994.

[3] T. F. Fuller, M. Doyle, and J. Newman, "Simulation and Optimization of the Dual Lithium Ion Insertion Cell," *J. Electrochem. Soc.*, vol. 141, no. 1, pp. 1–10, Jan. 1994.

[4] J. S. Newman and C. W. Tobias, "Theoretical Analysis of Current Distribution in Porous Electrodes," *J. Electrochem. Soc.*, vol. 109, no. 12, p. 1183, 1962.

[5] T. M. Bandhauer, S. Garimella, and T. F. Fuller, "A Critical Review of Thermal Issues in Lithium-Ion Batteries," *Journal of The Electrochemical Society*, vol. 158, no. 3, p. R1, 2011.

[6] M. Fleckenstein, O. Bohlen, M. A. Roscher, and B. Bäker, "Current density and state of charge inhomogeneities in Li-ion battery cells with LiFePO4 as cathode material due to temperature gradients," *Journal of Power Sources*, vol. 196, no. 10, pp. 4769–4778, May 2011.

[7] P. Ramadass, B. Haran, R. White, and B. N. Popov, "Capacity fade of Sony 18650 cells cycled at elevated temperatures: Part I. Cycling performance," *Journal of Power Sources*, vol. 112, no. 2, pp. 606–613, Nov. 2002.

[8] P. Ramadass, B. Haran, R. White, and B. N. Popov, "Mathematical modeling of the capacity fade of Li-ion cells," *Journal of Power Sources*, vol. 123, no. 2, pp. 230–240, Sep. 2003.

[9] P. Liu, J. Wang, J. Hicks-Garner, E. Sherman, S. Soukiazian, M. Verbrugge, H. Tataria, J. Musser, and P. Finamore, "Aging Mechanisms of LiFePO4 Batteries Deduced

by Electrochemical and Structural Analyses," *J. Electrochem. Soc.*, vol. 157, no. 4, pp. A499–A507, Apr. 2010.
[10] E. V. Thomas, H. L. Case, D. H. Doughty, R. G. Jungst, G. Nagasubramanian, and E. P. Roth, "Accelerated power degradation of Li-ion cells," Journal of Power Sources, vol. 124, no. 1, pp. 254–260, Oct. 2003.
[11] K. Amine, J. Liu, and I. Belharouak, "High-temperature storage and cycling of C-LiFePO4/graphite Li-ion cells," *Electrochemistry Communications*, vol. 7, no. 7, pp. 669–673, Jul. 2005.
[12] J. R. Belt, C. D. Ho, T. J. Miller, M. A. Habib, and T. Q. Duong, "The effect of temperature on capacity and power in cycled lithium ion batteries," *Journal of Power Sources*, vol. 142, no. 1–2, pp. 354–360, Mar. 2005.
[13] J. R. Belt, C. D. Ho, C. G. Motloch, T. J. Miller, and T. Q. Duong, "A capacity and power fade study of Li-ion cells during life cycle testing," *Journal of Power Sources*, vol. 123, no. 2, pp. 241–246, Sep. 2003.
[14] I. Bloom, S. A. Jones, V. S. Battaglia, G. L. Henriksen, J. P. Christophersen, R. B. Wright, C. D. Ho, J. R. Belt, and C. G. Motloch, "Effect of cathode composition on capacity fade, impedance rise and power fade in high-power, lithium-ion cells," *Journal of Power Sources*, vol. 124, no. 2, pp. 538–550, Nov. 2003.
[15] R. Wright, C. Motloch, J. Belt, J. Christophersen, C. Ho, R. Richardson, I. Bloom, S. Jones, V. Battaglia, G. Henriksen, T. Unkelhaeuser, D. Ingersoll, H. Case, S. Rogers, and R. Sutula, "Calendar- and cycle-life studies of advanced technology development program generation 1 lithium-ion batteries," Journal of Power Sources, vol. 110, no. 2, pp. 445–470, Aug. 2002.
[16] S. Peck and M. Pierce, "Development of a Temperature-Dependent Li-ion Battery Thermal Model," SAE International, Warrendale, PA, 2012-01-0117, Apr. 2012.
[17] U. S. Kim, J. Yi, C. B. Shin, T. Han, and S. Park, "Modeling the Dependence of the Discharge Behavior of a Lithium-Ion Battery on the Environmental Temperature," *J. Electrochem. Soc.*, vol. 158, no. 5, pp. A611–A618, May 2011.
[18] E. Barsoukov, J. H. Kim, C. O. Yoon, and H. Lee, "Universal battery parameterization to yield a non-linear equivalent circuit valid for battery simulation at arbitrary load," *J. Power Sources*, vol. 83, no. 1–2, pp. 61–70, Oct. 1999.
[19] M. W. Verbrugge and R. S. Conell, "Electrochemical and Thermal Characterization of Battery Modules Commensurate with Electric Vehicle Integration," *J. Electrochem. Soc.*, vol. 149, no. 1, pp. A45–A53, 2002.
[20] J. Christensen, P. Albertus, and D. Cook, "3D Thermoelectrochemical model of a Li-ion model" *AABC (Adv. Automotive Batt. Conf.)* Jan 24th, 2011.
[21] J. Christensen, P. Albertus, and D. Cook, "3D Thermoelectrochemical model of a Li-ion model" JECS, 2013. (*In preparation*)
[22] D. Bernardi, E. Pawlikowski, and J. Newman, "A General Energy Balance for Battery Systems," J. Electrochem. Soc., vol. 132, no. 1, pp. 5–12, Jan. 1985.
[23] M. M. Thackeray, C. Wolverton, and E. D. Isaacs, "Electrical energy storage for transportation—approaching the limits of, and going beyond, lithium-ion batteries," Energy Environ. Sci., vol. 5, no. 7, pp. 7854–7863, Jun. 2012.
[24] http://www.gs-yuasa.com/us/; http://lithiumenergy.jp/en/products/index.html (last visited Aug. 15, 2013)
[25] http://www.ansys.com (last visited Aug. 15, 2013)

[26] B. J. McBride, S. Gordon, and M. A. Reno. Coefficients for Calculating Thermodynamic and Transport Properties of Individual Species. NASA TM-4513, October 1993.
[27] J. W. Rose and J. R. Cooper, editors. Technical Data on Fuels. Wiley, 7th ed, 1977.
[28] W. C. Reynolds. Thermodynamic Properties in SI: Graphs, Tables, and Computational Equations for 40 Substances. Department of Mechanical Engineering, Stanford University, 1979.
[29] H. Maleki, S. A. Hallaj, J. R. Selman, R. B. Dinwiddie, and H. Wang, "Thermal Properties of Lithium-Ion Battery and Components," *J. Electrochem. Soc.*, vol. 146, no. 3, pp. 947–954, Mar. 1999.
[30] K. Nansaka and Y. Yamauchi, "Prismatic battery," US8216715 B210-Jul-2012.
[31] A. Parthasarathy, S. Srinivasan, A. J. Appleby, and C. R. Martin, "Temperature Dependence of the Electrode Kinetics of Oxygen Reduction at the Platinum/Nafion® Interface—A Microelectrode Investigation," J. Electrochem. Soc., vol. 139, no. 9, pp. 2530–2537, Sep. 1992.
[32] S. Takai, M. Kamata, S. Fujine, K. Yoneda, K. Kanda, and T. Esaka, "Diffusion coefficient measurement of lithium ion in sintered Li1.33Ti1.67O4 by means of neutron radiography," Solid State Ionics, vol. 123, no. 1–4, pp. 165–172, Aug. 1999.
[33] Meibuhr, S. G., "Electrode Studies in Nonaqueous Electrolytes: I. The Lithium Electrode in LiC10-Propylene Carbonate Solutions," J. Electrochem. SOC., 117, 56 (1970).
[34] Meibuhr, S. G., "Electrode Studies in Nonaqueous Electrolytes: 11. Anion Effect on the Kinetics of Li/Li+ in Propylene Carbonate," J. Electrochem. SOC., 118, 1320 (1971).
[35] Dudley, J. T., D. P. Wilkinsozn, G. Thomas, R. LeVae, S. Woo, H. Bolm, C. Horvath, M. W. Juzkow, B. Denis, P. Juric, P. Aghakian, and J. R. Dahn, "Conductivities of Electrolytes for Rechargeable Lithium Batteries," J. Power Sources, 35, 59 (1991).
[36] A. V. Churikov, "Transfer mechanism in solid-electrolyte layers on lithium: influence of temperature and polarization," Electrochimica Acta, vol. 46, no. 15, pp. 2415–2426, Apr. 2001.
[37] W. Fang, O. J. Kwon, and C.-Y. Wang, "Electrochemical–thermal modeling of automotive Li-ion batteries and experimental validation using a three-electrode cell," International Journal of Energy Research, vol. 34, no. 2, pp. 107–115, 2010.
[38]S. J. Harris, A. Timmons, D. R. Baker, and C. Monroe, "Direct in situ measurements of Li transport in Li-ion battery negative electrodes," Chemical Physics Letters, vol. 485, no. 4–6, pp. 265–274, Jan. 2010.
[39] T. D. Hatchard, D. D. MacNeil, A. Basu, and J. R. Dahn, "Thermal Model of Cylindrical and Prismatic Lithium-Ion Cells," *J. Electrochem. Soc.*, vol. 148, no. 7, p. A755, 2001.

Appendix A. High-accuracy calculations of sixteen collision integrals for Lennard-Jones (12–6) gases and their use to parameterize neon, argon, and krypton

Chapter 2 demonstrated a strong motivation to research how transport properties can be estimated using kinetic theory. Even for the simple experiment described there, a detailed multi-component transport analysis in principle requires more than ten binary diffusion coefficients (because of the complicated composition of air), including experimentally unavailable properties like $\mathscr{D}_{\text{acetone-methanol}}$. In addition, even if air was treated as a homogeneous substance, the best-fitting $\mathscr{D}_{\text{acetone-methanol}}$ was found to be four times smaller than Carty and Schrodt's value calculated using Lennard-Jones parameters.

In this appendix, we develop a method to evaluate collision integrals, which are kinetic properties needed in the estimation of transport properties. We show conclusively that through Chapman-Enskog kinetic theory, a Lennard-Jones (12–6) potential can be used to predict the temperature dependence of continuum transport properties (viscosity, thermal conductivity, and self-diffusivity) for several dilute monatomic gases within the accuracy limits established by experiments, while simultaneously matching the temperature dependence of thermodynamic data (the second virial coefficient). To provide this conclusion we develop arbitrary-precision algorithms to compute collision integrals; these high-accuracy calculations are then used to create interpolation formulas that allow very rapid collision-integral computation. The fast collision-integral interpolations we develop make tractable the inverse problem of multi-objective pair-

potential parameterization. Ultimately, we show the Lennard-Jones (12–6) potential suffices to match all reliable experimental data for Ne, Ar, and Kr from temperatures of boiling points up to 2000K (the first demonstration of its kind), as well as providing the most accurate Lennard-Jones parameters to date for these three gases.

Although this work focuses on three noble gases, it could be extended to polar gases such as acetone and methanol, used for Carty and Schrodt's expeirments reported in chapter 2. In that case, a different intermolecular potential may be necessary. Expansion of the current work to the polar-gas properties would be interesting. This work provides the groundwork for future study of more complicated intermolecular potential functions.

A.1 Introduction

As shown in Chapter 2, accurate transport properties are crucial for the simulation of processes involving continuum-scale momentum, heat, or mass transfer. Gas viscosities, thermal conductivities, and diffusivities, for example, are needed in the design of chemical reactors, and also play an important role in atmospheric chemistry, combustion science, and aerothermodynamics [1, 2]. Direct measurements of all the properties of a gas over a wide temperature range are usually impractical, so there is a need for reliable methods of property estimation [2].

Kinetic theory, as implemented through the analysis of Boltzmann's gas equation [3], provides a well-established method to calculate macroscopic transport coefficients. Conventional wisdom has it that the theory can achieve temperature-dependent properties

of dilute nonpolar gases with fair agreement [4]. This chapter shows that kinetic-theory predictions can be made to fall within the bounds of intrinsic error in property-measurement experiments. High-precision algorithms are developed to compute properties, and a method to parameterize potentials is introduced.

Gressman and Strain proved the global existence of stable solutions to the Boltzmann equation in 2010 [5]. This recent result emphasizes that the perturbation approach developed independently by Chapman and Enskog a century ago [6-8] is a physically sound method by which to compute properties for use in continuum transport models. Chapman-Enskog theory treats a gas fluctuating near equilibrium as an average representation of its ensemble of two-particle encounters. Perturbation of Boltzmann's equation yields transport coefficients as algebraic functions of reduced collision integrals $\Omega^{(l,s)\star}$, which essentially quantify moments of the mean free path. The indices l and s are integer parameters that arise during analysis of a dynamic perturbation of the equilibrium state according to the Chapman-Enskog procedure [9, 10].

Collision integrals in dilute gases depend only on the reduced temperature $T^* = k_B T / \epsilon$, where k_B is Boltzmann's constant, T the absolute temperature, and ϵ a characteristic two particle interaction energy. Thus $\Omega^{(l,s)\star}$ values are amenable to tabulation—in principle. Several well-known computational difficulties are barriers to numerical analysis: divergences, discontinuities, and rapid oscillations occur in several of the functions from which collision integrals derive [1]. Because of the high computational cost and analytical complexity of their calculation, collision integrals are usually retrieved from tables, rather than being computed on the fly, despite the facts that procedures for interpolation between temperatures are not definitively established, and

that published tables may summarize inaccurate calculations.

In an early effort to speed computation, Hattikudur and Thodos [11] applied nonlinear least-squares methods to fit existing collision-integral tables for the Lennard-Jones (LJ) potential [12, 13]. Their interpolations compute $\Omega^{(1,1)\star}$ and $\Omega^{(2,2)\star}$ for LJ (12–6) gases from $0.3 \le T^* \le 400$ matching the original tables of Hirschfelder et al. [9] within 1%. The Hattikudur-Thodos equations suffice only to compute thermal conductivity and viscosity to first order in the Sonine expansion, and should be avoided because the tables on which they are based contain significant numerical error: Akhmatskaya and Pozhar proved that the underlying tables have error nowhere less than 0.1%, and more than 1% for $T^* < 1$ [14]; approximations used by Hirschfelder et al. have also been shown to cause inaccuracy at high temperatures [16].

Neufeld, Janzen, and Aziz (NJA) provided interpolation formulas for sixteen LJ (12–6) collision integrals—allowing viscosity, thermal conductivity, self-diffusion coefficient, and thermal diffusivity computations to third order—for $0.3 \le T^* \le 100$ [16]. A database precise to 0.05%, computed with O'Hara and Smith's algorithm [17], underpins the formulas. Some higher-order integrals rely on a recursion relation with intrinsic ~ 2% error [18]. Overall the NJA formulas are precise to one or two digits at most.

This chapter uses the topology of two-particle interaction trajectories to inform accurate collision integral computation. By leveraging the knowledge of trajectory shapes, collision cross-sections are computed with unprecedented precision. Very accurate empirical interpolation formulas are also developed, which allow the transport properties of LJ (12–6) gases to be calculated up to relatively high orders of approximation.

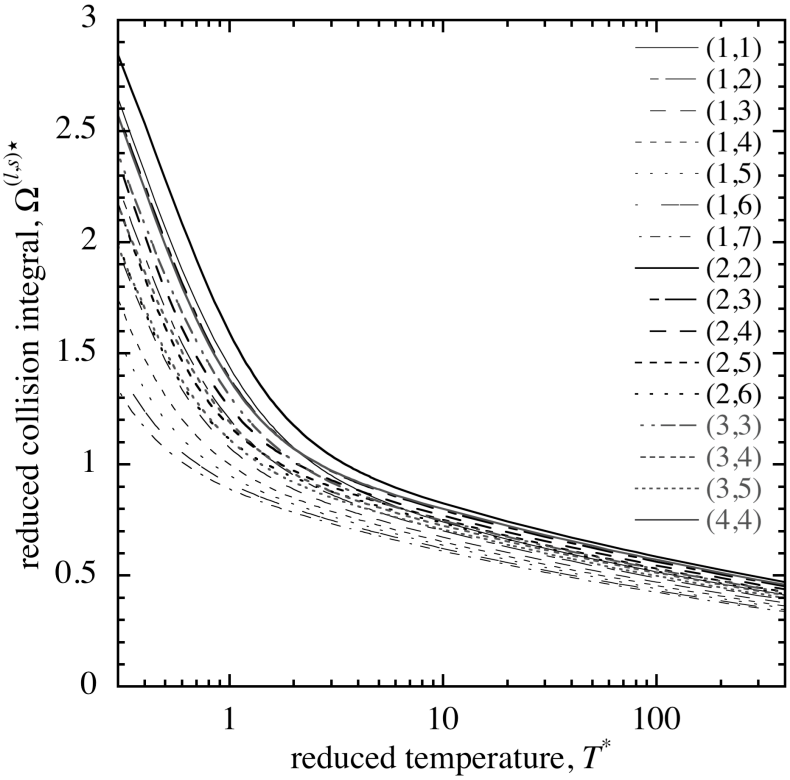

Figure A-1 Reduced collision integrals for Lennard-Jones (12–6) gases, computed using the methods developed in chapter 0.

This chapter closes by applying the new interpolation formulas to solve the inverse problem of optimal potential parameterization. Three noble gases are analyzed. Previous disagreements between LJ theory and experiments are ultimately resolved by the implementation of fast, precise collision-integral calculation. For dilute neon, argon, and krypton, the LJ potential model predicts viscosity, self-diffusion coefficient, thermal conductivity, and second virial coefficient within experimental error, from their boiling points up to extremely high temperatures.

A.2 Collision-integral interpolation

Since it provides a basis for putting this work to broader practical use, we first present empirical interpolation formulas for reduced LJ (12–6) collision integrals, which take the form

$$\Omega^{(l,s)\star} = A^{(l,s)} + \sum_{k=1}^{6}\left[B_k^{(l,s)} \Big/ \left(T^*\right)^k + C_k^{(l,s)} \left(\ln T^*\right)^k\right]. \qquad (1)$$

Figure A-1 demonstrates that this functionality reasonably approximates the first sixteen most useful collision integrals, which all decrease with rising T^* according to the form of the summand. Table A-1 summarizes the error of equation (1) relative to the high-precision tables on which it is based. For $0.3 \le T^* \le 400$, the average error is always less than 0.0011% and the maximum error less than 0.0069%; equation (1) yields collision integrals accurate to at least four significant digits throughout this temperature range.

Table A-1. Average and maximum deviations from high-precision tables for the interpolation formulas in equation (1).

(l, s)	Average deviation (%)	Max deviation (%)
(1,1)	0.00099	0.0051 at $T^* = 300$
(1,2)	0.00041	0.0025 at $T^* = 0.55$
(1,3)	0.00031	0.0011 at $T^* = 400$
(1,4)	0.00022	0.00093 at $T^* = 0.8$
(1,5)	0.00020	0.00095 at $T^* = 0.7$
(1,6)	0.00025	0.00099 at $T^* = 0.7$
(1,7)	0.00023	0.00099 at $T^* = 0.6$
(2,2)	0.0011	0.0071 at $T^* = 300$
(2,3)	0.00063	0.0030 at $T^* = 200$
(2,4)	0.00035	0.0018 at $T^* = 200$
(2,5)	0.00022	0.0012 at $T^* = 0.5$
(2,6)	0.00024	0.00085 at $T^* = 0.85$
(3,3)	0.00037	0.0021 at $T^* = 0.45$
(3,4)	0.00054	0.0033 at $T^* = 200$
(3,5)	0.00038	0.0020 at $T^* = 200$
(4,4)	0.00041	0.0029 at $T^* = 200$

Table A-2. Coefficients for equation (1), which predicts collision integrals within 0.007% in the range $0.3 \le T^* \le 400$.

(l, s)	A	B_1	C_1	B_2	$C_2 \times 10$	$B_3 \times 10$	$C_3 \times 10$
(1,1)	−1.1036729	2.6431984	1.6690746	0.0060432255	−6.9145890	−1.5158773	1.5502132
(1,2)	1.3555554	−0.44668594	−0.47499422	0.42734391	1.4482036	−1.6036459	−0.32158368
(1,3)	1.0677115	−0.13945390	−0.25258689	0.17696362	0.59709197	−0.26252211	−0.13332695
(1,4)	0.80959899	0.12938170	−0.045055948	0.059760309	−0.22642753	0.071109469	0.056672308
(1,5)	0.74128322	0.17788850	0.0013668724	0.027398438	−0.41730962	0.076254248	0.10378923
(1,6)	0.80998324	0.073071217	−0.071180849	0.034607908	−0.12738119	−0.011457199	0.038582834
(1,7)	0.81808091	0.044232851	−0.089417548	0.029750283	−0.051856424	−0.022011682	0.021882143
(2,2)	−0.92032979	2.3508044	1.6330213	0.50110649	−6.9795156	−4.7193769	1.6096572
(2,3)	2.5955799	−1.8569443	−1.4586197	0.96985775	5.2947262	−3.9888526	−1.1946363
(2,4)	1.6042745	−0.67406115	−0.62774499	0.42671907	2.0700644	−1.0177069	−0.47601690
(2,5)	0.82064641	0.23195128	0.039184885	0.12233793	−0.57316906	0.13891578	0.12794497
(2,6)	0.79413652	0.23766123	0.050470266	0.077125802	−0.62621672	0.13060901	0.14326724
(3,3)	1.2630491	−0.36104243	−0.33227158	0.68116214	0.79723851	−3.6401583	−0.15470355
(3,4)	2.2114636	−1.4743107	−1.1942554	0.64918549	4.3000688	−2.4075196	−0.97525871
(3,5)	1.5049809	−0.64335529	−0.60014514	0.3261704	1.9764859	−0.82126072	−0.45212434
(4,4)	2.6222393	−1.9158462	−1.4676253	1.0166380	5.3048161	−4.3355278	−1.1909781

(l, s)	$B_4 \times 10$	$C_4 \times 10^2$	$B_5 \times 10^2$	$C_5 \times 10^3$	$B_6 \times 10^3$	$C_6 \times 10^4$
(1,1)	0.54237938	−2.0642189	−0.90468682	1.5402077	0.61742007	−0.49729535
(1,2)	0.31461648	0.44357933	−0.32587575	−0.34138118	0.13860257	0.11259742
(1,3)	−0.043814141	0.19619285	0.16752100	−0.16063076	−0.14382801	0.055804557
(1,4)	−0.063851124	−0.065708760	0.10498938	0.040733113	−0.058149257	−0.010820157
(1,5)	−0.031650182	−0.13492954	0.032786518	0.096963599	−0.0092890016	−0.030307552
(1,6)	0.0028198596	−0.047060425	−0.020060540	0.030466929	0.021446483	−0.0085305576
(1,7)	0.0063264120	−0.024874471	−0.017555530	0.013745859	0.014255704	−0.0030285365
(2,2)	1.5806367	−2.2109440	−2.6367184	1.7031434	1.8120118	−0.56699986
(2,3)	0.90063692	1.6264589	−1.0918991	−1.2354315	0.56646797	0.40366357
(2,4)	0.0061857136	0.67153792	0.31225358	−0.52706167	−0.35206051	0.17705708
(2,5)	−0.20903423	−0.15336449	0.46715462	0.10241454	−0.35204303	−0.029975563
(2,6)	−0.10982362	−0.17806541	0.18034505	0.12353365	−0.095982571	−0.037501381
(3,3)	1.0500196	0.18686705	−1.6400134	−0.12179945	1.0880886	0.032594587
(3,4)	0.51820149	1.3399366	−0.60565396	−1.0283777	0.29812326	0.33956674
(3,5)	0.059682011	0.63650284	0.10269488	−0.49991689	−0.15957252	0.16833944
(4,4)	1.0496591	1.6123847	−1.3951104	−1.2174905	0.80048534	0.39545100

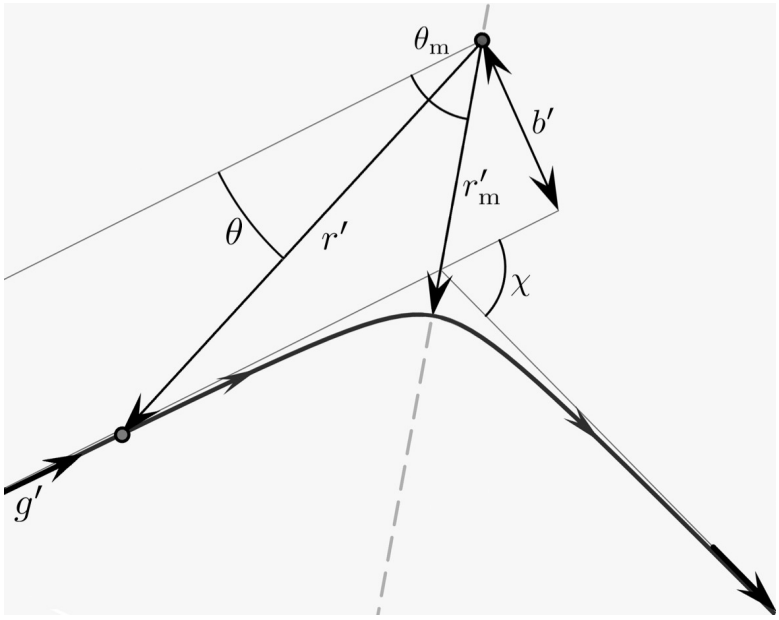

Figure A-2. Schematic of a binary encounter, characterized by the trajectory $r'(\theta)$. The initial relative particle speed g' and impact parameter b' determine the deflection angle χ.

Values of the coefficients in equation (1) are given in Table A-2 for the sixteen combinations of *l* and *s* shown on Figure A-1. Coefficients were determined by applying an optimization procedure based on the method of least squares [19] to a database of collision-integral tables, which was produced with the high-precision computational procedures discussed in chapter 0.

Unlike the NJA fit, equation (1) has a series form wherein coefficients generally decrease in magnitude as their order rises. One might think that adding terms to the sum would reduce deviations from the data tables on which it is based, but use of more than six terms in the series was found to increase truncation error overall when the coefficients were truncated after their eighth significant digit (as in Table A-2). Note also that the NJA parameterization was designed for accuracy within the range $0.3 \le T^* \le 100$; in contrast, equation (1) is designed for accuracy up to reduced temperatures of 400.

A.3 Precise collision-integral calculation

A.3.1 Description of encounters

Chapman-Enskog theory hinges on a detailed description of individual two-particle encounters, which are modeled with Newtonian dynamics. Several researchers have embedded quantum effects into kinetic theory [20–22], but quantum corrections tend to contribute negligibly to collision integrals [21]. Classical physics is employed here.

A representative classical binary encounter is sketched schematically in Figure A-2. Encounters are treated in a polar coordinate system (r', θ) centered on one particle (which

we call the 'incident particle'), in the plane established by the two particle velocities, with $\theta = 0$ aligned parallel to the direction of the relative velocity of the other particle (called the 'incoming particle'). (This perspective is equivalent to the center-of-mass coordinates used by Grad [10, 23]; here we follow the particle-center convention used by Chapman and Cowling [7, 8] and Hirschfelder *et al*. [9, 24-26]) Collision trajectories $r'(\theta)$ depend on the initial relative particle speed g', as well as the impact parameter b', which represents the distance of closest approach that would be achieved if the two particles did not exert any forces on each other during the encounter.

The energetics of particle interactions depend on a pair potential ϕ', which always has some repulsive character, and usually also has some attractive character. For a pair of similar particles, the trajectory during an encounter conserves angular momentum and energy, according to

$$mb'g' = mr'^2 \frac{d\theta}{dt}, \tag{2}$$

$$\frac{1}{2}mg'^2 = \frac{1}{2}m\left[\left(\frac{dr'}{dt}\right)^2 + r'^2\left(\frac{d\theta}{dt}\right)^2\right] + \phi'(r') \tag{3}$$

where t is time and m is the particle mass. The potential function thus establishes how g' and b' determine the angle χ by which the relative velocity deflects during an encounter.

The character of an encounter trajectory ultimately depends on the functionality of the pair potential. Chapman and Cowling [7, 8] used a hard-sphere potential to determine coefficients of viscosity, thermal conductivity, and self-diffusion. The accuracy of these transport coefficients was limited by the failure to account for interparticle attraction. Diffusivities computed for hard-sphere gases generally exceed experimental values by ~10-15% at moderate temperatures [27].

Kihara and Kotani,[28, 29] Hirschfelder et al., [9, 24–26] and Rowlinson[30] concurrently reported transport coefficients based on the LJ (12–6) interaction potential[12, 13]

$$\phi'(r') = 4\varepsilon\left[\left(\frac{\sigma}{r'}\right)^{12} - \left(\frac{\sigma}{r'}\right)^{6}\right]. \tag{4}$$

Here σ is the distance at which the potential crosses zero (it reaches a minimum at $r'/\sigma = \sqrt[6]{2} \approx 1.12$), and the characteristic energy ε quantifies the depth of the potential well. The term 'LJ parameters' will be used here to refer to the characteristic temperature ε/k_B and characteristic distance σ. Unlike the hard-sphere model, the LJ (12–6) potential accounts for interparticle attraction, whose sixth-order decay is suggested by quantum-mechanical analysis of non-polar, neutral atoms with spherically symmetric electron shells [31–33]; mathematical convenience is afforded by choosing a twelfth-order repulsive term [9]. When potentials involve both attraction and repulsion, the evaluations of collision integrals are complicated, because they must account for orbiting and spiraling trajectories [1], which will be a key focus here.

To determine trajectories during a binary encounter it is standard to obtain a time-independent expression of the angle θ by eliminating *dt* between Equations (2) and (3); after substitution of ϕ' from equation (4), one obtains

$$\theta(y;b,g) = \int_0^y \frac{bgdy}{\sqrt{P(y;\, b,g)}} \tag{5}$$

where the polynomial *P* is defined as

$$P(y;b,g) = g^2\left(1 - b^2y^2\right) + 4\left(y^6 - y^{12}\right) \tag{6}$$

Equations (5) and (6) introduce dimensionless variables

$$b=\frac{b'}{\sigma};\quad g^2=\frac{\frac{1}{2}m\left(g'\right)^2}{\varepsilon};\quad \phi=\frac{\phi'}{\varepsilon};\quad \text{and}\quad y=\frac{\sigma}{r'} \tag{7}$$

A dimensionless inverse radius y conveniently changes the integration domain in Equation (5) from open, $r\in\left[r,\infty\right)$, to closed, $y\in\left[0,y\right]$.

The dimensionless inverse distance of closest approach, y_{m}, is the smallest positive root of the polynomial P,

$$y_{\mathrm{m}}\left(b,g\right)=\min\left\{y_{\mathrm{m}}^i:y_{\mathrm{m}}^i\in R^+,P\left(y_{\mathrm{m}}^i;b,g\right)=0\right\} \tag{8}$$

For a given two-particle encounter, the incoming trajectory can be drawn with Equation (5); the outgoing trajectory can be found by reflection about a radial line inclined at the closest-approach angle $\theta_{\mathrm{m}}=\theta\left(y_{\mathrm{m}};b,g\right)$.

Reduced collision integrals $\Omega^{(l,s)\star}$ result from a threefold integration: one over all inverse trajectory radii, the closed domain of $y\in\left[0,y_{\mathrm{m}}\right]$; one over all impact parameters, the semi-infinite domain $b\in[0,\infty)$; and one all relative speeds, $g\in[0,\infty)$. The sequence of integrals used to obtain $\Omega^{(l,s)\star}$ is [9,24-26]

$$\chi\left(b,g\right)=\pi-2\theta_{\mathrm{m}}=\pi-2bg\int_0^{y_{\mathrm{m}}}\frac{dy}{\sqrt{P\left(y;b,g\right)}}\ , \tag{9}$$

$$Q^{(l)\star}\left(g\right)=\frac{2}{\left[1-\frac{1}{2}\cdot\frac{1+(-1)^l}{1+l}\right]}\int_0^\infty\left[1-\cos^l\chi\left(b,g\right)\right]b\,db\ , \tag{10}$$

$$\Omega^{(l,s)\star}\left(T^*\right)=\frac{2}{\left(s+1\right)!T^{*s+2}}\int_0^\infty\exp\left(-\frac{g^2}{T^*}\right)g^{2s+3}Q^{(l)\star}\,dg \tag{11}$$

These include the deflection angle χ (cf. Figure A-2) and introduce the reduced collision cross-section $Q^{(l)\star}$. (Quantities with a superscript $\star$ are scaled by the corresponding functions obtained with hard-sphere potential.)

The hyper-elliptic integral that arises in Equations (9) for LJ (12–6) particles cannot be solved analytically. While computing collision integrals numerically, y_m, χ, $Q^{(l)\star}$, and $\Omega^{(l,s)\star}$ must be calculated within strict accuracy limits. Singularities, discontinuities, and oscillations of the functions involved impede high-precision calculations [1].

A.3.2 Distance of closest approach

The reciprocal of the closest approach distance y_m (cf. Equation (8)) must be calculated first, because it sets the upper bound of integration in Equation (9). At this stage it is important to assess whether P (cf. Equation (6)) affords multiple real positive roots. When interaction potentials have both attractive and repulsive character, two particles can spiral around each other or even fall into orbit (following 'looping' trajectories), rather than undergoing a simple collision. Orbits correspond to parameter combinations that yield minimal real positive roots of P with multiplicity higher than 1.

Akhmatskaya and Pozhar [14] found combinations that lead to orbits using the characteristic of double roots

$$P\left(y_m^i;b,g\right)=\frac{dP\left(y_m^i;b,g\right)}{dy}=0 \tag{12}$$

On thus finds that y_m^i is a double root of P when

$$y_m^i=\sqrt[6]{\frac{1}{5}\pm\frac{1}{5}\sqrt{1-\frac{5}{4}g^2}}\,. \tag{13}$$

Insertion of Equation (13) into Equation (6) determines a relationship between b and g that, when satisfied, shows that an encounter will result an orbit. Only the smaller of the

two roots in Equation (13) actually yields orbiting trajectories; the larger does not satisfy Equation (8).

One might ask whether combinations of b and g that satisfy Akhmatskaya and Pozhar's conditions are the *only* orbiting trajectories within the domains of b and g. Uniqueness of these orbits can be proved by enumerating the real positive roots afforded by the polynomial P. Hostetter's modification to the Routh-Hurwitz test [34,35] allows the values of a polynomial's coefficients to be used to count how many real, positive roots it affords. The Hostetter-Routh-Hurwitz test shows P has three real positive roots when $g \le 2/\sqrt{5}$,

$$\begin{aligned} &\frac{2\sqrt{3}}{5^{1/3}g}\left[1-\left(1-\frac{5g^2}{4}\right)^{1/2}\right]^{1/3}\left[\frac{3}{5}+\frac{2}{5}\left(1-\frac{5g^2}{4}\right)^{1/2}\right]^{1/2} \\ &\le b \le \frac{2\sqrt{3}}{5^{1/3}g}\left[1+\left(1-\frac{5g^2}{4}\right)^{1/2}\right]^{1/3}\left[\frac{3}{5}-\frac{2}{5}\left(1-\frac{5g^2}{4}\right)^{1/2}\right]^{1/2} \end{aligned} \tag{14}$$

Otherwise, P possesses a single real positive root.

Figure A-3 summarizes characteristics of the polynomial P and values of its least root y_m. Two lines on the figure delineate the boundaries of the domains of b and g where P affords repeat positive roots. On the upper ($y_m^1 = y_m^2 > y_m^3$) and the lower ($y_m^1 > y_m^2 = y_m^3$) lines, one of the three roots has multiplicity 2; there is a triple root at the point $(g,b) = \left(2/\sqrt{5}, 3/\sqrt[3]{5}\right)$. The upper double-root line on Figure A-3 has no physical significance because if the double root is larger than the single root, a trajectory will never traverse its position.

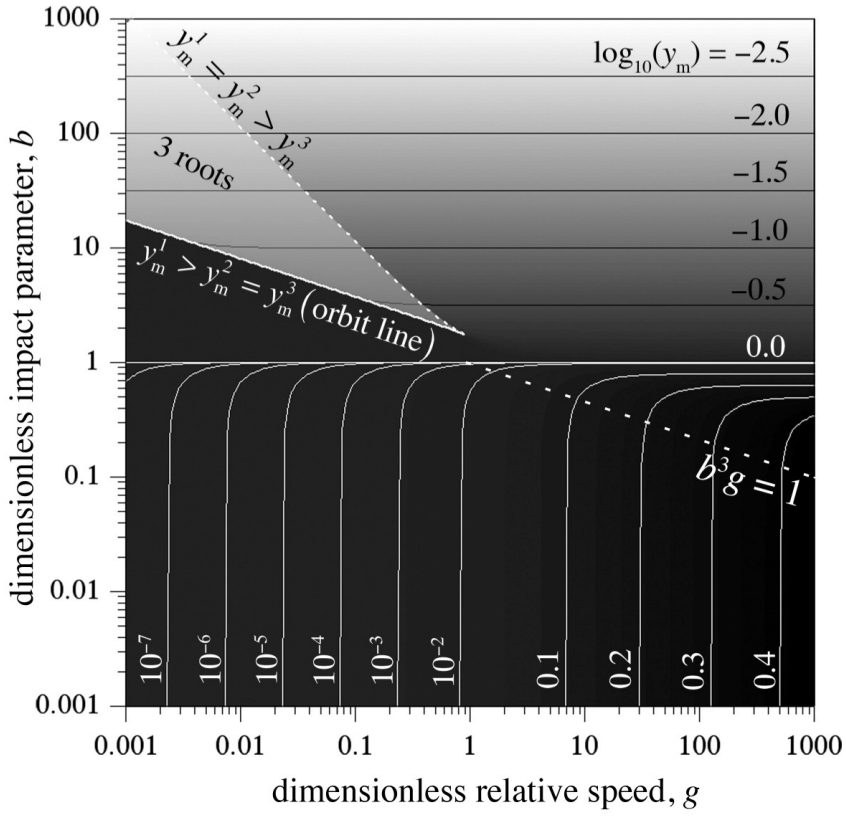

Figure A-3. Contour plot of the inverse closest-approach distance y_m with respect to b and g for Lennard-Jones (12–6) particles. The polynomial P of Equation (6) affords either three real positive roots or just one in this domain. On the 'orbit line' b and g combine to make the deflection angle χ diverge.

The line where the minimum root repeats corresponds to a situation where two particles fall into orbit during an encounter. Because of this characteristic, the lower curve on Figure A-3 will be called the 'orbit line', described when $g \le 2/\sqrt{5}$ by

$$b_o(g) = \frac{2\sqrt{3}}{g\sqrt[3]{5}} \sqrt[3]{1 - \sqrt{1 - \frac{5g^2}{4}}} \sqrt{\frac{3}{5} + \frac{2}{5}\sqrt{1 - \frac{5g^2}{4}}} \tag{15}$$

Newton's method [36] was used in combination with Horner's scheme for synthetic division [37] to establish the positions of the real roots of P with high accuracy. The asymptotic behavior of y_m helps provide a clue toward useful initial guesses for the algorithm. The shapes of the y_m contours on Figure A-3 change around a hypothetical line $b^3 g = 1$. Asymptotic analyses show that the following relations are reliable initial guesses for roots:

$$y_m \approx \begin{cases} 1 \text{ if } g < \frac{2}{\sqrt{5}} \text{ and } b < b_o, \\ \sqrt[6]{\frac{1}{2} + \frac{1}{2}\sqrt{1 + g^2}} \text{ if } g \ge \frac{2}{\sqrt{5}} \text{ and } b^3 g \ll 1, \\ \frac{1}{b} \text{ if } b > b_o \text{ or } b^3 g \gg 1 \end{cases} \tag{16}$$

When b3g ≈ 1, the last two guesses yield similar results. In this work, 1/b was used when $b > b_o$ or $b^3 g \ge 1$.

Newton's method reliably finds the first root of P. In the 3-root region, P can be reduced in order by synthetic division, Newton's method can be applied to locate the second root, and a sequential division can be performed to find the third. Truncation errors introduced by division can be mitigated by using these preliminary results as guesses for roots with the original polynomial P.

High precision y_m values are essential; their accuracy limits all further calculations. To verify accuracy Equations (6) and (8) were combined, yielding

$$\tilde{b}(g,y_{\mathrm{m}}) = \frac{2y_{\mathrm{m}}^2(b,g)}{g}\sqrt{\frac{g^2}{4y_{\mathrm{m}}^6(b,g)} + 1 - y_{\mathrm{m}}^6(b,g)} \tag{17}$$

Here $\tilde{b}$ is equivalent to b; their difference tracks the accuracy of y_{m}. (When y_{m} nears 1, a new variable $x_{\mathrm{m}} = y_{\mathrm{m}} - 1$ can be introduced to avoid truncation errors.) Equation (17) confirmed that computed y_{m} values were accurate to machine precision–fourteen significant digits.

A.3.3 Deflection angle

Once closest-approach distances y_{m} are known, the task of evaluating the deflection angle χ presents itself. Since P always has at least one real positive root, the integrand in Equation (9) always has a singularity at the upper bound of integration. Roots at the upper bound correspond to poles in the integrand of order 1/2, 1, or 3/2.

Singularities of order 1/2 at $y = y_{\mathrm{m}}$ in the integrand can be removed by a change of integration variable. First, relying on the fact that P is even, factor it to

$$P(y;b,g) = \frac{(y_{\mathrm{m}} - y)(y_{\mathrm{m}} + y)}{y_{\mathrm{m}}^2} R\left(\frac{y}{y_{\mathrm{m}}};b,g\right), \tag{18}$$

where R is a 10^{th}-order even polynomial,

$$R(x;b,g) = \sum_{k=0}^{5} B_k(b,g)\,x^{2k}, \tag{19}$$

Whose coefficients are given by Horner's scheme as

$$B_5 = B_4 = B_3 = 4y_{\mathrm{m}}^{12};\ B_2 = B_1 = B_3 - 4y_{\mathrm{m}}^6;\ B_0 = g^2. \tag{20}$$

Inserting $u = (2/\pi)\sin^{-1}(y/y_{\mathrm{m}})$ transforms Equation (9) to

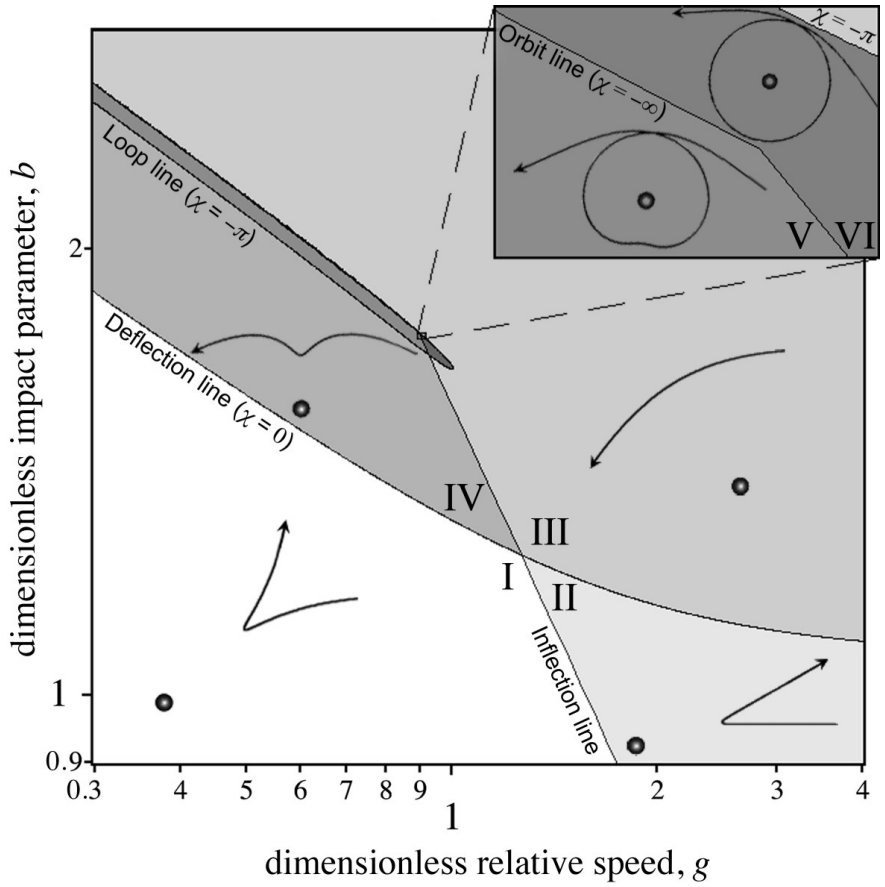

Figure A-4. Map showing how trajectory shapes depend on the impact parameter and relative speed for binary Lennard-Jones (12–6) interactions. Six different trajectory types, drawn using Equation (5), are represented. An inset shows behavior in the region bounded by the loop line, where spiraling trajectories occur. Orbits ($\chi \to \infty$), undeflected trajectories ($\chi = 0$) and head-on collisions ($b = 0$, $\chi = \pi$) have no statistical weight in the ensemble and are not depicted.

Table A-3. Comparison of calculated deflection angles.

g^2=0.1	Deflection angle χ (radian)			
b	Hirschfelder *et al*. [9]	Sharipov *et al*. [39][a]	This work	Region in Figure A-4
2.838	-0.323	-0.3230	-0.3230	III
2.696	-0.543	-0.5435	-0.5435	III
2.643	-0.706	-0.7049	-0.7049	III
2.598	-0.945	-0.9437	-0.9437	III
2.572	-1.205	-1.199	-1.199	III
2.544	-1.998	-1.977	-1.977	III
2.539	-2.576	-2.584	-2.584	III
2.538	-2.346	-2.903	-2.903	III
2.516	-1.166	-4.944	-4.481	V
2.503	-1.944	-2.324	-3.959	V
2.470	-2.867	-3.081	-3.203	V
2.456	-3.106	-2.984	-2.984	IV
2.400	-2.509	-2.356	-2.356	IV
2.328	-1.943	-1.819	-1.819	IV
2.171	-1.124	-1.041	-1.041	IV
1.996	-0.491	-0.4360	-0.4360	IV
1.881	-0.150	-0.1119	-0.1119	IV

[a]Sign convention matched to Ref. 9

$$\frac{\chi(b,g)}{\pi} = 1 - bgy_{\mathrm{m}} \int_0^1 \frac{du}{\sqrt{R\left(\sin\frac{1}{2}\pi u; b, g\right)}}, \tag{21}$$

This integrand is finite across its domain when P has just one root. When b and g are on the orbit line, however, poles of order 1 or 2 occur at $u = 1$; then $\chi \to -\infty$.

Hirschfelder et al. [9, 24–26] replaced the integrand in their equivalent of Equation (21) with a best-fit polynomial. This injected numerical error without specific bounds. Akhmatskaya and Pozhar [14] brought more rigors to the analysis, using Gauss-Chebyshev quadrature to approximate the integral with bounded error [38].

For the present work a 4th-order Runge-Kutta method (RK4)[36] was adapted to perform the integration in Equation (21). Grid-independent values valid to machine precision were extrapolated by using the known dependence of error on mesh spacing in the RK4 scheme. Results matched those of Colonna and Laricchiuta's fractal integration algorithm [1], which yields results of similar accuracy at considerably greater computational expense.

Figure A-4 maps out the characteristic shapes of trajectories with respect to the impact parameter b and relative speed g. Although this sort of map can greatly aid the physical understanding of pair potentials, to the best of our knowledge, Figure A-4 is the first topological diagram of its kind. Four lines demarcate regions where 'collisions' ($0 \le \chi$), 'deflections' ($-\pi \le \chi < 0$), 'loops' ($\chi < -\pi$) and orbits ($\chi \to -\infty$) occur. Trajectories can also have inflection points, dividing the map into six domains.

Representative trajectories obtained by solving Equation (5) are included in each region that occupies finite area on the map. In regions I and II of Figure A-4, the impact parameter is relatively small; particles therefore collide with a trajectory dominated by

short-range repulsion. Some effect of attraction is seen for trajectories in region I, where kinetic energy (which scales as g^2) is lower. In regions III and IV, the impact parameter is relatively large, so interactions are dominated by long-range attraction, which ultimately causes the incoming particle to be deflected toward the incident particle from its original path. In region III, the kinetic energy is large enough that repulsion does not have a significant effect; incoming gas particles primarily experience long-range attraction. When kinetic energy is smaller, in region IV, the particles are drawn sufficiently close together by the attractive force that repulsion comes into effect. In regions V and VI, kinetic energy is low enough that particles spiral around each other one or more times before the attractive force can be overcome. Qualitatively dissimilar loops appear above and below the orbit line, in regions V and VI, respectively.

Table A-3 compares deflection angles yielded by the extrapolative RK4 algorithm described above to computations by Hirschfelder *et al*.[9] and Sharipov and Bertoldo [39]. The squared relative speed g^2 is fixed to 0.1, and the impact parameter b is varied to pass through regions III, IV, and V. Results from extrapolative RK4 identify with Sharipov and Bertoldo's, excepting in region V, where they differ significantly. Sharipov and Bertoldo split Equation (9) into two integrations; in one of the domains P was linearized around its roots. In regions V and VI of the trajectory map the second derivative of P can be larger than its first, and quadratic behavior of P dominates. Thus Sharipov and Bertoldo's method fails in domains where trajectories exhibit loops.

Inflections occur when $d^2\theta/dy^2$ changes sign during an encounter, which happens only if dP/dy changes sign. Either dP/dy has two real positive roots or it has none [34, 35]. These domains of b and g are separated by a line where the root repeats, which can be

found by Akhmatskaya and Pozhar's method [14] to be $bg = 6/\sqrt[6]{3125}$ (the 'inflection line' on Figure A-4). Roots of *dP*/*dy* must also be less than y_m to yield inflected trajectories, so the orbit line also bounds regions I, IV, and V in Figure A-4.

Orbiting trajectories and those in regions I, III, IV and VI are well documented,[1, 9, 14, 24, 26, 28, 39–41] but to the best of our knowledge regions II and V have not been discussed. Region V is most important because looping trajectories dramatically affect collision cross-sections.

A.3.4 Collision cross section

Divergent deflection angles make the integrand of the reduced cross section $Q^{(l)\star}$ take on fractal character, oscillating with increasing frequency as the orbit line is approached. The integrand in Equation (10) is not Riemann integrable in the neighborhood of b_o (cf. Equation (15)); at b_o, it is undefined. Earlier sources approximate χ near the orbit line, taking $\chi \propto 1/\sqrt{b^2 - b_o^2(g)}$, and using the proportionality constant as a fitting parameter. This accounts neither for the discontinuity in nor the non-analyticity of cos χ near b_o. Even the most authoritative earlier sources [14, 24] do not address the error this approximation incurs.

An *ad hoc* Lebesgue integration can be used to circumvent the non-analyticity of the integrand in Equation (10) at the orbit line. A measure of the error in the integral's value as it crosses bo is provided by cutting out a small area of the integration domain around b_o, $b \in [b_0 - \delta, b_0 + \delta]$. In any region of the trajectory map, the upper bound of the integrand in Equation (10) is *b* for even *l* and 2*b* for odd *l*, because $-1 \le \cos\chi \le 1$; the

lower bound is always zero. Thus the exclusion of a neighborhood of size 2 around bo induces an error in resulting $Q^{(l)\star}$ values of at most $2b_o$ for even l and $4b_o$ for odd l. It follows that numerical error in the integral as a whole can be controlled by the choice of δ; an exact integral can be calculated in principle by taking a limit as the measure δ goes to zero.

To resolve difficulties with the semi-infinite integration domain in Equation (10), observe that integrands in $Q^{(l)\star}$ always behave similarly when impact parameters are large. Asymptotic behavior was analyzed to inform a decision procedure for terminating the upper bound of the integration domain at a predefined level of accuracy. The asymptotic analysis begins with Equations (6) and (16). When b is much greater than 1, P asymptotically satisfies

$$\lim_{b\gg 1} P\left(y_{\mathrm{m}}\right) = g^2\left(1-b^2 y_{\mathrm{m}}^2\right) + 4y_{\mathrm{m}}^6 + O\left(\frac{1}{b^{12}}\right). \tag{22}$$

An asymptotic formula for y_{m} follows from Equation (8). Insertion into Equations (18), (20), and (21) yields the asymptotic behavior of the deflection angle. Maclaurin expansion of the cosine ultimately provides the formula

$$\lim_{b\gg 1}\left(1-\cos^l\chi\right)b = \frac{225\pi^2 l}{32g^4 b^{11}} + O\left(\frac{1}{b^{17}}\right) \tag{23}$$

The collision-cross-section integrand and Equation (23) are depicted in Fig. 5; they match if b is sufficiently large.

Equation (23) allows estimation of the error induced by truncating the integration domain in Equation (10) at finite upper bound b_{stop}. Presuming that $b_{\mathrm{stop}} \gg 1$, the portion of the semi-infinite integral lost is

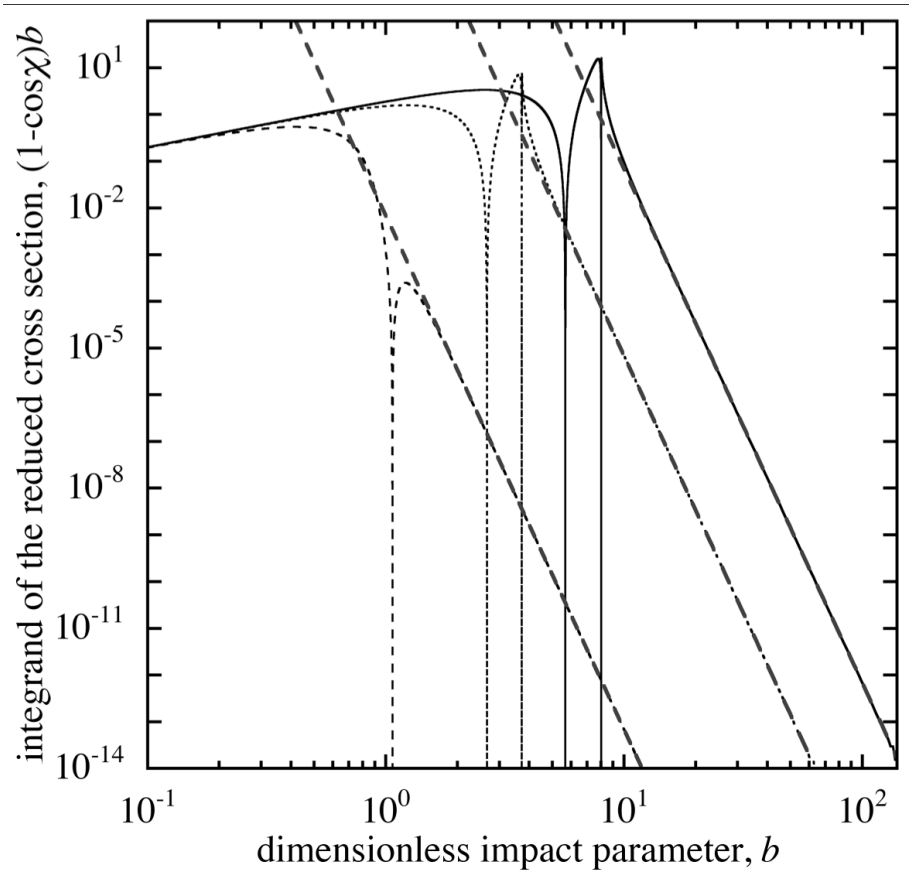

Figure A-5. Integrands of the reduced cross sections, $Q^{(l)\star}$, and the asymptotic behavior for $b \gg 1$, with $l = 1$. Solid line, $g = 0.001$; dotted line, $g = 0.1$; short dashed line, $g = 10$; long- dashed lines show the asymptotic behavior from Equation (23).

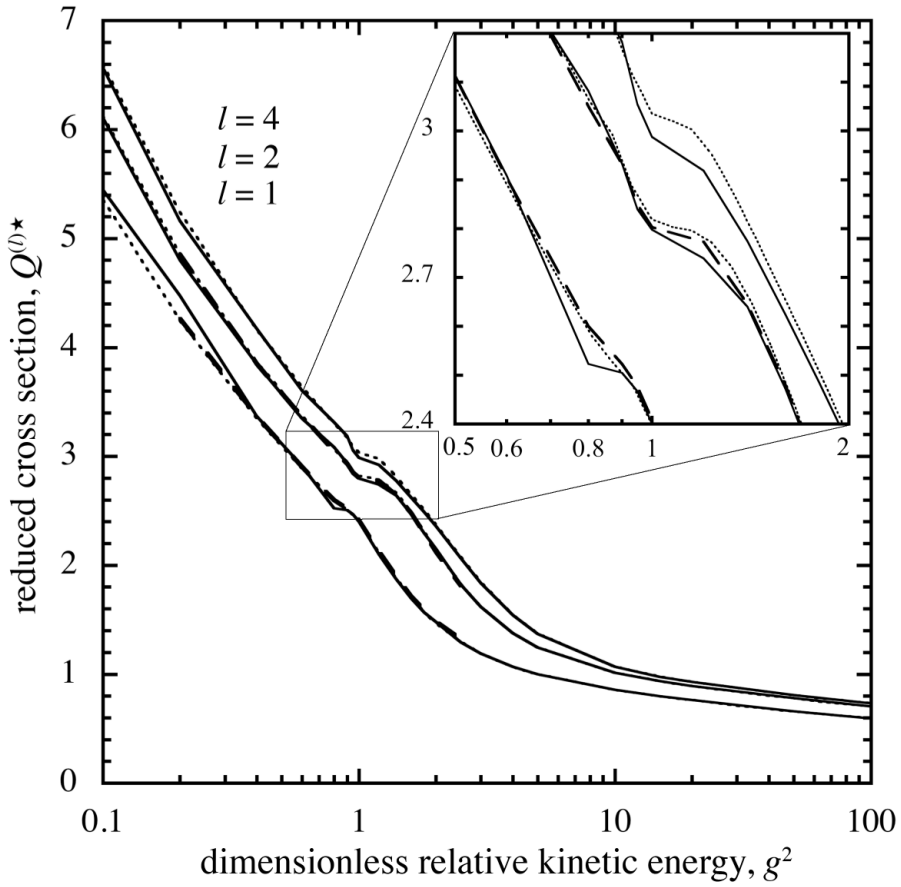

Figure A-6. Collision cross section $Q^{(l)\star}$ as a function of relative kinetic energy g^2. The solid lines are reprinted from Hirschfelder *et al*. [24]; the dashed lines are from Storck [40]; the dotted lines represent calculations accurate to 6 digits based on the methods discussed here. The inset shows significant differences when g^2 is near unity.

$$\int_{b_{\text{stop}}}^{\infty}\left[\lim_{b\gg 1}\left(1-\cos^{l}\chi\right)b\right]db=\frac{45\pi^{2}l}{64g^{4}b_{\text{stop}}^{10}}+O\left(\frac{1}{b_{\text{stop}}^{16}}\right) \tag{24}$$

Marching forward from $b = 0$ with RK4, the ratio of the area lost by truncation of the domain to the area already integrated can be monitored to decide when to halt the numerical procedure.

Figure A-6 compares collision cross sections previously reported by Hirschfelder *et al*. [24] and Storck [40] to those developed here, as functions of the dimensionless kinetic energy g^2. For the present calculations 6-digit accuracy (0.00001% error) was deemed sufficient. The inset in Figure A-6 shows significant differences between the present results and Storck's for a range of g^2 values between 0.5 and 2.0. These differences owe to Storck's neglect of the trajectories in region V and VI of Figure A-4.

A.3.5 Collision integrals

The reduced collision integrals $\Omega^{(l,s)\star}$ defined in Equation (11) are more readily computed than other preliminary quantities. Although the integration domain is also semi-infinite, the integrand decreases rapidly with g^2, making it easier to create procedures to terminate the integration with bounded error. The exponentially decreasing character allows precision to be insured by a procedure where the forward-marching RK4 integration is halted when the integrand becomes smaller than a target value.

Collision integrals with 6 digits of precision (0.00001% accuracy) are tabulated in the supplementary material. (Values with higher accuracy could be evaluated using the methods suggested above.) Equation (1) was obtained by fitting this table with the method of least squares, as discussed in chapter 0. As a result, Equation (1) generates

collision integrals accurate to at least four significant digits when $0.3 \le T^* \le 400$. This accuracy is well within the bounds of intrinsic experimental error on transport-property measurements, and should suffice for most continuum heat, mass, and momentum transport analyses.

The present computations deviate up to 2% from those of Hirschfelder *et al*. at low reduced temperature, $T^* = 0.3$, consistent with the observation of Akhmatskaya and Pozhar [14]. There is a larger difference, up to 3.5% at $T^* = 400$. This is consistent with NJA's observation that previous computations were in error at large T^* [16].

A.4 Optimal Lennard-Jones parameters for Neon, Argon, and Krypton

Finding the pair potential that best describes a particular type of particle is a challenging inverse problem. The temperature dependences of transport properties are in principle known from experiments, with various degrees of measurement error. Parameterization of a potential requires that these data be simultaneously fit with calculations from kinetic theory—or at least, it should. A true optimization has not yet been performed, because iterative procedures in which LJ parameters vary require prohibitively time-intensive collision-integral calculations.

Previous efforts to establish pair potentials in gases have also tended to use one set of property data, such as the second virial coefficient [42] or viscosity [24], and varied both LJ parameters in an ad hoc fashion to obtain a best fit. Such procedures do not guarantee an optimal choice that minimizes the error across multiple properties.

It is worth mentioning that many papers call into question whether the LJ potential accurately models gas-particle interactions at all [18, 43–45]. When considering such

criticisms, it should be borne in mind that the true test of a potential model is whether it accurately predicts how macroscopic thermodynamic and transport properties depend on temperature—with 'accurately' taken to mean 'within the bounds of intrinsic experimental error for all known data at all accessible temperatures.' Since accurate collision-integral tables have never been used for this sort of multiobjective optimization of the LJ potential, it is impossible to judge whether or not the potential models any real gas well. To address this concern, simultaneous best fits of the two most accurately known properties (second virial coefficient and viscosity) of a gas were used to parameterize the LJ potential; the predictive capability of the potential was then tested by comparison to less accurately known properties (thermal conductivity and self-diffusion coefficient). All four properties for Ne, Ar, and Kr were matched within experimental error.

Virial coefficients are thermodynamic properties. By definition, they correct the pressure-explicit equation of state for an ideal gas according to

$$\frac{p\overline{V}}{N_{\mathrm{A}}k_{\mathrm{B}}T} = 1 + \frac{B_{2\mathrm{V}}(T)}{\overline{V}} + \frac{B_{3\mathrm{V}}(T)}{\overline{V}^2} + \cdots, \tag{25}$$

in which the second coefficient $B_{2\mathrm{V}}$ reflects pairwise interactions, the third virial coefficient $B_{3\mathrm{V}}$ quantifies pairwise and three-body interactions, *etc* [46]. Here p is pressure, $\overline{V}$ is the molar volume, and N_{A} is Avogadro's number. In a pure gas $B_{2\mathrm{V}}$ varies with temperature as [47]

$$B_{2\mathrm{V}}\left(T^*\right) = 2\pi\sigma^3 N_{\mathrm{A}} \int_0^\infty \frac{1}{y^4}\left\{\exp\left[-\frac{y^{12}-y^6}{T^*}\right]-1\right\}dy. \tag{26}$$

Lennard-Jones considered a number of pair potentials, ultimately settling on the form in (4) [48, 49].

Transport coefficients depend on collision integrals of various orders, which in turn depend on the pair potential. Hirschfelder *et al*. implemented one of the first attempts to determine LJ parameters from a transport property—viscosity. The viscosity η is given terms of collision integrals for an LJ gas as [9]

$$\eta\left(T^*\right) = \frac{5\sqrt{\pi\varepsilon m T^*}}{16\pi\sigma^2\Omega^{(2,2)\star}\left(T^*\right)} f_\eta^{(n)}. \tag{27}$$

Here $f_\eta^{(n)}$ denotes a function that brings η up to the n^{th} order in the Sonine expansion. The thermal conductivity k and the self-diffusion coefficient $\mathscr{D}$ are

$$k\left(T^*\right) = \frac{75k_{\text{B}}}{64\sigma^2\Omega^{(2,2)\star}\left(T^*\right)}\sqrt{\frac{\varepsilon T^*}{\pi m}} f_k^{(n)} \quad \text{and} \tag{28}$$

$$\mathscr{D}\left(T^*\right) = \frac{3\sqrt{\pi\varepsilon m T^*}}{8\pi\sigma^2\rho\left(T^*, p\right)\Omega^{(1,1)\star}\left(T^*\right)} f_{\mathscr{D}}^{(n)}, \tag{29}$$

where $f_k^{(n)}$ and $f_{\mathscr{D}}^{(n)}$ represent corrections of n^{th} order. Since it involves the density ρ, given up to second order in the virial expansion by

$$\rho\left(T^*, p\right) = \frac{mN_{\text{A}}}{2B_{2\text{V}}\left(T^*\right)}\left[-1 + \sqrt{1 + \frac{4pB_{2\text{V}}\left(T^*\right)}{\varepsilon N_{\text{A}} T^*}}\right], \tag{30}$$

computation of the self-diffusion coefficient $\mathscr{D}$ involves a computation of $B_{2\text{V}}$ as well as the collision integrals.

Use of higher-order corrections improves accuracy of the property in question, but only up to a point—Viehland et al.[50] demonstrated that convergence of the approximation is ordinarily very rapid, and that third- and fourth-order calculations of the viscosity in the dimensionless temperature range $0.3 \le T^* \le 400$ differ by less than

0.004%, far less than the 2.5% experimental error in viscosity measurement. Hurly and Moldover showed that third- and fourth-order accurate calculations of thermal conductivity differ by less than 0.01% over a wide temperature range [51]. For this work, $f_\eta^{(3)}$, $f_\lambda^{(3)}$, and $f_\mathscr{D}^{(2)}$, were deemed sufficiently accurate for use in Lennard-Jones parameterization. These are written in terms of collision integrals in the A-A Appendix.

An LJ parameterization effort requires reliable experimental data that quantify the temperature dependence of B_{2V}, η, λ, and $\mathscr{D}$ were needed. Here 'reliable' is interpreted to mean that the experiments were replicated and reported with quantitative estimates of experimental error. Maitland and Smith [52] performed an extensive data search for gas viscosities, and aggregated literature data to generate tables accurate within 2.5% for the viscosities of Ne, Ar, and Kr between their boiling points and 2000 K. Saxena *et al*.'s data were used for thermal conductivities between 350K and 1500K, which have 4.0% maximum error [53–56].

In the case of self-diffusion coefficients, experimental values are quite sparse, so in addition to self-diffusion coefficients [44,49,69,70,71], we also gathered mutual-diffusion coefficients for isotopic mixtures [48,64]. Mutual diffusion coefficients were converted to self-diffusion coefficients by correcting for the composition differences between the equilibrated isotopic mixtures and naturally occurring isotope ratios. Some reports of self-diffusion coefficients did not provide error estimates [48,70,71], but most report intrinsic error of 2~3%.

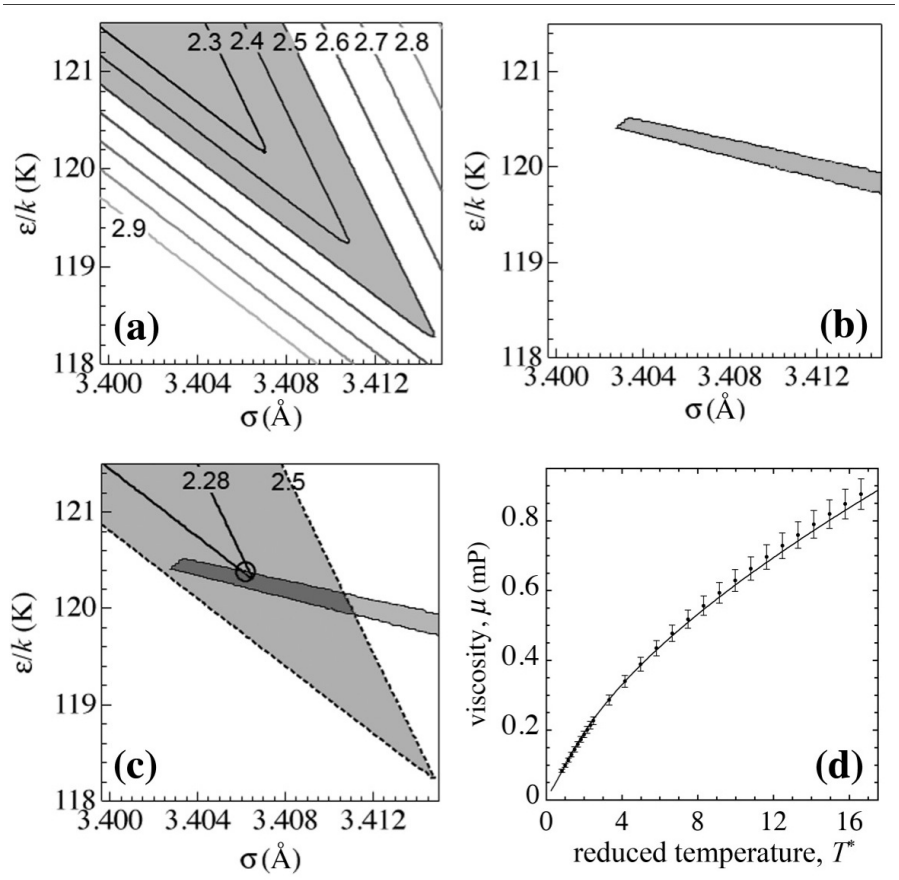

Figure A-7. Procedure for LJ parameterization of argon: (a) contours of the maximum percentage deviation between theoretical and calculated viscosity values (the viscosity-correct region where calculations match experiments is shaded); (b) virial-correct region; (c) contraction of the viscosity-correct region to minimize error in viscosity within dual-correct region; (d) comparison of results to experiments.

Measurements of both self-diffusion coefficients [57–61] and mutual-diffusion coefficients at atmospheric pressure were collected [62, 63]. Mutual diffusion coefficients were converted to self-diffusion coefficients by correcting m for the composition differences between equilibrated isotopic-mixture compositions and naturally occurring isotope ratios. Some reports do not provide error estimates [60–62]; most report error of a few percent.

The extensive tables produced by Dymond and Smith [64], which compile measurements by numerous groups over several decades, were used for B2V data. Error ranges for second virial coefficients are typically provided as absolute values, rather than percentages, on the basis that B_{2V} is very close to zero when gases behave near ideally. Error in B_{2V} ranges from 0.5-1 cm^3/mol.

To determine optimal LJ parameters, experimental data quantifying the temperature dependences of viscosity η and second virial coefficient B_{2V} were fit with Equations (26) and (27), using equations (31) and (32) from the appendix to get $f_\eta^{(3)}$ in terms of collision integrals, and Equation (1) to compute the collision integrals. This approach strictly tests the potential chosen by using both a thermodynamic property and a transport property—parameters computed by two distinct theories. Among the transport coefficients, viscosity was chosen as the objective for LJ parameter optimization because it has the least error and is recorded over the widest T range.

LJ parameter optimization was facilitated by a graphical method illustrated in Figure A-7 for argon. A contour plot of the maximum percentage deviation between theoretical and experimental η values was created *vs.* σ and ε/k_B. The experimental error of 2.5% corresponds to one of these contours, delineating a 'viscosity-correct' region in

which all combinations of σ and ε/k_B correctly predict the temperature dependence of viscosity. In a similar plot for B_{2V}, a 'virial-correct' region was identified by creating a Boolean function that took value 1 if all predicted B_{2V} values for a given σ and ε/k_B were within experimental error, and 0 otherwise, and coloring the two values differently. Any σ and ε/k_B values within the intersection of the 'viscosity-correct' and 'virial-correct' regions match both properties within error. Since this overlapping area has finite size, a further constraint is needed to determine exact parameter values. Viscosities are more precisely measured, so the deviation from experimental viscosity data within this 'dual-correct' domain was minimized: the error tolerance on the 'viscosity-correct' domain was reduced until it met the 'virial-correct' domain at a point (within the precision of Equation (1)).

Validity of the LJ parameter optimization was tested by using parameters fit to η and B_{2V} to predict k and $\mathscr{D}$; the predictions were subsequently compared to experimental data. Thermal conductivity strongly correlates to viscosity. The self-diffusion coefficient is a more stringent test of a potential model, because in addition to depending on a different order of collision integral than η, it also depends on B_{2V}.

Optimal LJ parameters for Ne, Ar, and Kr are shown in Table A-4, which also compares property predictions to those based on LJ parameters provided by earlier researchers [9, 42, 65]. Ironically, Lennard-Jones' parameters (the oldest) are closer to the ones obtained here than any others, because Lennard-Jones based his parameter optimization on the second viral coefficient alone, avoiding a reliance on faulty collision-integral computation. Hirschfelder et al. suggested that their LJ parameters would describe pair potentials better because of the lower intrinsic error of viscosity

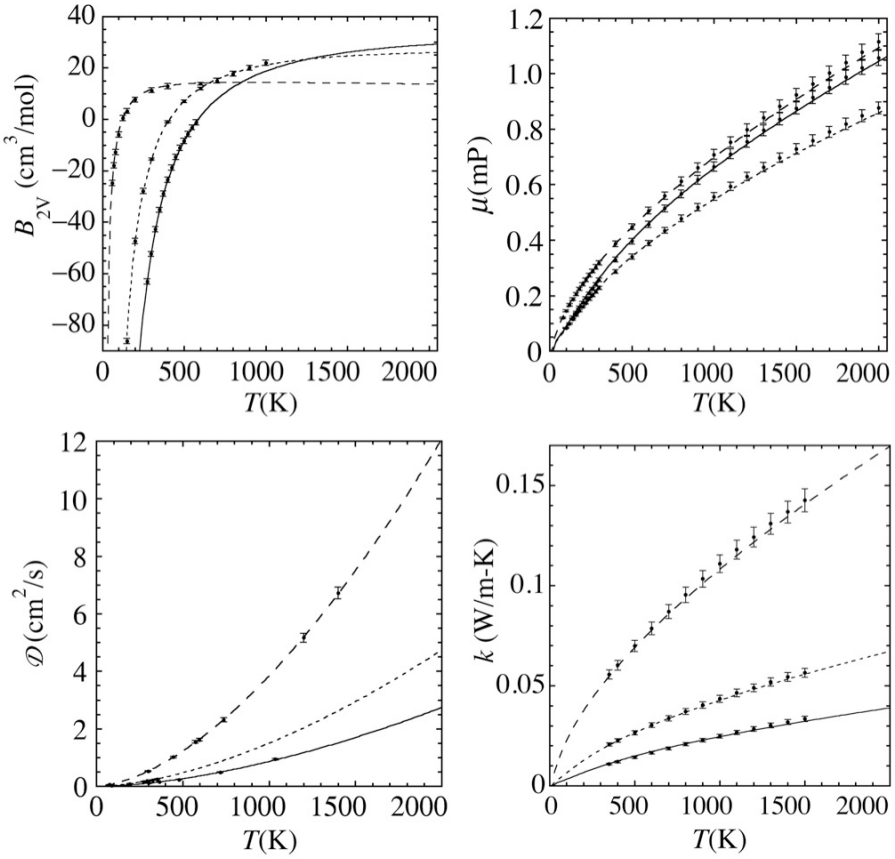

Figure A-8. Optimal LJ parameters generate four different gas properties accurately within experimental error. Each graph includes three gases: neon (dashed), argon (dotted), and krypton (solid). Data for $\mathcal{D}$ are at 101325 Pa.

Table A-4. Comparison of LJ parameters from this work to literature values for Ne, Ar, and Kr, showing average and maximum deviation from measured transport properties, as well as the number of points located inside the virial-correct region on Figure A-7. Intrinsic experimental errors are written parenthetically next to η, k, and $\mathcal{D}$.

					η (2.5%)		k (4%)		$\mathcal{D}$ (≥ 3%)		
Gas	Group	Properties used for parameterization	ε/k (K)	σ (Å)	avg	max	avg	max	avg	max	B_{2V}
Ne	Lennard-Jones	B_{2V}	35.35	2.743	2.6	5.3	0.8	1.9	2.8	4.3	6/10
	Hirschfelder	η	35.7	2.80	1.3	2.2	4.0	5.2	0.7	1.4	8/10
	Kestin	η	60.89	2.6481	1.3	8.8	1.0	2.1	2.4	12.	0/10
	This work	η, B_{2V}	35.750	2.7820	1.3	2.0	2.8	4.0	0.7	1.5	10/10
Ar	Lennard-Jones	B_{2V}	119.5	3.408	1.8	2.5	2.7	2.8	1.1	2.6	10/11
	Hirschfelder	η	124.0	3.418	2.0	3.4	3.8	4.0	1.3	3.2	3/11
	Kestin	η	152.75	3.2923	1.4	6.4	0.4	0.5	2.2	7.5	0/11
	This work	η, B_{2V}	120.38	3.4062	1.8	2.3	2.7	2.8	1.1	2.4	11/11
Kr	Hirschfelder	η	190.0	3.61	2.1	3.3	3.5	4.5	2.2	4.4	0/13
	Kestin	η	206.42	3.5222	1.1	2.8	0.3	1.5	1.3	2.2	0/13
	This work	η, B_{2V}	171.64	3.6202	1.5	2.5	2.4	3.0	1.4	3.0	13/13

measurements. Table A-4, however, shows that Hirschfelder et al. found inaccurate LJ parameters due to faulty collision-integral calculation. DiPippo and Kestin's more recent LJ parameterization [65] was based on the collision-integral tables of Hirschfelder et al., and is therefore similarly suspect.

A.5 Conclusion

An arbitrary-precision algorithm was developed to calculate collision integrals for the LJ (12–6) potential. To speed computation and solve inverse problems with variable LJ parameters, interpolation formulas with 4-digit accuracy were developed (Equation (1)). Optimal LJ parameters were computed for three gases by simultaneously fitting experimental data for the temperature dependence of viscosity and second virial coefficient. Collision integrals were involved in viscosity calculation, and the second virial coefficient came from a separate equilibrium theory. The LJ parameters that matched these properties were verified using the self-diffusion coefficient and thermal conductivity of the gases in question. LJ potentials were found that predict the temperature dependences of viscosities, thermal conductivities, self-diffusion coefficients, and second virial coefficients of neon, argon, and krypton within experimental error, over temperatures ranging from their boiling points to 2000 K.

This work could be extended to the property evaluations of polar gases using different intermolecular potential. Once a different form of potentials is introduced, one might repeat the steps in chapter 0 and 0 to evaluate the arbitrary collision integrals of the polar gas, and to get its empirical equations. Once the empirical equation is established, the steps in chapter 0 would provide the optimal parameters for the polar gas. The work

in this chapter was enough to prove that this suggested method is capable of calculating the properties of polar gases with high precision.

A-A Appendix: higher order corrections

The third-order viscosity correction includes a factor

$$f_{\eta}^{(3)} = 1 + \frac{b_{12}^2}{b_{11}b_{22} - b_{12}^2} + \frac{b_{11}\left(b_{12}b_{23} - b_{22}b_{13}\right)^2}{\left(b_{11}b_{22} - b_{12}^2\right)\det(\mathbf{b})}, \tag{31}$$

where the independent entries in the 3×3, symmetric matrix **b** are

$$\begin{aligned}
b_{11} &= 4\Omega^{(2,2)\star} \\
b_{12} &= 7\Omega^{(2,2)\star} - 8\Omega^{(2,3)\star} \\
b_{22} &= \tfrac{301}{12}\Omega^{(2,2)\star} - 28\Omega^{(2,3)\star} + 20\Omega^{(2,4)\star} \\
b_{13} &= \tfrac{63}{8}\Omega^{(2,2)\star} - 18\Omega^{(2,3)\star} + 10\Omega^{(2,4)\star} \\
b_{23} &= \tfrac{1365}{32}\Omega^{(2,2)\star} - \tfrac{321}{4}\Omega^{(2,3)\star} + \tfrac{125}{2}\Omega^{(2,4)\star} - 30\Omega^{(2,5)\star} \\
b_{33} &= \tfrac{25137}{256}\Omega^{(2,2)\star} - \tfrac{1755}{8}\Omega^{(2,3)\star} + \tfrac{1905}{8}\Omega^{(2,4)\star} - 135\Omega^{(2,5)\star} + \tfrac{105}{2}\Omega^{(2,6)\star} + 12\Omega^{(4,4)\star}.
\end{aligned} \tag{32}$$

The same order of thermal conductivity involves

$$f_{\lambda}^{(3)} = 1 + \frac{a_{12}^2}{a_{11}a_{22} - a_{12}^2} + \frac{a_{11}\left(a_{12}a_{23} - a_{22}a_{13}\right)^2}{\left(a_{11}a_{22} - a_{12}^2\right)\det(\mathbf{a})}, \tag{33}$$

where entries in the symmetric 3×3 matrix **a** are

$$\begin{aligned}
a_{11} &= b_{11};\ \ a_{12} = b_{12};\ \ a_{13} = b_{13}; \\
a_{22} &= \tfrac{77}{4}\Omega^{(2,2)\star} - 28\Omega^{(2,3)\star} + 20\Omega^{(2,4)\star} \\
a_{23} &= \tfrac{945}{32}\Omega^{(2,2)\star} - \tfrac{261}{4}\Omega^{(2,3)\star} + \tfrac{125}{2}\Omega^{(2,4)\star} - 30\Omega^{(2,5)\star} \\
a_{33} &= \tfrac{14553}{256}\Omega^{(2,2)\star} - \tfrac{1215}{8}\Omega^{(2,3)\star} + \tfrac{1565}{8}\Omega^{(2,4)\star} - 135\Omega^{(2,5)\star} + \tfrac{105}{2}\Omega^{(2,6)\star} + 4\Omega^{(4,4)\star}.
\end{aligned} \tag{34}$$

Second-order self-diffusion coefficients include

$$\frac{1}{f_{\mathcal{D}}^{(2)}} = 1 - \frac{\left(6C^{\star} - 5\right)^2}{55 - 12B^{\star} + 16A^{\star}}, \tag{35}$$

where

$$\begin{aligned} A^{\star} &= \Omega^{(2,2)\star} / \Omega^{(1,1)\star} \\ B^{\star} &= \left\{5\Omega^{(1,2)\star} - 4\Omega^{(1,3)\star}\right\} / \Omega^{(1,1)\star} \\ C^{\star} &= \Omega^{(1,2)\star} / \Omega^{(1,1)\star} \end{aligned} \tag{36}$$

These orders of η, k, and $\mathcal{D}$ suffice to fit all the available data for the gases discussed in this article.

A.6 Supplementary data: sixteen collision integral values of 6 digits accuracy (0.00001%)

T^*	$\Omega^{(1,1)\star}$	$\Omega^{(1,2)\star}$	$\Omega^{(1,3)\star}$	$\Omega^{(1,4)\star}$	$\Omega^{(1,5)\star}$	$\Omega^{(1,6)\star}$	$\Omega^{(1,7)\star}$	$\Omega^{(2,2)\star}$
0.30	2.6500024	2.2568342	1.9665277	1.7422927	1.5692059	1.4367486	1.3357334	2.8436719
0.35	2.4690902	2.0803498	1.7992869	1.5906654	1.4362847	1.3224167	1.2377740	2.6793810
0.40	2.3147191	1.9334804	1.6655752	1.4739771	1.3372123	1.2389202	1.1669636	2.5333021
0.45	2.1817500	1.8106979	1.5576333	1.3828143	1.2614679	1.1758283	1.1136355	2.4027196
0.50	2.0663606	1.7072842	1.4695923	1.3103104	1.2021301	1.1266734	1.0720503	2.2852477
0.55	1.9654568	1.6195116	1.3970409	1.2516628	1.1545826	1.0873425	1.0386623	2.1797044
0.60	1.8769305	1.5445772	1.3364925	1.2034475	1.1157023	1.0551401	1.0111924	2.0848158
0.65	1.7987221	1.4800688	1.2854200	1.1632213	1.0833326	1.0282481	0.98812233	1.9994146
0.70	1.7292913	1.4242462	1.2419179	1.1292004	1.0559550	1.0054049	0.96840757	1.9226284
0.75	1.6675641	1.3754865	1.2044863	1.1000678	1.0324731	0.98571345	0.95130868	1.8533519
0.80	1.6121364	1.3326440	1.1719829	1.0748426	1.0120831	0.96852089	0.93628907	1.7906831
0.85	1.5624746	1.2948503	1.1435158	1.0527821	0.99418312	0.95334226	0.92295044	1.7340892
0.90	1.5174627	1.2612243	1.1184037	1.0333110	0.97831663	0.93981035	0.91099132	1.6826234
0.95	1.4768357	1.2311810	1.0960772	1.0159875	0.96413043	0.92764266	0.90017961	1.6358666
1.00	1.4397702	1.2041955	1.0761146	1.0004554	0.95134931	0.91661848	0.89033337	1.5931672
1.05	1.4060217	1.1798014	1.0581465	0.98643969	0.93975414	0.90656270	0.88130844	1.5541219
1.10	1.3750666	1.1577189	1.0418789	0.97371159	0.92916937	0.89733523	0.87298883	1.5184065
1.15	1.3466473	1.1376075	1.0270868	0.96208905	0.91945328	0.88882209	0.86528009	1.4855505
1.20	1.3204234	1.1192153	1.0135626	0.95142110	0.91048923	0.88092999	0.85810466	1.4552844
1.25	1.2962670	1.1023150	1.0011456	0.94158523	0.90218129	0.87358176	0.85139815	1.4273571
1.30	1.2738574	1.0867759	0.98969426	0.93247623	0.89444917	0.86671280	0.84510662	1.4015367
1.35	1.2530452	1.0724095	0.97910188	0.92400777	0.88722575	0.86026898	0.83918453	1.3775536

T^*	$\Omega^{(1,1)\star}$	$\Omega^{(1,2)\star}$	$\Omega^{(1,3)\star}$	$\Omega^{(1,4)\star}$	$\Omega^{(1,5)\star}$	$\Omega^{(1,6)\star}$	$\Omega^{(1,7)\star}$	$\Omega^{(2,2)\star}$
1.40	1.2336136	1.0590926	0.96926129	0.91610605	0.88045410	0.85420416	0.83359312	1.3552816
1.45	1.2155747	1.0467019	0.96009215	0.90870885	0.87408586	0.84847912	0.82829923	1.3345419
1.50	1.1986808	1.0351603	0.95152055	0.90176277	0.86807940	0.84306002	0.82327421	1.3152088
1.55	1.1828536	1.0243771	0.94348497	0.89522147	0.86239909	0.83791765	0.81849327	1.2971279
1.60	1.1679578	1.0142682	0.93593428	0.88904506	0.85701370	0.83302664	0.81393476	1.2801718
1.65	1.1539511	1.0047749	0.92881914	0.88319896	0.85189631	0.82836480	0.80957967	1.2642756
1.70	1.1408224	0.99583780	0.92209781	0.87765275	0.84702325	0.82391262	0.80541135	1.2493360
1.75	1.1284010	0.98740237	0.91573575	0.87238001	0.84237367	0.81965290	0.80141495	1.2352709
1.80	1.1166373	0.97943615	0.90970084	0.86735749	0.83792919	0.81557048	0.79757735	1.2220198
1.85	1.1055155	0.97189625	0.90396440	0.86256423	0.83367350	0.81165172	0.79388680	1.2095019
1.90	1.0949587	0.96474278	0.89850262	0.85798182	0.82959206	0.80788453	0.79033282	1.1976519
1.95	1.0849179	0.95794271	0.89329397	0.85359390	0.82567190	0.80425810	0.78690594	1.1864277
2.0	1.0753782	0.95147239	0.88831761	0.84938582	0.82190137	0.80076262	0.78359768	1.1757878
2.1	1.0576880	0.93941612	0.87899283	0.84145786	0.81476839	0.79413024	0.77730684	1.1560755
2.2	1.0415415	0.92839764	0.87040761	0.83410749	0.80812087	0.78792640	0.77140676	1.1382131
2.3	1.0267699	0.91828467	0.86246292	0.82726094	0.80189937	0.78210064	0.76585289	1.1219472
2.4	1.0131781	0.90894977	0.85507731	0.82085684	0.79605443	0.77661074	0.76060781	1.1070586
2.5	1.0006472	0.90029830	0.84818368	0.81484417	0.79054453	0.77142109	0.75563978	1.0933919
2.6	0.98906701	0.89224814	0.84172453	0.80917987	0.78533451	0.76650137	0.75092168	1.0807943
2.7	0.97829129	0.88472900	0.83565191	0.80382741	0.78039436	0.76182556	0.74643015	1.0691400
2.8	0.96824673	0.87768660	0.82992513	0.79875553	0.77569826	0.75737120	0.74214494	1.0583269
2.9	0.95886031	0.87106903	0.82450913	0.79393736	0.77122390	0.75311876	0.73804836	1.0482551
3.0	0.95005427	0.86483130	0.81937367	0.78934962	0.76695180	0.74905117	0.73412491	1.0388470
3.1	0.94177557	0.85893580	0.81449279	0.78497194	0.76286495	0.74515340	0.73036091	1.0300376

T^*	$\Omega^{(1,1)\star}$	$\Omega^{(1,2)\star}$	$\Omega^{(1,3)\star}$	$\Omega^{(1,4)\star}$	$\Omega^{(1,5)\star}$	$\Omega^{(1,6)\star}$	$\Omega^{(1,7)\star}$	$\Omega^{(2,2)\star}$
3.2	0.93400074	0.85335175	0.80984369	0.78078651	0.75894835	0.74141217	0.72674421	1.0217697
3.3	0.92666046	0.84805008	0.80540630	0.77677772	0.75518872	0.73781571	0.72326405	1.0139889
3.4	0.91970993	0.84300574	0.80116297	0.77293164	0.75157428	0.73435352	0.71991072	1.0066494
3.5	0.91311310	0.83819666	0.79709810	0.76923595	0.74809450	0.73101614	0.71667561	0.99971193
3.6	0.90685315	0.83360430	0.79319799	0.76567966	0.74473996	0.72779516	0.71355081	0.99314079
3.7	0.90089774	0.82921201	0.78945026	0.76225293	0.74150216	0.72468291	0.71052933	0.98690575
3.8	0.89521976	0.82500346	0.78584389	0.75894689	0.73837349	0.72167248	0.70760469	0.98097605
3.9	0.88980006	0.82096453	0.78236895	0.75575354	0.73534696	0.71875763	0.70477109	0.97532751
4.0	0.88461425	0.81708302	0.77901658	0.75266566	0.73241634	0.71593260	0.70202323	0.96993895
4.1	0.87965381	0.81334769	0.77577864	0.74967666	0.72957583	0.71319223	0.69935616	0.96479082
4.2	0.87490764	0.80974903	0.77264787	0.74678059	0.72682026	0.71053164	0.69676551	0.95986544
4.3	0.87035232	0.80627792	0.76961763	0.74397198	0.72414477	0.70794656	0.69424703	0.95514646
4.4	0.86597230	0.80292597	0.76668185	0.74124583	0.72154501	0.70543286	0.69179709	0.95061857
4.5	0.86175561	0.79968564	0.76383499	0.73859757	0.71901691	0.70298691	0.68941206	0.94626864
4.6	0.85769318	0.79655010	0.76107195	0.73602297	0.71655672	0.70060518	0.68708870	0.94208483
4.7	0.85377421	0.79351319	0.75838809	0.73351815	0.71416099	0.69828452	0.68482413	0.93805622
4.8	0.84999456	0.79056912	0.75577912	0.73107956	0.71182653	0.69602196	0.68261547	0.93417280
4.9	0.84634383	0.78771273	0.75324108	0.72870382	0.70955036	0.69381476	0.68046011	0.93042544
5	0.84281354	0.78493952	0.75077033	0.72638792	0.70732973	0.69166044	0.67835565	0.92680619
6	0.81285427	0.76092265	0.72912577	0.70597537	0.68768908	0.67256505	0.65967671	0.89620912
7	0.78978812	0.74182420	0.71162085	0.68932388	0.67159018	0.65686760	0.64429297	0.87275246
8	0.77115143	0.72600688	0.69695069	0.67528837	0.65797787	0.64357010	0.63124604	0.85381806
9	0.75558286	0.71252733	0.68434230	0.66317681	0.64620640	0.63205656	0.61994085	0.83797577
10	0.74223469	0.70079676	0.67330028	0.65253913	0.63585166	0.62192004	0.60998263	0.82436995

T^*	$\Omega^{(1,1)\star}$	$\Omega^{(1,2)\star}$	$\Omega^{(1,3)\star}$	$\Omega^{(1,4)\star}$	$\Omega^{(1,5)\star}$	$\Omega^{(1,6)\star}$	$\Omega^{(1,7)\star}$	$\Omega^{(2,2)\star}$
20	0.66405281	0.62944509	0.60519146	0.58652602	0.57140344	0.55873123	0.54785312	0.74363086
30	0.62347510	0.59125466	0.56837928	0.55071357	0.53638643	0.52437838	0.51407164	0.70078919
40	0.59627779	0.56544434	0.54345126	0.52645211	0.51266524	0.50111255	0.49119952	0.67169995
50	0.57596616	0.54610667	0.52476590	0.50826839	0.49489105	0.48368462	0.47407140	0.64979124
60	0.55984084	0.53073284	0.50991043	0.49381509	0.48076715	0.46983950	0.46046786	0.63229371
70	0.54652207	0.51802665	0.49763441	0.48187445	0.46910151	0.45840686	0.44923670	0.61777649
80	0.53521100	0.50723298	0.48720820	0.47173560	0.45919842	0.44870342	0.43970638	0.60540410
90	0.52540444	0.49787433	0.47817019	0.46294861	0.45061739	0.44029690	0.43145039	0.59464667
100	0.51676535	0.48963015	0.47021007	0.45521112	0.44306276	0.43289720	0.42418449	0.58514739
200	0.46296112	0.43832021	0.42071111	0.40713202	0.39614770	0.38696530	0.37910221	0.52556475
300	0.43383794	0.41058661	0.39398951	0.38120211	0.37086503	0.36222809	0.35483526	0.49305524
400	0.41418524	0.39188997	0.37598843	0.36374360	0.35384941	0.34558517	0.33851320	0.47103246

T^*	$\Omega^{(2,3)\star}$	$\Omega^{(2,4)\star}$	$\Omega^{(2,5)\star}$	$\Omega^{(2,6)\star}$	$\Omega^{(3,3)\star}$	$\Omega^{(3,4)\star}$	$\Omega^{(3,5)\star}$	$\Omega^{(4,4)\star}$
0.30	2.5806610	2.3622719	2.1704207	2.0010465	2.3996913	2.1698726	1.9860912	2.5710549
0.35	2.4091063	2.1834561	1.9898392	1.8258038	2.2254600	2.0038490	1.8289555	2.3938882
0.40	2.2575571	2.0297914	1.8408867	1.6868985	2.0803510	1.8673483	1.7018522	2.2395320
0.45	2.1240588	1.8990875	1.7186542	1.5765238	1.9575384	1.7537232	1.5977523	2.1053244
0.50	2.0069722	1.7882134	1.6181863	1.4880206	1.8525505	1.6580928	1.5116212	1.9886589
0.55	1.9046180	1.6940822	1.5350981	1.4162050	1.7620821	1.5769424	1.4396656	1.8871923
0.60	1.8150156	1.6138942	1.4658166	1.3571792	1.6835043	1.5075387	1.3789923	1.7987636
0.65	1.7364493	1.5452565	1.4075304	1.3080480	1.6148438	1.4477580	1.3273775	1.7214751
0.70	1.6674359	1.4861632	1.3580404	1.2666544	1.5545007	1.3959162	1.2830921	1.6536775
0.75	1.6065811	1.4349531	1.3156437	1.2313822	1.5011905	1.3506548	1.2447869	1.5939665

T^*	$\Omega^{(2,3)\star}$	$\Omega^{(2,4)\star}$	$\Omega^{(2,5)\star}$	$\Omega^{(2,6)\star}$	$\Omega^{(3,3)\star}$	$\Omega^{(3,4)\star}$	$\Omega^{(3,5)\star}$	$\Omega^{(4,4)\star}$
0.80	1.5526726	1.3903133	1.2790066	1.2010100	1.4538369	1.3108971	1.2113994	1.5411581
0.85	1.5047917	1.3511504	1.2470898	1.1746032	1.4115863	1.2757691	1.1820864	1.4942592
0.90	1.4620443	1.3165932	1.2190696	1.1514400	1.3737257	1.2445561	1.1561756	1.4524316
0.95	1.4237576	1.2859202	1.1942947	1.1309565	1.3396477	1.2166734	1.1331257	1.4149738
1.00	1.3893188	1.2585459	1.1722436	1.1127074	1.3088446	1.1916425	1.1124988	1.3812893
1.05	1.3582156	1.2339935	1.1524937	1.0963379	1.2809145	1.1690665	1.0939370	1.3508871
1.10	1.3300294	1.2118563	1.1347033	1.0815622	1.2554800	1.1486110	1.0771464	1.3233387
1.15	1.3043943	1.1918081	1.1185922	1.0681483	1.2322414	1.1300009	1.0618842	1.2982860
1.20	1.2809860	1.1735721	1.1039286	1.0559062	1.2109437	1.1130009	1.0479478	1.2754262
1.25	1.2595512	1.1569163	1.0905207	1.0446789	1.1913652	1.0974136	1.0351684	1.2544978
1.30	1.2398589	1.1416427	1.0782082	1.0343361	1.1733062	1.0830712	1.0234031	1.2352759
1.35	1.2217188	1.1275872	1.0668561	1.0247685	1.1566067	1.0698304	1.0125311	1.2175683
1.40	1.2049473	1.1146073	1.0563501	1.0158838	1.1411207	1.0575671	1.0024495	1.2012088
1.45	1.1894056	1.1025824	1.0465931	1.0076041	1.1267275	1.0461757	0.99307048	1.1860539
1.50	1.1749662	1.0914076	1.0375022	0.99986251	1.1133123	1.0355640	0.98431832	1.1719775
1.55	1.1615160	1.0809925	1.0290059	0.99260197	1.1007802	1.0256524	0.97612759	1.1588698
1.60	1.1489623	1.0712592	1.0210426	0.98577312	1.0890508	1.0163714	0.96844160	1.1466352
1.65	1.1372108	1.0621399	1.0135589	0.97933319	1.0780449	1.0076599	0.96121097	1.1351894
1.70	1.1261887	1.0535748	1.0065081	0.97324497	1.0676999	0.99946422	0.95439245	1.1244586
1.75	1.1158312	1.0455117	0.99984960	0.96747593	1.0579583	0.99173737	0.94794812	1.1143770
1.80	1.1060784	1.0379050	0.99354748	0.96199748	1.0487650	0.98443768	0.94184454	1.1048868
1.85	1.0968772	1.0307135	0.98757016	0.95678443	1.0400747	0.97752803	0.93605214	1.0959359
1.90	1.0881810	1.0239013	0.98189003	0.95181448	1.0318466	0.97097562	0.93054467	1.0874785
1.95	1.0799496	1.0174365	0.97648202	0.94706785	1.0240442	0.96475115	0.92529879	1.0794735

T^*	$\Omega^{(2,3)\star}$	$\Omega^{(2,4)\star}$	$\Omega^{(2,5)\star}$	$\Omega^{(2,6)\star}$	$\Omega^{(3,3)\star}$	$\Omega^{(3,4)\star}$	$\Omega^{(3,5)\star}$	$\Omega^{(4,4)\star}$
2.0	1.0721422	1.0112907	0.97132416	0.94252689	1.0166328	0.95882826	0.92029365	1.0718843
2.1	1.0576712	0.99985674	0.96168219	0.93400056	1.0028680	0.94779539	0.91093290	1.0578241
2.2	1.0445409	0.98942473	0.95282960	0.92612771	0.99034584	0.93771554	0.90233462	1.0450714
2.3	1.0325613	0.97985338	0.94465732	0.91882073	0.97889431	0.92845696	0.89439477	1.0334411
2.4	1.0215773	0.97102666	0.93707600	0.91200766	0.96837334	0.91991113	0.88702785	1.0227808
2.5	1.0114602	0.96284896	0.93001171	0.90562882	0.95866550	0.91198800	0.88016290	1.0129643
2.6	1.0021004	0.95524048	0.92340281	0.89963429	0.94967207	0.90461216	0.87374059	1.0038861
2.7	0.99340868	0.94813418	0.91719743	0.89398190	0.94130938	0.89772016	0.86771093	0.99545741
2.8	0.98530826	0.94147344	0.91135165	0.88863584	0.93350643	0.89125817	0.86203147	0.98760320
2.9	0.97773329	0.93520999	0.90582799	0.88356547	0.92620218	0.88518026	0.85666594	0.98025947
3.0	0.97062776	0.92930264	0.90059428	0.87874436	0.91934463	0.87944694	0.85158315	0.97337142
3.1	0.96394335	0.92371569	0.89562274	0.87414960	0.91288876	0.87402418	0.84675611	0.96689191
3.2	0.95763837	0.91841838	0.89088924	0.86976125	0.90679542	0.86888240	0.84216139	0.96078014
3.3	0.95167605	0.91338390	0.88637269	0.86556181	0.90103025	0.86399579	0.83777848	0.95500065
3.4	0.94602470	0.90858880	0.88205461	0.86153587	0.89556349	0.85934176	0.83358936	0.94952249
3.5	0.94065658	0.90401245	0.87791870	0.85766981	0.89036869	0.85490049	0.82957817	0.94431847
3.6	0.93554710	0.89963667	0.87395053	0.85395152	0.88542254	0.85065434	0.82573082	0.93936475
3.7	0.93067461	0.89544535	0.87013727	0.85037020	0.88070445	0.84658775	0.82203481	0.93464011
3.8	0.92601967	0.89142414	0.86646749	0.84691616	0.87619607	0.84268685	0.81847895	0.93012585
3.9	0.92156512	0.88756027	0.86293092	0.84358073	0.87188098	0.83893924	0.81505322	0.92580526
4.0	0.91729564	0.88384227	0.85951835	0.84035606	0.86774479	0.83533380	0.81174863	0.92166346
4.1	0.91319746	0.88025985	0.85622148	0.83723505	0.86377411	0.83186053	0.80855706	0.91768708
4.2	0.90925819	0.87680372	0.85303280	0.83421126	0.85995719	0.82851038	0.80547115	0.91386415
4.3	0.90546674	0.87346549	0.84994548	0.83127885	0.85628337	0.82527521	0.80248424	0.91018384

T^*	$\Omega^{(2,3)\star}$	$\Omega^{(2,4)\star}$	$\Omega^{(2,5)\star}$	$\Omega^{(2,6)\star}$	$\Omega^{(3,3)\star}$	$\Omega^{(3,4)\star}$	$\Omega^{(3,5)\star}$	$\Omega^{(4,4)\star}$
4.4	0.90181294	0.87023757	0.84695332	0.82843246	0.85274294	0.82214777	0.79959026	0.90663639
4.5	0.89828765	0.86711304	0.84405067	0.82566720	0.84932712	0.81912111	0.79678368	0.90321296
4.6	0.89488258	0.86408560	0.84123237	0.82297859	0.84602795	0.81618917	0.79405943	0.89990551
4.7	0.89159019	0.86114950	0.83849366	0.82036249	0.84283808	0.81334635	0.79141289	0.89670672
4.8	0.88840358	0.85829945	0.83583020	0.81781512	0.83975103	0.81058750	0.78883978	0.89360992
4.9	0.88531644	0.85553064	0.83323798	0.81533297	0.83676050	0.80790791	0.78633618	0.89060900
5	0.88232298	0.85283861	0.83071330	0.81291278	0.83386098	0.80530310	0.78389847	0.88769837
6	0.85654973	0.82937384	0.80853723	0.79154957	0.80891308	0.78262759	0.76251500	0.86260235
7	0.83619863	0.81050537	0.79050905	0.77406342	0.78924407	0.76443263	0.74516965	0.84273175
8	0.81939793	0.79472897	0.77532473	0.75927045	0.77303257	0.74924772	0.73058710	0.82628544
9	0.80509669	0.78117621	0.76221439	0.74645986	0.75925378	0.73622396	0.71801542	0.81225329
10	0.79264954	0.76930082	0.75068505	0.73517070	0.74727784	0.72482750	0.70697412	0.80001509
20	0.71644579	0.69554433	0.67855911	0.66427378	0.67429261	0.65434851	0.63817231	0.72458743
30	0.67507284	0.65513376	0.63888735	0.62521359	0.63488403	0.61592387	0.60049842	0.68331752
40	0.64684273	0.62752545	0.61178127	0.59853428	0.60806710	0.58973506	0.57481379	0.65505591
50	0.62555277	0.60670537	0.59134838	0.57843324	0.58787704	0.57001539	0.55547876	0.63369637
60	0.60854523	0.59007918	0.57503914	0.56239643	0.57176719	0.55428446	0.54006052	0.61660850
70	0.59443663	0.57629285	0.56152168	0.54911025	0.55841509	0.54125073	0.52729066	0.60241831
80	0.58241611	0.56455190	0.55001433	0.53780381	0.54704700	0.53015758	0.51642587	0.59031847
90	0.57196833	0.55435118	0.54002015	0.52798715	0.53717186	0.52052451	0.50699402	0.57979498
100	0.56274587	0.54535011	0.53120413	0.51933007	0.52845897	0.51202788	0.49867723	0.57050077
200	0.50498732	0.48905190	0.47612279	0.46529004	0.47396894	0.45895175	0.44677450	0.51220356
300	0.47354227	0.45845471	0.44622782	0.43599273	0.44435102	0.43014706	0.41864148	0.48041234
400	0.45226789	0.43777361	0.42603617	0.41621633	0.42432860	0.41069132	0.39965208	0.45888704

A.7 References

[1] G. Colonna and A. Laricchiuta, Computer Physics Communications 178, 809 (2008).
[2] R. Eslamloueyan and M. Khademi, Chemometrics and Intelligent Laboratory Systems 104, 195 (2010).
[3] L. Boltzmann, American Journal of Physics 33, 974 (1965).
[4] R. B. Bird, W. E. Stewart, and E. N. Lightfoot, Transport Phenomena, 2nd ed. (Wiley, 2001).
[5] P. T. Gressman and R. M. Strain, PNAS 107, 5744 (2010).
[6] D. Enskog, Kinetische Theorie der Vorg¨ange in m¨assig verd¨unnten Gasen, Ph.D. thesis, Uppsala, Sweden (1917).
[7] S. Chapman, Philosophical Transactions of the Royal Society of London A 217, 115 (1918).
[8] S. Chapman and T. G. Cowling, The Mathematical Theory of Non-uniform Gases (Cambridge University Press, 1939).
[9] J. Hirschfelder, C. Curtiss, and R. B. Bird, Molecular Theory of Gases and Liquids (J. Wiley & Sons, New York, 1963).
[10] S. Harris, An Introduction to the Theory of the Boltzmann Equation (Holt, Rinehart, and Winston, 1971).
[11] U. R. Hattikudur and G. Thodos, The Journal of Chemical Physics 52, 4313 (1970).
[12] J. E. Lennard-Jones, Proceedings of the Royal Society of London A 109, 584 (1925).
[13] J. E. Lennard-Jones and B. M. Dent, Proceedings of the Royal Society of London. Series A 112, 230 (1926).
[14] E. V. Akhmatskaya and L. A. Pozhar, USSR Computational Mathematics and Mathematical Physics 26, 185 (1986).
[15] W. G. C. Boyd, Proceedings: Mathematical and Physical Sciences 447, 609 (1994).
[16] P. D. Neufeld, A. R. Janzen, and R. A. Aziz, The Journal of Chemical Physics 57, 1100 (1972).
[17] H. O'Hara and F. J. Smith, Computer Physics Communications 2, 47 (1971). 26
[18] E. A. Mason, The Journal of Chemical Physics 27, 782 (1957).
[19] S. J. Leon, Linear Algebra With Applications, 4th ed. (Macmillan Coll Div, 1994).
[20] K. W. Ford and J. A. Wheeler, Annals of Physics 7, 259 (1959).
[21] F. J. Smith and R. J. Munn, The Journal of Chemical Physics 41, 3560 (1964).
[22] S. Imam-Rahajoe, C. F. Curtiss, and R. B. Bernstein, The Journal of Chemical Physics 42, 530 (1965).
[23] H. Grad, Communications on Pure and Applied Mathematics 2, 331 (1949).
[24] J. O. Hirschfelder, R. B. Bird, and E. L. Spotz, The Journal of Chemical Physics 16, 968 (1948).
[25] J. O. Hirschfelder, R. B. Bird, and E. L. Spotz, The Journal of Chemical Physics 17, 1343 (1949).
[26] J. O. Hirschfelder, R. B. Bird, and E. L. Spotz, Chemical Reviews 44, 205 (1949).
[27] V. J. Berry Jr and R. C. Koeller, AIChE Journal 6, 274 (1960).
[28] M. Kotani, Proceedings of the Physico-Mathematical Society of Japan. 3rd Series 24, 76 (1942).
[29] T. Kihara and M. Kotani, Proceedings of the Physico-Mathematical Society of Japan. 3rd Series 25, 602 (1943).

[30] J. S. Rowlinson, The Journal of Chemical Physics 17, 101 (1949).
[31] F. London, Zeitschrift f¨ur Physik A Hadrons and Nuclei 63, 245 (1930).
[32] R. Eisenschitz and F. London, Zeitschrift f¨ur Physik A Hadrons and Nuclei 60, 491 (1930).
[33] H. Hettema, Quantum Chemistry: Classic Scientific Papers (World Scientific, Singapore, 2000).
[34] G. Hostetter, IEEE Transactions on Circuits and Systems 22, 697 (1975).
[35] G. Hostetter, IEEE Transactions on Automatic Control 20, 296 (1975).
[36] W. H. Press, Numerical Recipes in FORTRAN (Cambridge University Press, 1992).
[37] W. G. Horner, Philosophical Transactions of the Royal Society of London 109, 308 (1819).
[38] V. I. Krylov, Approximate Calculation of Integrals (Macmillan, 1962).
[39] F. Sharipov and G. Bertoldo, Journal of Computational Physics 228, 3345 (2009).
[40] U. Storck, ZAMM 78, 555 (1998).
[41] G. A. L. Delvigne and J. Los, Physica 63, 339 (1973).
[42] J. Lennard-Jones, Physica 4, 941 (1937).
[43] J. Kestin, K. Knierim, E. A. Mason, B. Najafi, S. T. Ro, and M. Waldman, Journal of Physical and Chemical Reference Data 13, 229 (1984).
[44] E. A. Mason and W. E. Rice, The Journal of Chemical Physics 22, 522 (1954).
[45] E. A. Mason, The Journal of Chemical Physics 22, 169 (1954).
[46] J. McCabe and S. Ouvry, Physics Letters B 260, 113 (1991). 27
[47] H. L. Frisch and E. Helfand, The Journal of Chemical Physics 32, 269 (1960).
[48] J. E. Jones, Proceedings of the Royal Society of London A 106, 441 (1924).
[49] J. E. Jones, Proceedings of the Royal Society of London A 106, 463 (1924).
[50] L. A. Viehland, A. R. Janzen, and R. A. Aziz, The Journal of Chemical Physics 102, 5444 (1995).
[51] J. J. Hurly and M. R. Moldover, Journal of Research of the National Institute of Standards and Technology 105, 667 (2000).
[52] G. C. Maitland and E. B. Smith, Journal of Chemical & Engineering Data 17, 150 (1972).
[53] P. C. Jain and S. C. Saxena, The Journal of Chemical Physics 63, 5052 (1975).
[54] V. Saxena and S. Saxena, Chemical Physics Letters 2, 44 (1968).
[55] V. K. Saxena and S. C. Saxena, The Journal of Chemical Physics 48, 5662 (1968).
[56] V. K. Saxena and S. C. Saxena, The Journal of Chemical Physics 51, 3361 (1969).
[57] S. Weissman, Physics of Fluids 16, 1425 (1973).
[58] S. Weissman and G. A. DuBro, Physics of Fluids 13, 2689 (1970).
[59] W. Groth and E. Sussner, Zeitschrift f¨ur Physikalische Chemie-Leipzig 193, 296 (1944).
[60] K. Schafer and K. Schuhmann, Zeitschrift f¨ur Elektrochemie 61, 246 (1957).
[61] B. K. Annis, A. E. Humphreys, and E. A. Mason, Physics of Fluids 12, 78 (1969).
[62] E. Winn, Physical Review 80, 1024 (1950).
[63] F. Hutchinson, The Journal of Chemical Physics 17, 1081 (1949).
[64] J. H. Dymond and E. B. Smith, The Virial Coefficients of Pure Gases and Mixtures (Clarendon Press, 1980).
[65] R. DiPippo and J. Kestin, Proceedings of the Fourth Symposium on Thermophysical Properties, College Park, MD , 304 (1968).